Fronteiras Fractais em Sistemas Hamiltonianos e em Relatividade Geral

Aluno: Alessandro Paulo Sérvio de Moura

Banca Examinadora:

Prof. Dr. Patricio Anibal Letelier Sotomayor (orientador) - IMECC/UNICAMP
Prof. Dr. George Emanuel Avraam Matsas - IFT-SP
Prof. Dr. Henrique Pereira de Oliveira - IF/UERJ
Profa. Dra. Kyoko Furuya - IFGW/UNICAMP
Prof. Dr. Marcus Aloizio Martinez de Aguiar - IFGW/UNICAMP
Prof. Dr. César Rogério de Oliveira (suplente) - DM/UFSC
Prof. Dr. Amir Ordaggi Caldeira (suplente) - IFGW/UNICAMP

Universidade Estadual de Campinas

15 de Março de 2000

Resumo

Estudamos a dinâmica de partículas-teste em sistemas hamiltonianos com escapes, incluindo sistemas de física newtoniana (o sistema de Hénon-Heiles para energias acima da energia de escape) e sistemas de relatividade geral correspondendo a distribuições de matéria axisimétricas e estáticas, que podem servir como modelo de centros galácticos; em particular, estudamos o movimento de partículas-teste em campos gravitacionais gerados por halos de matéria, com e sem um buraco negro central, tanto na formulação newtoniana como relativística. Também estudamos um sistema idealizado de dois buracos negros estáticos, onde o movimento de partículas-teste pode ser reduzido a um mapa, e uma dinâmica simbólica é encontrada explicitamente. Estudamos a dinâmica em geral caótica destes sistemas. A sensibilidade às condições iniciais é manifestada na estrutura fractal das bacias de escape. A dimensão fractal da fronteira entre as bacias de escape fornece uma medida quantitativa do caos nestes sistemas abertos.

Abstract

We study the dynamics of test particles in Hamiltonian systems with escapes, including Newtonian systems (the Hénon-Heiles system for energies above the escape energy) and general-relativistic systems corresponding to static axisymmetric mass distributions, which could be used to model galactic cores; in particular, we study the motion of test particles in gravitational fields generated by halos, with and without a central black hole, in both the Newtonian and the relativistic formulations. We also study an idealized two-black-hole system, wherein the motion of test particles is reduced to a map, and a symbolic dynamics is explicitly found. We find these systems have in general chaotic dynamics, and the sensibility to the initial conditions manifests itself in the fractal structure of the basins of escape. The fractal dimension of the boundary between the basins gives us a quantitative measure of chaos in these open systems.

Agradecimentos

Em primeiro lugar, quero agradecer ao meu orientador, o prof. Patricio Letelier, por ter me ensinado muito e me inspirado mais ainda. Agradeço também à FAPESP, por ter tornado este projeto possível, ao Instituto de Física Gleb Wataghin, ao Instituto de Matemática, Estatística e Ciência da Computação e à UNICAMP. Aos meus amigos Eduardo, Marcos, Daniel, Terracunha, Marcela, Montanha, e especialmente Claudio e Daniela, obrigado por terem me ajudado a manter contato com a realidade. Agradeço ademais ao Adilson, por nossas conversas estimulantes. Finalmente, agradeço à minha família.

Conteúdo

Introdução

A extrema sensibilidade às condições iniciais exibida por sistemas dinâmicos de baixa dimensionalidade regidos por leis de evolução determinísticas simples é uma das mais importantes descobertas da física-matemática. As complexas estruturas dinâmicas associadas a estes sistemas (ditos "caóticos") são objeto de estudos há várias décadas. Dentre os sistemas dinâmicos, destacam-se em importância os sistemas hamiltonianos, por sua extensa aplicação em física. Sistemas dinâmicos hamiltonianos são usados para descrever, entre outros fenômenos, o movimento de partículas-teste em campos conservativos, incluindo o campo métrico tensorial da relatividade geral. Nesta tese estudamos as manifestações de caos clássico (não-quântico) em sistemas hamiltonianos, em particular em sistemas da relatividade geral com interesse astrofísico. Focalizamos o nosso interesse em sistemas com *escapes*, onde o caos é de natureza transiente. Neste caso, a sensibilidade às condições iniciais manifesta-se através de uma dependência complexa da rota de escape escolhida pela partícula como função das condições iniciais. Observamos que o caos em sistemas relativísticos abertos ainda é um assunto pouco explorado.

A tese é dividida em duas partes: uma introdução geral, consistindo dos capítulos 1-4, e os resultados propriamente ditos, consistindo dos apêndices A, B, C e D, onde estão reproduzidos artigos publicados ou submetidos para publicação em revistas internacionais.

No capítulo 1 e 2, fazemos uma introdução aos conceitos de integrabilidade e caos em sistemas hamiltonianos genéricos; falamos entre outras coisas do problema dos pequenos denominadores em teoria de perturbação clássica, do teorema KAM, e da formação de emaranhados homoclínicos que dão origem ao caos. No capítulo 3, introduzimos as ferramentas para a análise de sistemas hamiltonianos abertos, que são diferentes daquelas usadas em sistemas confinados, mais comumente estudados. Nestes, o caos é caracterizado por seções de Poincaré, e é quantificado por coeficientes de

Lyapunov. No caso de sistemas abertos, o caos é caracterizado pela estrutura fractal da fronteira que separa as condições iniciais correspondendo a diferentes escapes, e é quantificado pela dimensão fractal desta fronteira. Em particular, mostramos que a dimensão fractal (ou dimensão box-counting) é uma medida direta da sensibilidade às condições iniciais que caracteriza o caos. No capítulo 4, resumimos brevemente os resultados da relatividade geral que usaremos, em particular a dinâmica de partículas-teste em campos estáticos axisimétricos, que serão extensamente explorados nos artigos reproduzidos nos Apêndices.

No Apêndice A, está reproduzido o artigo "Fractal basins in Hénon-Heiles and other polynomial potentials", onde estudamos o conhecido sistema de Hénon-Heiles para energias acima da energia de escape, quando o sistema apresenta três diferentes escapes. Mostramos numericamente que as bacias de escape (os conjuntos de condições iniciais correspondendo a cada escape distinto) têm uma estrutura fractal, e estudamos como esta estrutura fractal é formada pela dinâmica, e como esta estrutura e a sua correspondente dimensão fractal mudam com a energia. Estudamos também neste artigo outros potenciais polinomiais.

No Apêndice B, reproduzimos o artigo "Fractal escapes in Newtonian and relativistic multipole gravitational fields". Neste artigo estudamos o movimento planar (com momento angular nulo) de partículas em campos gravitacionais produzidos em uma região vazia de matéria por um halo material externo com simetria axial; admitimos também que o campo não depende do tempo. Na região interior ao halo, o campo gravitacional pode ser expandido em termos multipolares crescentes (ou seja, cuja intensidade aumenta longe da origem). Esta expansão multipolar também pode ser feita para campos relativísticos axisimétricos estáticos, como está explicado no capítulo 4. Estudamos a dinâmica para termos multipolares puros, que no caso newtoniano são dados por potenciais homogêneos nas coordenadas cartesianas, que apresentam escapes. Estudamos também a dinâmica dos campos relativísticos análogos, e comparamos os resultados.

No Apêndice C, reproduzimos o artigo "Chaos and Fractals in Geodesic Motions Around a Non-Rotating Black-Hole with Halos", onde estudamos um sistema similar àquele estudado no Apêndice B, mas incluindo um buraco negro central sem rotação, e ampliando a análise para partículas com momento angular. Um buraco negro cercado por um halo de matéria é um bom modelo para o centro de galáxias, o que torna este modelo mais realista; além disso, a introdução do buraco negro também é interessante do ponto de vista dinâmico, pois abre uma nova rota de escape para a partícula, correspondendo à queda no buraco negro, que não tem equivalente newtoniano.

Finalmente, no Apêndice D temos o artigo "Scattering map for two black holes", onde estudamos um modelo ultra-simplificado do movimento de raios de luz em um sistema composto de dois buracos negros de Schwarzschild. Fazendo as aproximações de que os dois buracos negros estão estáticos e a uma grande distância um do outro, reduzimos a dinâmica de uma partícula de luz orbitando o sistema a um mapa de duas dimensões, que pode ser analizado em detalhes. Demonstramos que existe uma dinâmica simbólica associada ao sistema, e que este é caótico, exibindo uma fronteira fractal entre os possíveis escapes (cair em um dos buracos negros ou escapar para o infinito). Demonstramos também outros alguns resultados analíticos, obtidos devido à simplicidade do sistema.

Capítulo 1

Sistemas Hamiltonianos e Integrabilidade

Neste primeiro capítulo, vamos estudar questões ligadas à integrabilidade e à estabilidade de sistemas da mecânica clássica, questões estas que deram origem ao estudo do caos. Começamos com uma rápida revisão da formulação hamiltoniana da mecânica, e em seguida passamos à equação de Hamilton-Jacobi, que nos fornece a maneira mais natural de formular o conceito de integrabilidade. Passamos então para a teoria clássica de perturbações e o problema dos pequenos denominadores, e finalmente enunciamos e discutimos o teorema KAM, sem demonstrá-lo.

As referências básicas para o assunto deste capítulo são [1, 2, 3, 4, 5, 6, 7].

1.1 Sistemas hamiltonianos

Na formulação hamiltoniana da mecânica clássica, a evolução temporal de um sistema com N graus de liberdade é dada pela função hamiltoniana $H = H(\mathbf{q}, \mathbf{p}, t)$, onde $\mathbf{q} = \{q_1, \cdots, q_N\}$ é o conjunto de coordenadas generalizadas, e $\mathbf{p} = \{p_1, \cdots, p_N\}$ é o conjunto de momenta generalizados. O espaço definido pelas coordenadas e pelos momenta é o chamado *espaço de fase*; cada ponto deste espaço define um estado do sistema. A evolução temporal do sistema é dada por uma trajetória $\mathbf{q} = \mathbf{q}(t)$, $\mathbf{p} = \mathbf{p}(t)$ no espaço de fase, determinada pelas equações de Hamilton:

$$\dot{q}_i = \frac{\partial H}{\partial p_i}; \qquad \dot{p}_i = -\frac{\partial H}{\partial q_i}, \tag{1.1}$$

onde $i = 1, \cdots, N$. Usando uma notação mais compacta:

$$\dot{\mathbf{q}} = \nabla_p H; \qquad \dot{\mathbf{p}} = -\nabla_q H. \tag{1.2}$$

Estas equações de movimento são obtidas através da extremização do funcional de ação S dado por:

$$S = \int (\dot{\mathbf{q}} \cdot \dot{\mathbf{p}} - H)\, dt, \tag{1.3}$$

onde $\dot{\mathbf{q}}$ é função de $\mathbf{q}$, $\mathbf{p}$ e t através da relação:

$$\mathbf{p} = \nabla_{\dot{q}} L, \tag{1.4}$$

onde L é a função Lagrangeana.

Podemos efetuar uma transformação de coordenadas no espaço de fase, e passar do conjunto de coordenadas e momenta $(\mathbf{q}, \mathbf{p})$ a um outro $(\mathbf{Q}, \mathbf{P})$, desde que preservemos a forma das equações de Hamilton (1.2). As transformações que satisfazem este critério são ditas *canônicas*. As transformações canônicas têm a propriedade de preservar o volume no espaço de fase, ou seja:

$$\int \cdots \int_U dq_1 \cdots dq_N dp_1 \cdots dp_N = \int \cdots \int_{D(U)} dQ_1 \cdots dQ_N dP_1 \cdots dP_N, \tag{1.5}$$

onde U é uma região qualquer do espaço de fase, e $D(U)$ denota esta mesma região nas novas coordenadas e momenta $\mathbf{Q}$, $\mathbf{P}$. Como as equações de Hamilton (1.2) definem uma transformação canônica, o volume de uma região do espaço de fase é preservado pela evolução temporal (teorema de Liouville).

As transformações canônicas podem ser construídas a partir de uma *função geratriz* $F = F(\mathbf{q}, \mathbf{P}, t)$, que é função das antigas coordenadas e dos novos momenta[1]. Em termos da função geratriz, as equações de transformação são:

$$\mathbf{Q} = \nabla_P F, \qquad \mathbf{p} = \nabla_q F. \tag{1.6}$$

A primeira equação acima nos dá $\mathbf{Q}$ como funçãode $\mathbf{q}$ e $\mathbf{P}$; invertendo, encontramos $\mathbf{q} = \mathbf{q}(\mathbf{Q}, \mathbf{P})$, e substituindo na segunda equação, encontramos $\mathbf{p} = \mathbf{p}(\mathbf{Q}, \mathbf{P})$.

A hamiltoniana H é transformada na nova hamiltoniana H' dada por:

$$H' = H\left(\mathbf{q}(\mathbf{Q}, \mathbf{P}), \mathbf{p}(\mathbf{Q}, \mathbf{P})\right) + \frac{\partial F}{\partial t}. \tag{1.7}$$

[1]Outros tipos de dependência são possíveis, mas não serão tratados aqui.

Vamos definir agora os *parênteses de Poisson* entre duas funções f e g:

$$\{f, g\} = \nabla_q f \cdot \nabla_p g - \nabla_p f \cdot \nabla_q g, \tag{1.8}$$

com $f = f(\mathbf{q}, \mathbf{p}, t)$ e $g = g(\mathbf{q}, \mathbf{p}, t)$.

O parêntesis de Poisson é invariante por transformações canônicas; através dele, as equações de movimento (1.2) podem ser escritas como:

$$\dot{\mathbf{q}} = \{\mathbf{q}, H\}; \qquad \dot{\mathbf{p}} = \{\mathbf{p}, H\}. \tag{1.9}$$

Na verdade, a evolução temporal de qualquer função das variáveis dinâmicas $f(\mathbf{q}, \mathbf{p}, t)$ tem esta forma:

$$\frac{df}{dt} = \{f, H\} + \frac{\partial f}{\partial t}. \tag{1.10}$$

Da definição (1.8), vemos que $\mathbf{q}$ e $\mathbf{p}$ satisfazem as chamadas *relações canônicas de comutação*:

$$\{q_i, q_j\} = \{p_i, p_j\} = 0; \qquad \{q_i, p_j\} = \delta_{ij}. \tag{1.11}$$

Estas relações são invariantes por transformações canônicas, e elas são condições necessárias e suficientes para que $\mathbf{q}$ e $\mathbf{p}$ formem um par canonicamente conjugado e obedeçam às equações de movimento (1.2).

Seja $f = f(\mathbf{q}, \mathbf{p})$ uma função das variáveis dinâmicas que não depende explicitamente do tempo. f é uma *constante de movimento* do sistema se $\frac{df}{dt} = 0$, ou seja, se ela se mantiver constante ao longo das trajetórias do sistema. Da eq. (1.10), vemos de imediato que isto implica:

$$\{f, H\} = 0. \tag{1.12}$$

Se f e g são duas constantes de movimento, pode-se mostrar que $\{f, g\}$ também é uma constante de movimento.

Geometricamente, a existência de uma constante de movimento representa uma restrição às trajetórias possíveis do sistema no espaço de fase, pois uma dada trajetória $(\mathbf{q}(t), \mathbf{p}(t))$ deve necessariamente estar contida na superfície $f(\mathbf{q}(t), \mathbf{p}(t)) = \text{cte}$, onde o valor da constante depende das condições iniciais. Se tivermos n constantes de movimento independentes, a trajetória do sistema fica restrita a uma variedade de $2N - n$ dimensões do espaço de fase. Se o sistema for conservativo (ou seja, se $\frac{\partial H}{\partial t} = 0$), é evidente da eq.(1.10) que a própria hamiltoniana é uma constante de movimento.

1.2 A equação de Hamilton-Jacobi e a Questão da Integrabilidade

Vamos a partir de agora restringir-nos a sistemas conservativos, onde a hamiltoniana é uma constante de movimento. Podemos encontrar as soluções para as equações de movimento se conseguirmos achar uma transformação canônica tal que a nova hamiltoniana H' seja função apenas dos novos momenta (que denotaremos α_i), e não dependa das novas coordenadas (que denotaremos β_i). Neste caso, pelas eqs.(1.2), os novos momenta serão constantes de movimento, e as novas coordenadas β_i terão uma evolução temporal trivial:

$$\dot{\alpha}_i = 0; \qquad \dot{\beta}_i = \frac{\partial H}{\partial \alpha_i} = \text{cte.} \tag{1.13}$$

Denotando por S a função geratriz para esta transformação, temos das equações (1.6) que:

$$\mathbf{p} = \nabla_q S; \qquad \boldsymbol{\beta} = \nabla_\alpha S, \tag{1.14}$$

com $S = S(\mathbf{q}, \boldsymbol{\alpha})$. Da equação (1.7), temos:

$$H(\mathbf{q}, \nabla_q S) = H'(\boldsymbol{\alpha}) \equiv E, \tag{1.15}$$

onde E é a energia; estamos admitindo que o sistema é conservativo. Esta é a *equação de Hamilton-Jacobi*, que é uma equação diferencial parcial não-linear de primeira ordem em S, com N variáveis independentes $q_1, \cdots, q_N$. A solução geral desta equação tem portanto N constantes arbitrárias, que podemos identificar com os novos momenta α_i. Podemos também identificar os α_i com quaisquer combinações algébricas independentes destas constantes.

Assim, se conseguirmos resolver a equação de Hamilton-Jacobi (1.15), teremos encontrado N constantes de movimento α_i, que podemos (em princípio) exprimir explicitamente em função de $\mathbf{q}$ e $\mathbf{p}$ através da inversão da primeira das equações (1.14):

$$\alpha_i = \alpha_i(\mathbf{q}, \mathbf{p}) = \text{cte.} \tag{1.16}$$

Assim, neste caso a trajetória do sistema está restrita a uma variedade N-dimensional no espaço de fase $2N$-dimensional. Quando isto acontese, ou seja, quando a equação de Hamilton-Jacobi é solúvel, o sistema é dito *integrável*.

Das relações (1.11), e do fato de estas serem invariantes por transformações canônicas, temos que:

$$\{\alpha_i, \alpha_j\} = 0, \qquad \text{p/ todo } i,\ j. \tag{1.17}$$

Assim, as N constantes de movimento definidas pelos novos momenta estão *em involução* (ou seja, satisfazem a relação acima). Usando este resultado e o fato de estas N constantes serem independentes (o que vem do dato de os N momenta de um sistema com N graus de liberdade serem independentes), podemos demonstrar que as variedades N-dimensionais onde estão confinadas as órbitas dos sistemas integráveis são N-toros. Para isso, vamos definir N campos vetoriais no espaço de fase:

$$\mathbf{V}_i = \left(\nabla_p \alpha_i, -\nabla_q \alpha_i\right), \qquad i = 1, 2, \cdots, N. \tag{1.18}$$

Os α_i são dados por (1.16).

Fixando os N valores dos α_i, estaremos fixando a variedade N-dimensional no espaço de fase onde as órbitas ficam restritas (para uma dada condição inicial). Denotaremos esta variedade por $\mathcal{M}$. O campo de vetores $\mathbf{n}_i$ perpendicular à superfície definida por $\alpha_i(\mathbf{q}, \mathbf{p}) = \alpha_i$, e portanto perpendicular também a $\mathcal{M}$, é dado por:

$$\mathbf{n}_i = \left(\nabla_q \alpha_i, \nabla_p \alpha_i\right). \tag{1.19}$$

Temos então que:

$$\mathbf{V}_i \cdot \mathbf{n}_j = \nabla_q \alpha_j \cdot \nabla_p \alpha_i - \nabla_p \alpha_j \cdot \nabla_q \alpha_i = \{\alpha_j, \alpha_i\} = 0, \tag{1.20}$$

para todo i, j.

Assim, os campos vetoriais $\mathbf{V}_i$ são tangenciais a $\mathcal{M}$. Para movimentos limitados (ou "ligados"), $\mathcal{M}$ é uma variedade compacta. Resumindo, $\mathcal{M}$ é uma variedade compacta com N dimensões e sobre a qual estão definidos N campos vetoriais tangenciais independentes $\mathbf{V}_i$ (pois os α_i são independentes). Disto pode-se mostrar que $\mathcal{M}$ é um N-toro [8].

Um N-toro é uma variedade multiplamente conexa com N caminhos fechados independentes e não-homeomorfos a um ponto. Escolhendo N tais caminhos C_i ($i = 1, \cdots, N$), definimos as chamadas *variáveis de ação* $\mathbf{I} = (I_1, \cdots, I_N)$:

$$I_i = \frac{1}{2\pi} \oint_{C_i} \mathbf{p} \cdot d\mathbf{q} = \frac{1}{2\pi} \oint_{C_i} \sum_{i=1}^{N} p_i dq_i. \tag{1.21}$$

Cada um dos I_i é por construção uma constante de movimento, e como os caminhos C_i são independentes, os I_i também são. Podemos então exprimi-los como funções dos α_i, e escolhê-los como sendo os novos momenta. As coordenadas conjugadas θ_i (*variáveis de ângulo*) são dadas por:

$$\theta_i = \frac{\partial S}{\partial I_i}, \tag{1.22}$$

onde $S = S(\mathbf{q}, \mathbf{I})$. As novas coordenadas assim definidas têm a propriedade de variar de 2π no circuito correspondente:

$$\oint_{C_i} d\theta_i = 2\pi; \qquad \oint_{C_i} d\theta_j = 0, \ \text{p/ } i \neq j. \tag{1.23}$$

As variáveis θ_i são as coordenadas naturais definidas em um N-toro. Os valores das variáveis de ação I_i identificam em qual toro nós estamos, enquanto que os θ_i dizem onde estamos neste toro.

As equações de movimento (1.13) para as variáveis de ângulo-ação se escrevem:

$$\begin{aligned} \dot{\mathbf{I}} = 0 \implies \mathbf{I} = \text{cte}; \\ \dot{\boldsymbol{\theta}} = \boldsymbol{\omega} \implies \boldsymbol{\theta}(t) = \boldsymbol{\theta}_0 + \boldsymbol{\omega} t, \end{aligned} \tag{1.24}$$

onde $\boldsymbol{\omega} = (\omega_1, \cdots, \omega_N)$ é dado por:

$$\boldsymbol{\omega} = \nabla_I H', \tag{1.25}$$

onde $H' = H'(\mathbf{I})$ é a energia escrita em termos das variáveis de ação, e os ω_i são as frequências do movimento no toro indexado por $\mathbf{I}$.

Os θ_i são coordenadas angulares, ou seja, $\theta_i + 2n\pi$ indica o mesmo ponto que θ_i, para n inteiro. Logo, qualquer função $f(\mathbf{q}, \mathbf{p})$ das variáveis dinâmicas pode ser escrita como uma série de Fourier nas coordenadas θ_i:

$$f(\mathbf{q}, \mathbf{p}) = \sum_{\mathbf{m}} f_{\mathbf{m}}(\mathbf{I}) e^{i\mathbf{m} \cdot \boldsymbol{\theta}}, \tag{1.26}$$

com $\mathbf{m} = (m_1, \cdots, m_N)$ sendo um vetor N-dimensional com coeficientes inteiros. Usando a equação (1.24), teremos:

$$f(\mathbf{q}(t), \mathbf{p}(t)) = \sum_{\mathbf{m}} f_{\mathbf{m}}(\mathbf{I}) e^{i(\mathbf{m} \cdot \boldsymbol{\omega} t + \mathbf{m} \cdot \boldsymbol{\theta}_0)}. \tag{1.27}$$

Em particular, temos:

$$q(t) = \sum_{\mathbf{m}} q_{\mathbf{m}}(\mathbf{I}) e^{i(\mathbf{m}\cdot\boldsymbol{\omega} t + \mathbf{m}\cdot\boldsymbol{\theta}_0)}. \tag{1.28}$$

Assim, a evolução temporal de qualquer função das variáveis dinâmicas é multiplamente periódica (ou quasiperiódica), com um número N de frequências independentes igual ao número de graus de liberdade, em um sistema integrável.

No caso geral, as N frequências ω_i são incomensuráveis, e a órbita preenche densamente o N-toro no qual ela está contida. Em casos particulares, os ω_i podem não ser incomensuráveis, ou seja, podemos ter relações do tipo:

$$\mathbf{m}\cdot\boldsymbol{\omega} = 0, \tag{1.29}$$

para um ou mais vetores $\mathbf{m}$ linearmente independentes com entradas inteiras. Caso tenhamos um número k de relações independentes deste tipo, a órbita preenche um sub-espaço $(N-k)$-dimensional dentro do toro, e este caso é dito *k-degenerado*. Se $k = N - 1$, a órbita é fechada e o movimento é periódico.

1.3 Teoria Clássica de Perturbações e o Teorema KAM

Vimos na seção anterior que sistemas integráveis (ou seja, aqueles em que a equação de Hamilton-Jacobi pode ser resolvida) têm órbitas restritas a uma variedade N-dimensional com a topologia de um N-toro, com N frequências características (movimento multiplamente periódico, ou quasiperiódico).

Surge então a questão da estabilidade dos sistemas integráveis, ou seja: dado um sistema integrável, se o perturbarmos fracamente suas trajetórias continuarão restritas a toros, mesmo que levemente distorcidos? Esta questão foi atacada no começo do século, em conexão com o problema da estabilidade do sistema solar. A tentativa de resolvê-la levou Poincaré à criação de um novo ramo da matemática: o estudo dos sistemas dinâmicos (ver [9]).

Vamos formular este problema um pouco mais rigorosamente: seja uma hamiltoniana integrável H_0, e seja H a hamiltoniana total do sistema, dada por:

$$H = H_0 + \epsilon H_1, \tag{1.30}$$

resultante da perturbação de H_0 pelo termo "pequeno" ϵH_1, sendo $\epsilon \ll 1$ um parâmetro adimensional que mede a intensidade da perturbação. A pergunta é se H é integrável ou não, para ϵ suficientemente pequeno.

Uma maneira de atacar este problema é usar a teoria de perturbações canônica. Para isto, escreveremos a hamiltoniana H em termos das variáveis de ângulo-ação $\mathbf{I}$, $\boldsymbol{\theta}$ da hamiltoniana integrável H_0:

$$H(\mathbf{I},\boldsymbol{\theta}) = H_0(\mathbf{I}) + \epsilon H_1(\mathbf{I},\boldsymbol{\theta}). \tag{1.31}$$

Por causa da perturbação ϵH_1, $\mathbf{I}$ não será em geral constante, e $\boldsymbol{\theta}$ não terá uma variação linear com o tempo, ou seja, $\mathbf{I}$ e $\boldsymbol{\theta}$ não são variáveis de ângulo-ação da hamiltoniana não-perturbada H, mas elas ainda são, é claro, variáveis canônicas. O objetivo da teoria de perturbações clássica é encontrar uma transformação para um novo conjunto de coordenadas canônicas ($\mathbf{J}$,$\boldsymbol{\phi}$) que sejam variáveis de ângulo-ação para a hamiltoniana perturbada H. Se conseguirmos fazer isso, teremos mostrado que H é integrável.

Denotemos S a função geratriz que realiza a transformação (se ela for possível). Como admitimos que ϵ é muito menor que 1, vamos tentar escrever S como uma série de potências em ϵ:

$$S = \boldsymbol{\theta}\cdot\mathbf{J} + \epsilon S_1 + \cdots, \tag{1.32}$$

onde o primeiro termo é simplesmente a transformação identidade. A equação de Hamilton-Jacobi fica:

$$H_0(\nabla_\theta S) + \epsilon H_1(\nabla_\theta S,\boldsymbol{\theta}) = H_0'(\mathbf{J}) + \epsilon H_1'(\mathbf{J}), \tag{1.33}$$

onde H' é a hamiltoniana escrita em termos das novas variáveis de ação $\mathbf{J}$. Expandindo em série de Taylor e mantendo termos de até primeira ordem em ϵ, teremos as equações:

$$\begin{aligned} &H_0(\mathbf{J}) = H_0'(\mathbf{J}) && \text{ordem zero} \\ &\nabla_\theta S_1\cdot\nabla_J H_0(\mathbf{J}) + H_1(\mathbf{J},\boldsymbol{\theta}) = H_1'(\mathbf{J}) && \text{ordem um} \end{aligned} \tag{1.34}$$

A primeira equação nos diz simplesmente que em ordem zero a energia do sistema perturbado é igual à do sistema não-perturbado. Tomando uma média em $\boldsymbol{\theta}$ na segunda equação, encontramos a correção de primeira ordem na energia:

$$H_1'(\mathbf{J}) = \overline{H_1}(\mathbf{J}), \tag{1.35}$$

onde

$$\overline{H_1}(\mathbf{J}) = \int_0^{2\pi} d\theta_1 \cdots \int_0^{2\pi} d\theta_N H_1(\mathbf{J}, \boldsymbol{\theta}) \tag{1.36}$$

é a média de H_1 no toro indexado por $\mathbf{J}$.

Como $\theta_1, \cdots, \theta_N$ são variáveis tipo ângulo, qualquer função de $\boldsymbol{\theta}$ pode ser escrita como uma série de Fourier em $\boldsymbol{\theta}$. Assim, escrevemos H_1 e S_1 na forma:

$$\begin{aligned} S_1(\mathbf{J}, \boldsymbol{\theta}) &= \sum_{\mathbf{m}} S_{1\mathbf{m}}(\mathbf{J}) e^{i\mathbf{m} \cdot \boldsymbol{\theta}}, \\ H_1(\mathbf{J}, \boldsymbol{\theta}) &= \sum_{\mathbf{m}} H_{1\mathbf{m}}(\mathbf{J}) e^{i\mathbf{m} \cdot \boldsymbol{\theta}}. \end{aligned} \tag{1.37}$$

Usando a eq. (1.35) e substituindo as duas expressões acima na eq. (1.34), encontramos:

$$S_1(\mathbf{J}, \boldsymbol{\theta}) = i \sum_{\mathbf{m}} \frac{H_{1\mathbf{m}} e^{i\mathbf{m} \cdot \boldsymbol{\theta}}}{\mathbf{m} \cdot \omega_0(\mathbf{J})}; \tag{1.38}$$

lembramos que $\omega_0(\mathbf{J}) = \nabla_J H_0(\mathbf{J})$.

Aqui encontramos o famoso "problema dos pequenos denominadores": se as frequências $\omega_{01}, \cdots, \omega_{0N}$ são comensuráveis, ou seja, se elas satisfazem a relação

$$\mathbf{m} \cdot \boldsymbol{\omega}_0 = 0 \tag{1.39}$$

para algum $\mathbf{m}$, o denominador do termo correspondente em (1.38) diverge; e mesmo que as frequências ω_0 não sejam comensuráveis, existem números inteiros $m_1, \cdots, m_N$ tais que a igualdade (1.39) é satisfeita com uma precisão arbitrária, pois todo número real pode ser aproximado tanto quanto se queira por números racionais. Assim, quaisquer que sejam os ω_{0i}, vão haver termos em (1.38) que tendem ao infinito, e como os números racionais formam um conjunto denso nos reais, a função $S_1(\boldsymbol{\theta}, \mathbf{J})$ é divergente e descontínua, o que viola as hipóteses que nós implicitamente assumimos sobre a continuidade e suficiente diferenciabilidade de S. Assim, a teoria clássica de perturbações falha em nos dar a resposta sobre a integrabilidade da hamiltoniana perturbada.

A solução deste problema foi encontrada por Kolmogorov, Arnold e Moser, e constitui o famoso teorema KAM, que nós vamos enunciar e discutir sem demonstrar.

Seja um sistema integrável com N graus de liberdade descrito pela hamiltoniana $H_0(\mathbf{I})$, com variáveis de ângulo-ação I_i, θ_i $(i = 1, \cdots, N)$, sendo $\omega_i = \partial H_0 / \partial I_i$ as frequências associadas ao N-toro correspondente a

$(I_1, \cdots, I_N)$. Supomos que H_0 é uma função analítica e que o sistema é não-degenerado, ou seja:

$$\det\left(\frac{\partial \omega_i}{\partial I_j}\right) = \det\left(\frac{\partial^2 H_0}{\partial I_i \partial I_j}\right) \neq 0. \tag{1.40}$$

Se o sistema for perturbado por um termo pequeno $\epsilon H'(\mathbf{I}, \boldsymbol{\theta})$, para ϵ suficientemente pequeno o teorema KAM nos diz que:

- Se as frequências ω_i forem "suficientemente incomensuráveis", existe um toro, que é próximo ao toro correspondente no sistema não-perturbado, onde as trajetórias do sistema perturbado (correspondentes a estas frequências) vão estar contidas.

- Se as frequências ω_i forem "suficientemente comensuráveis", então o toro é destruido, e as trajetórias correspondentes exploram uma região do espaço de fase de dimensão maior que N (em geral).

- A região do espaço de fase onde os toros são destruidos (regiões com frequências "suficientemente comensuráveis") tem medida de Lebesgue finita e que é tanto menor quanto menor for a perturbação $\epsilon H'$, tendendo a zero para $\epsilon H' \to 0$.

Os termos "suficientemente comensuráveis" e "suficientemente incomensuráveis" têm significados precisos em teoria de números; para exemplificar, em um sistema de 2 graus de liberdade, as duas frequências ω_1 e ω_2 são "suficientemente incomensuráveis" se, dado um número racional arbitrário r/s (r e s inteiros) que aproxima o número real ω_1/ω_2, vale a desigualdade:

$$\left|\frac{\omega_1}{\omega_2} - \frac{r}{s}\right| > \frac{K(\epsilon)}{s^{5/2}}, \tag{1.41}$$

para quaisquer inteiros r e s, onde $K(\epsilon)$ é uma função que vai a 0 para $\epsilon \to 0$. Os toros que não satisfazem (1.41) são em geral destruidos pela perturbação.

Capítulo 2

Caos

No final do capítulo anterior, vimos que para sistemas integráveis fracamente perturbados a maioria dos toros é preservada (ainda que levemente distorcidos), a não ser aqueles com frequências "suficientemente comensuráveis". Para estes, sabemos que as trajetórias correspondentes exploram regiões do espaço de fase com dimensionalidade maior que N, mas gostaríamos de ter mais informações sobre estas trajetórias. Além disso, o teorema KAM só vale para para perturbações fracas; o que acontece com sistemas onde a perturbação não pode ser considerada pequena ?

2.1 Seções de Poincaré e Mapas "Twist"

Vamos introduzir agora um conceito extremamente útil no estudo de sistemas dinâmicos: o mapa de Poincaré. Para isso, nos restringiremos daqui por diante a sistemas com 2 graus de liberdade, para facilitar a exposição.

Se o sistema é conservativo, ele tem pelo menos uma constante de movimento (a energia), e as trajetórias do sistema estão confinadas a uma variedade 3-dimensional (a chamada *energy shell*). A existência de uma outra constante de movimento significa então que o sistema é integrável. Consideremos uma superfície 2-dimensional dentro de uma destas "energy shells". Escolha uma condição inicial nesta superfície e siga a trajetória correspondente, marcando os pontos onde a trajetória intersecta a superfície. Teremos então um conjunto de pontos no plano. Se a trajetória for periódica, este conjunto é composto por um número finito de pontos. Se o sistema for integrável, as condições iniciais pertencentes a toros com frequências incomensuráveis (que é o caso geral) correspondem a um conjunto de pontos no plano se secção que, apesar de infinito, está contido em uma variedade 1-dimensional no plano, pois estes pontos estão na intersecção do plano com o 2-toro. No caso geral, um sistema apresenta tanto regiões integráveis (com órbitas contidas em N-toros) como não-integráveis (com órbitas não contidas em toros) no espaço de fase.

Com este procedimento, definimos um mapa do plano no plano: cada ponto do plano é levado a um outro ponto pela evolução temporal do sistema. Este mapa tem a propriedade de conservar a área (ver por exemplo [6]).

Suponha agora que estamos tratando de um sistema integrável. Temos então as variáveis de ângulo-ação $I_1, I_2, \theta_1, \theta_2$. Escolhendo a superfície de seção tal que esta corta o toro perpendicularmente à direção em que θ_2 aumenta, e considerando I_1 como uma variável radial (I_2 já está fixado por conservação de energia), definimos um mapa como mostrado na fig. 2.1. I_1 e I_2 são constantes pelas equações (1.24). Denotando $r \equiv I_1$, e $\alpha \equiv \omega_1/\omega_2 = \alpha(r)$, este mapa (chamado de "mapa twist") é dado por:

$$T = \begin{cases} \theta_{i+1} = \theta_i + 2\pi\alpha \\ r_{i+1} = r_i \end{cases} . \tag{2.1}$$

Assim, nestas coordenadas, temos um mapa dos círculos $r = \text{const}$ neles mesmos: todo o círculo é girado pelo ângulo $2\pi\alpha$ em cada iteração. Como α depende de r, uma linha reta radial é em geral mapeada em uma curva.

Se perturbarmos o sistema com um termo não-integrável, como em (1.30), I_1, I_2, θ_1 e θ_2 continuam a ser variáveis canonicamente conjugadas, mas elas não são mais variáveis de ângulo-ação, e suas equações de movimento não são mais tão simples como em (1.24). O novo mapa "twist" é então dado por:

$$T_\epsilon = \begin{cases} \theta_{i+1} = \theta_i + 2\pi\alpha + \epsilon f(r_i, \theta_i) \\ r_{i+1} = r_i + \epsilon g(r_i, \theta_i) \end{cases} , \tag{2.2}$$

onde f e g vêm da perturbação.

2.2 O Teorema de Poincaré-Birkhoff

Vamos estudar com mais detalhes o mapa "twist" definido na seção anterior, e para isto vamos revisar rapidamente algumas propriedades básicas de mapas em duas dimensões.

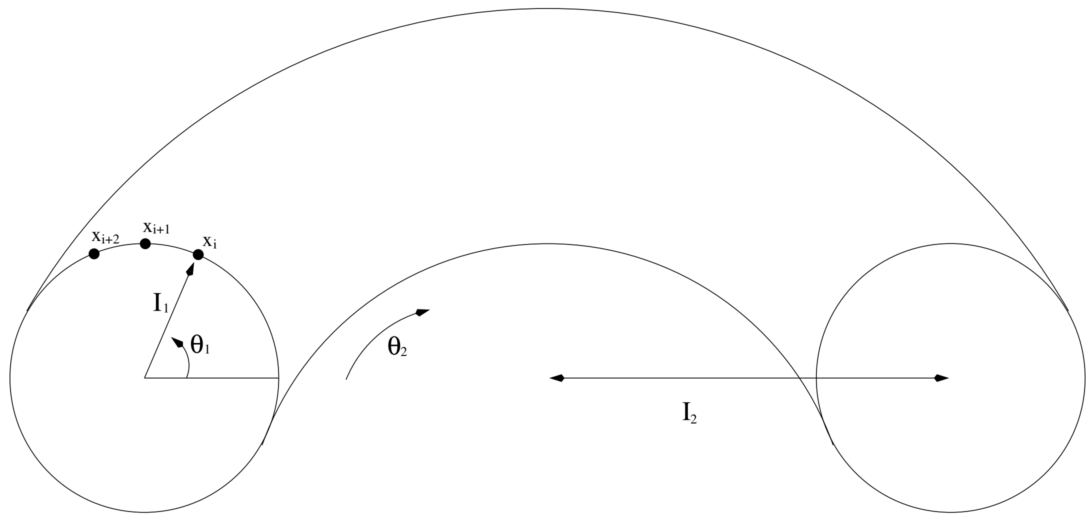

Figura 2.1: Ilustração do mapa "twist"

Seja um mapa T definido por:

$$\begin{pmatrix} x_1' \\ x_2' \end{pmatrix} = T \begin{pmatrix} x_1 \\ x_2 \end{pmatrix} = \begin{pmatrix} T_1(x_1, x_2) \\ T_2(x_1, x_2) \end{pmatrix}. \tag{2.3}$$

Os *pontos fixos* (x_{10}, x_{20}) de T são pontos que satisfazem $\begin{pmatrix} x_{10} \\ x_{20} \end{pmatrix} = T \begin{pmatrix} x_{10} \\ x_{20} \end{pmatrix}$. A partir de uma linearização em torno de um ponto fixo, podemos determinar a sua estabilidade, se o ponto fixo não for um centro (teorema de Hartman-Grobman, ver [15]. Sendo $(\partial T_i/\partial x_j)\,|_{(x_{10},x_{20})} \equiv J_{ij}$ a matriz jacobiana de T calculada no ponto fixo, a linearização de T em torno deste ponto é dada por:

$$T_{lin} = \begin{pmatrix} J_{11} & J_{12} \\ J_{21} & J_{22} \end{pmatrix}. \tag{2.4}$$

A equação característica de T_{lin} define dois autovalores λ_1 e λ_2. Para mapas que têm a propriedade de preservar a área (como o mapa "twist"), devemos ter $\lambda_1 \cdot \lambda_2 = 1$, e temos as seguintes possibilidades:

- $\lambda_1 = \lambda_2^* = e^{i\alpha}$, com α real (centro).

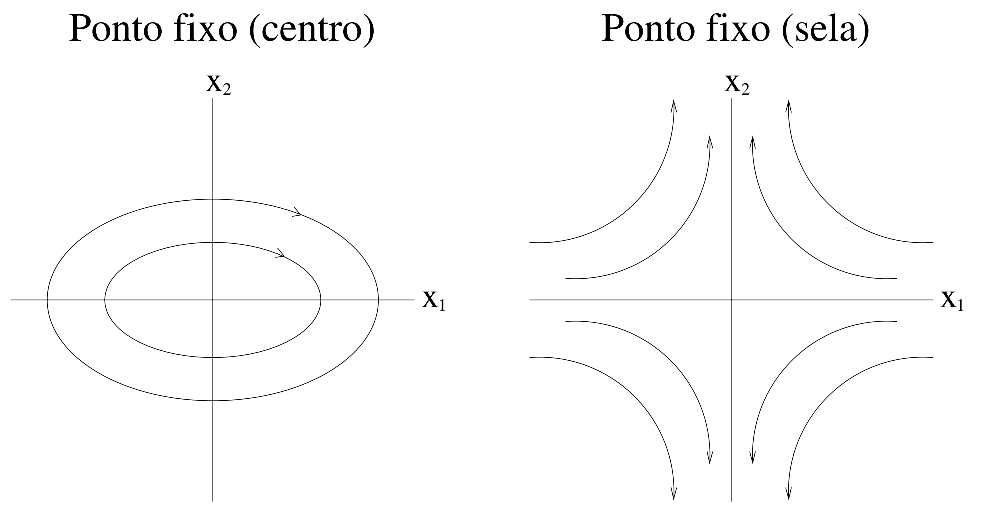

Figura 2.2: Tipos de pontos fixos do mapa T

- $\lambda_1 = 1/\lambda_2$, com λ_1 e λ_2 reais (ponto hiperbólico).

No primeiro caso, temos um ponto de equilíbrio estável, e no segundo caso, um ponto de equilíbrio instável, com duas trajetórias tendendo a (x_{10}, x_{20}) para $t \to \infty$ (variedade estável), e duas trajetórias tendendo a (x_{10}, x_{20}) para $t \to -\infty$ (variedade instável). Ver fig. 2.2.

Voltemos ao mapa "twist", considerando um sistema integrável com hamiltoniana H_0. Voltando à notação da seção anterior, considere um valor de r para o qual a razão $\alpha = \omega_1/\omega_2$ é racional: $\alpha = \frac{m}{n}$ (m, n inteiros), denotando por C o círculo correspondente nas coordenadas (r, θ). Escolhemos dois círculos C^+ e C^- próximos de C com valores irracionais de α (ver fig. 2.3a). α é uma função bem comportada de r; assumimos, para fixar as idéias, que α seja uma função crescente de r em C, o que significa que C^+ roda no sentido anti-horário em relação a C, e C^- roda no sentido horário em relação a C (fig. 2.3a). Assim, sob a aplicação do mapa T^n (com T definido por (2.1)), o círculo C permanece inalterado, enquanto que C^+ e C^- rodam como indicado na figura 2.3a.

Consideremos agora a perturbação não-integrável T_ϵ do mapa T, dada pela eq. (2.2), com $\epsilon \ll 1$. O teorema KAM nos garante que as curvas invariantes C^+ e C^- são preservadas, para ϵ suficientemente pequeno, mesmo que ligeiramente distorcidas; denotaremos por C_ϵ^+ e C_ϵ^- as novas curvas invariantes do mapa T_ϵ.

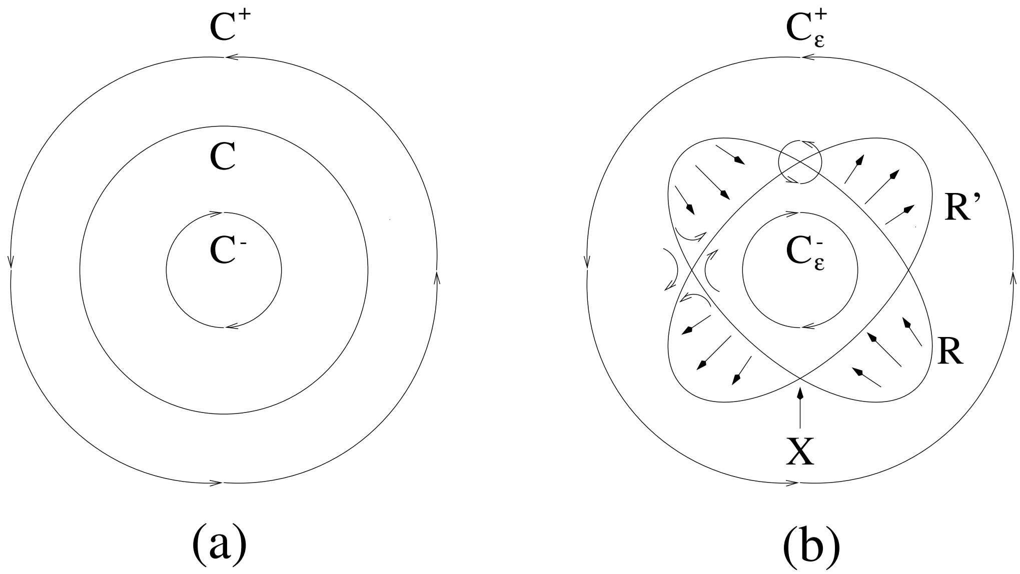

Figura 2.3: O teorema de Poincaré-Birkhoff

A curva C, no entanto, é destruida, por corresponder a frequências comensuráveis. Mesmo não existindo uma curva invariante correspondendo a C, existem pontos fixos isolados no mapa T_ϵ^n, como mostramos a seguir. Da fig. 2.3a, fica claro que existe uma curva R tal que a coordenada r é preservada pelo mapa T_ϵ^n. Definindo a curva R' por $R' = T_\epsilon^n R$, os pontos onde R e R' intersectam são pontos fixos de T_ϵ^n (fig. 2.3b). Da fig. 2.3b vemos de imediato que o número de intersecções é par. Se X é um destes pontos fixos, então $T_\epsilon X, T_\epsilon^2 X, \cdots, T_\epsilon^{n-1} X$ também são pontos fixos, ou seja, existe um número par $2kn$ de de pontos fixos de T_ϵ^n (k inteiro). Além disso, como mostra a figura 2.3b, estes pontos fixos são alternadamente centros e selas. Estes resultados constituem o *teorema de Poincaré-Birkhoff*.

Mas isso não é tudo. Em torno de cada um dos kn centros, temos localmente uma situação como a mostrada na fig. 2.3, com uma estrutura própria de curvas invariantes, cada uma delas tendo suas frequências correspondentes. Aplicamos então o teorema de Poincaré-Birkhoff novamente: para aquelas curvas com frequências comensuráveis, aparecem novamente pontos fixos tipo centro e tipo sela, alternadamente; e assim por diante, em todas as escalas; o resultado é a estrutura auto-similar esboçada na fig. 2.4.

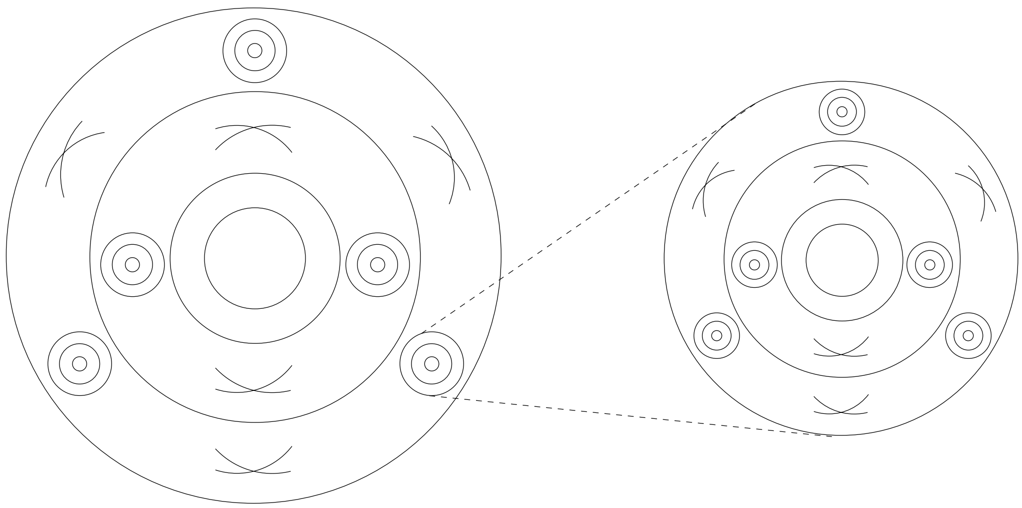

Figura 2.4: Aplicações sucessivas do teor. de Poincaré-Birkhoff

2.3 Pontos Homoclínicos e o Surgimento do Caos

Na seção anterior vimos o que acontece com os centros que resultam da destruição dos toros com frequências comensuráveis. Agora vamos estudar os pontos de sela. Cada um destes pontos tem uma variedade estável (que denotamos por H^+) e uma variedade instável (H^-). Em sistemas integráveis, H^+ e H^- podem formar um só arco, com uma junção suave, como mostrado na fig. 2.5a. Tal é o caso do pêndulo, por exemplo.

Em sistemas não-integráveis, por outro lado, as variedades estável e instável em geral se cruzam, como na fig. 2.5b; os pontos de cruzamento são chamados *pontos homoclínicos*. Vamos examinar este cruzamento com mais detalhes.

Aplicando o mapa "twist" T (2.2) (nós não usaremos o subscrito ϵ daqui por diante) no ponto homoclínico X, obtemos o ponto TX. Como X fica no cruzamento de H^+ e H^-, para que a imagem de X seja única, TX deve ficar também em um cruzamento de H^+ e H^-, ou seja, TX também é um ponto homoclínico. Temos então uma situação como a mostrada na fig. 2.6a. Aplicando T no ponto TX, obteremos pelo mesmo argumento um outro ponto homoclínico T^2X (fig. 2.6b). Como o mapa T preserva a área,

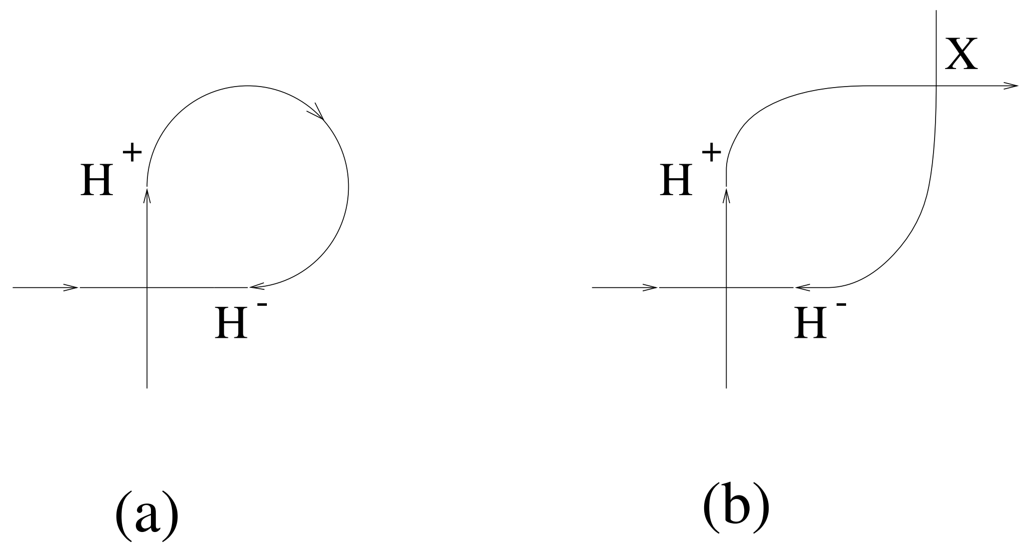

Figura 2.5: H^+ e H^- em sistemas integráveis e não-integráveis.

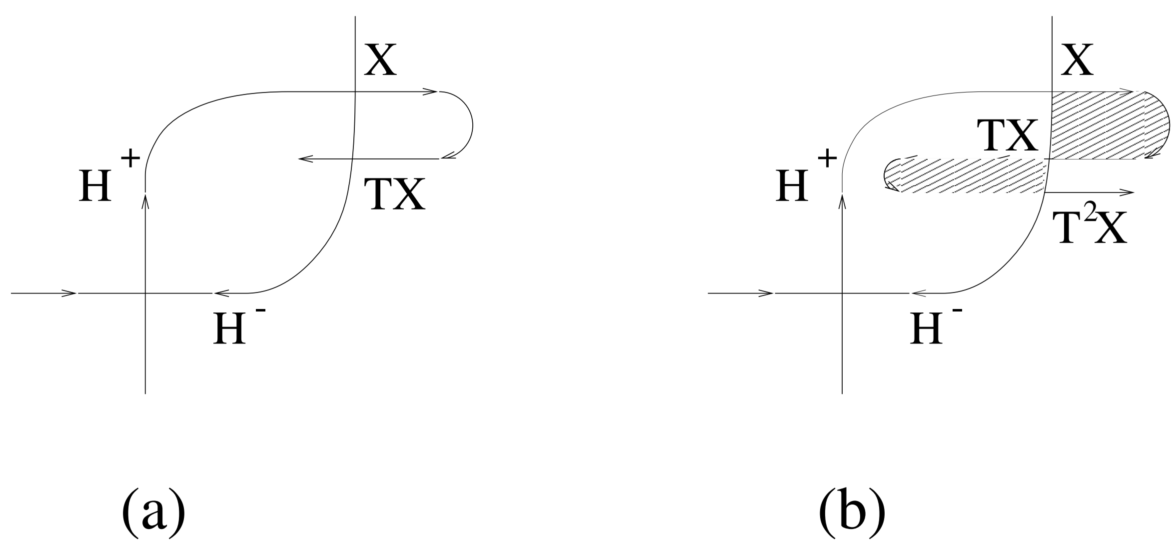

Figura 2.6: Formação do emaranhado homoclínico

as regiões destacadas na fig. 2.6b têm a mesma área; e como os sucessivos pontos $T^n X$ aproximam-se cada vez mais lentamente do ponto hiperbólico H, os loops formados por H^- tornam-se cada vez mais longos e finos. O mesmo acontece com H^+ para T^{-n}. Como H^- e H^+ não sofrem auto-intersecções (pois isto implicaria na não-unicidade do mapa T), vemos que H^+ e H^- formam uma intrincada estrutura com uma topologia não trivial, conhecida como o *emaranhado homoclínico*. Este é a figura que Poincaré não ousou desenhar [13].

Como consequência da existência do emaranhado homoclínico, as trajetórias na vizinhança de pontos de equilíbrio hiperbólicos apresentam um comportamento aparentemente randômico que é a origem da grande sensibilidade às condições iniciais que caracteriza os sistemas caóticos (falaremos um pouco mais sobre isto na seção seguinte).

Completamos assim o estudo de sistemas integráveis fracamente perturbados por termos não-integráveis. A estrutura do espaço de fase está esboçada na fig. 2.4; em torno de cada centro a estrutura se repete, e assim infinitamente em todas as escalas, de forma auto-similar.

2.4 Características do Movimento Caótico

Nesta seção, vamos investigar algumas características que são próprias ao movimento caótico, e que o distinguem do movimento regular.

Se uma trajetória é caótica, ela explora uma região do espaço de fase de dimensionalidade maior que aquela disponível para trajetórias integráveis. Nós já vimos que estas últimas são quase-periódicas: a evolução temporal de qualquer variável dinâmica é expressa como uma série de Fourier com N frequências fundamentais (ver eq.(1.28)). Assim, a transformada de Fourier de qualquer variável dinâmica contém neste caso picos discretos correspondentes às combinações das N frequências fundamentais. Para o movimento caótico, não existem variáveis de ângulo-ação, logo não existe um número finito de frequências fundamentais; ou seja, o movimento caótico não é quase-periódico. A transformada de Fourier de uma trajetória caótica vai revelar, ao invés de alguns picos discretos, um espectro essencialmente contínuo. Esta é uma boa maneira prática de identificar trajetórias caóticas.

Uma outra característica marcante das trajetórias caóticas é a extrema sensibilidade às condições iniciais. Quando a trajetória é integrável, sua evolução temporal em termos das variáveis de ângulo-ação é dada pela eq.(1.24), que descreve uma evolução linear no toro correspondente a uma dada condição inicial. Se escolhermos uma condição inicial vizinha, as duas trajetórias afastam-se linearmente uma da outra. Para trajetórias caóticas, as duas trajetórias em geral afastam-se *exponencialmente* com o tempo. Os N coeficientes λ_i que descrevem a taxa de separação (correspondentes aos N graus de liberdade) são os chamados *expoentes de Liapunov*, e podem ser calculados numericamente. Para órbitas integráveis, todos os expoentes de Liapunov são nulos, e para órbitas caóticas, pelo menos um deles é positivo. A presença de um coeficiente de Liapunov maior que zero causa um rápido afastamento de trajetórias inicialmente próximas, o que é responsável pela grande sensibilidade às condições iniciais.

Para finalizar, analizaremos algumas propriedades estatísticas do movimento caótico. Para isso, definimos primeiramente o conceito de *ergodicidade*. Dada uma certa região do espaço de fase, e uma certa trajetória contida nesta região, dizemos que a trajetória é *ergódica* se ela cobrir uniformemente esta região. Em um sistema integrável com N graus de liberdade, por exemplo, as trajetórias contidas em toros com frequências incomensuráveis são ergódicas no toro (mas não são ergódicas em todo o espaço de fase). A chamada *hipótese ergódica* propõe que trajetórias caóticas de sistemas conservativos são (em geral) ergóicas nas regiões $(2N-1)$-dimensionais do espaço de fase acessíveis a elas.

A ergodicidade de uma trajetória em uma região do espaço de fase implica na igualdade das médias temporal e de ensemble nesta região:

$$\lim_{T\to\infty}\frac{1}{T}\int_0^T f(q(t),p(t))dt = \int dq \int dp f(q,p). \tag{2.5}$$

Vamos agora introduzir um outro conceito, o de *mixing*. Uma trajetória tem a propriedade de mixing em uma dada região do espaço de fase se, dado um volume pequeno (no espaço de fase) em torno de um certo ponto inicial dasta trajetória, a evolução temporal espalhar este volume uniformemente por toda a região. Mais rigorosamente, se Ω é a região à qual a trajetória tem acesso, e sendo V o volume inicial, a trajetória tem mixing se, dada uma região arbitrária W contida em Ω, valer:

$$\lim_{T\to\infty}\frac{\mathrm{vol}(V_T\bigcap W)}{\mathrm{vol}(V)} = \frac{\mathrm{vol}(W)}{\mathrm{vol}(\Omega)}, \tag{2.6}$$

onde V_T é a região no tempo T correspondente à evolução temporal de V, e vol indica o volume no espaço de fase.

Trajetórias integráveis não apresentam “mixing”, pois para estas V é deformado linearmente pela evolução temporal; para trajetórias caóticas, por outro lado, V é deformado exponencialmente, e apesar de sua área ser preservada ($\mathrm{vol}(V) = \mathrm{vol}(V_T)$), ele é “esticado” e deformado até preencher uniformemente a região acessível do espaço de fase.

Capítulo 3

Fractais e Caos em Sistemas Abertos

A maior parte dos estudos em caos são restritos a sistemas dissipativos com atratores e a sistemas hamiltonianos com movimento confinado; para estes dois tipos de sistema, técnicas poderosas foram desenvolvidas, e a caracterização do caos é um problema razoavelmente bem entendido. Neste capítulo, nós vamos investigar a dinâmica de sistemas *abertos*, ou seja, sistemas onde o movimento não é limitado; um exemplo típico são problemas de espalhamento. A caracterização do caos neste tipo de sistema se dá através de estruturas fractais, que é uma caracterização válida na relatividade geral, pois o caráter fractal de um conjunto é uma característica topológica, que não depende de uma particular escolha de coordenadas.

Neste capítulo vamos introduzir a idéia de fractal e de dimensão fractal; falaremos em seguida de sistemas dissipativos com múltiplos atratores, e de como a dimensão fractal entre as diferentes bacias de atração caracteriza um tipo de caos; e finalmente, falaremos do espalhamento caótico.

3.1 Fractais e Dimensão Fractal

A maior parte dos conjuntos geométricos a que estamos acostumados é caracterizada por uma dimensão que é um número inteiro. Assim, um conjunto discreto de pontos tem dimensão 0, uma curva tem dimensão 1, uma superfície tem dimensão 2, etc. Todos estes conjuntos têm em comum a seguinte propriedade: se olharmos para uma região pequena o suficiente, eles são "suaves", ou seja, quanto menor a região que olhamos, mais próxima ela se torna da sua primeira aproximação linear. Assim, uma curva olhada de perto se parece com uma reta, uma superfície se parece com um plano, e assim por diante. Estes conjuntos têm uma escala característica, abaixo da qual nenhuma estrutura aparece, e tudo fica suave.

Em sistemas dinâmicos, no entanto, aparecem conjuntos que apresentam estrutura em *todas* as escalas [14, 15]; para estes conjuntos, não importa o quanto ampliemos uma certa região, ela nunca fica suave. Estes conjuntos são chamados de *fractais*. Para caracterizar suas propriedades de escala, nós usamos uma generalização da definição usual de dimensão que permite que esta tenha valores não-inteiros. Um conjunto é fractal se ele tem uma dimensão não-inteira.

Existem várias maneiras possíveis de definir a dimensão fractal; nós apresentaremos a mais simples, a chamada dimensão "box-counting". Dado um conjunto de pontos que está contido em um espaço euclideano n-dimensional $\mathbf{R}^n$, cobrimos uma região que contém o conjunto com hipercubos de aresta ϵ, com ϵ pequeno. Sendo $N(\epsilon)$ o número de cubos que contém pontos do conjunto, temos em geral uma dependência do tipo:

$$N(\epsilon) \sim \epsilon^{-d}, \tag{3.1}$$

para $\epsilon \to 0$, onde d é por definição a dimensão fractal. Temos então:

$$d = -\lim_{\epsilon \to 0} \frac{\ln N(\epsilon)}{\ln \epsilon}. \tag{3.2}$$

É fácil demonstrar que esta definição dá os resultados corretos para os conjuntos não-fractais: $d = 1$ para uma curva, $d = 2$ para uma superfície, etc. Ela permite, porém, valores não-inteiros; quanto isto acontece, não existe uma aproximação linear para o conjunto, e ele apresenta estrutura em escalas arbitrariamente pequenas. Um exemplo bem conhecido é o conjunto de Cantor, construido através do processo mostrado na fig. 3.1. Mostra-se facilmente que $d = \ln 2/\ln 3 \approx 0.63$ para este conjunto.

O conjunto de Cantor tem claramente estrutura em todas as escalas; além disso, ele goza da propriedade de *auto-similaridade*: qualquer um dos subconjuntos que não são excluídos em um dado estágio da construção (ver fig. 3.1) é igual ao conjunto inteiro, a menos de uma transformação de escala. A maioria das fractais encontrados em física não são auto-similares, e não têm uma regra de construção simples como o conjunto de Cantor. É importante notar

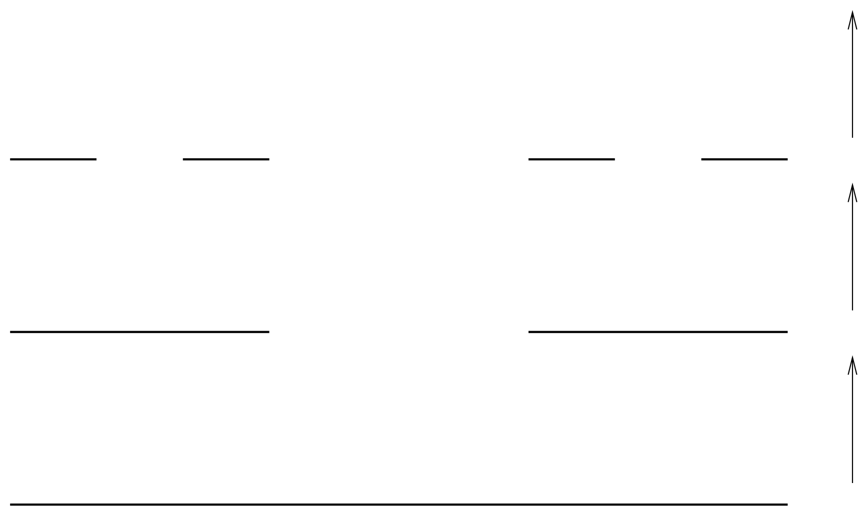

Figura 3.1: Construção do conjunto de Cantor.

também que a fractalidade de um conjunto é uma característica topológica deste, e que é preservada por transformações suaves de coordenadas. Esta propriedade é importante para a caracterização do caos em relatividade geral [16].

3.2 Atratores e Bacias de Atração

Apesar de o nosso interesse principal ser sistemas hamiltonianos, vamos voltar nossa atenção por um momento para sistemas dissipativos com mais de um atrator, pois vários conceitos usados neste tipo de sistema serão úteis mais tarde.

Um sistema dissipativo pode ter um ou mais atratores; cada atrator tem associado a ele uma *bacia de atração*, que é a região do espaço de fase consistindo de condições iniciais de trajetórias atraídas para aquele atrator. A fronteira que divide as diversas bacias de atração é de especial interesse para nós. Esta fronteira pode ter uma estrutura fractal [14], com dimensão maior que $N-1$ (onde N é a dimensão do espaço de fase). Se $d = N-1$, a fronteira é não-fractal. Caso $d > N-1$, então temos uma fronteira fractal. Na região onde a fronteira é fractal, duas ou mais bacias de atração estão entrelaçadas de forma extremamente complexa, em todas as escalas. Se pudermos determinar uma condição inicial apenas dentro de uma certa margem de erro, e se esta condição inicial estiver próxima a uma fronteira fractal, fica difícial determinar a que bacia de atração aquela condição inicial pertence. Assim, o caráter fractal da fronteira entre as bacias de atração implica em uma grande sensibilidade às condições iniciais, no que diz respeito ao destino final das trajetórias. Observamos que os atratores em si podem ser perfeitamente regulares; o caos que estamos estudando manifesta-se na escolha dos atratores para cada condição inicial, e não nos atratores em si.

Os pontos do espaço de fase que pertencem à fronteira não fazem parte de nenhuma das bacias de atração; eles são a variedade estável de um conjunto invariante não-atrator. Este conjunto invariante corresponde às trajetórias que nunca caem em nenhum dos atratores para todos os tempos (passado e futuro). Quando a fronteira é fractal, o conjunto invariante também é fractal.

Para entender a dinâmica por trás da formação de uma fronteira fractal, vamos considerar um mapa 2-dimensional M que age na região mostrada na fig. 3.2. A_- e A_+ são os atratores, e S_0, S_- e S_+ são pontos de sela. Pontos à direita da variedade estável de S_- (ou seja, a curva cd) pertencem à bacia de atração de A_-, e pontos à esquerda de ab pertencem à bacia de atração de A_+. A pergunta é: o que acontece com os pontos da região Q? Para responder esta pergunta, temos que entender a ação de M em Q, que está mostrada esquematicamente na fig. 3.2b; vemos o mecanismo de "stretching and folding" característico de sistemas caóticos.

Sob a ação de M, uma parte da região Q foi parar à direita de cd, fazendo parte portanto da bacia de atração de A_-; trata-se da pré-imagem da região II', ou seja $M^{-1}(II')$, que denotaremos por II. Analogamente, a região $IV = M^{-1}(IV')$ pertence à bacia de atração de A_+. As regiões II e IV estão mostradas na fig. 3.2c. Mas isso não é tudo. A bacia de atração de A_- também contém pontos que são mapeados em II, ou seja, contém também a pré-imagem de II, que é $M^{-1}[II \cap M(Q)]$; do mesmo modo, $M^{-1}[IV \cap M(A)]$ faz parte da bacia de atração de A_+. Estes conjuntos fazem parte das regiões I, III e V, e estão mostrados na fig. 3.2c. O processo continua infinitamente, e o resultado é que as bacias de atração de A_- e A_+ estão infinitamente entrelaçadas em uma estrutura fractal; temos então a formação de uma fronteira fractal.

Como já mencionamos, a fronteira é a variedade estável de um conjunto invariante não-atrator, que pode ser visto como a interseção das suas variedades estável e instável. No caso do mapa da fig. 3.2, o conjunto invariante é formado pela interseção da fronteira (variedade estável) e do conjunto

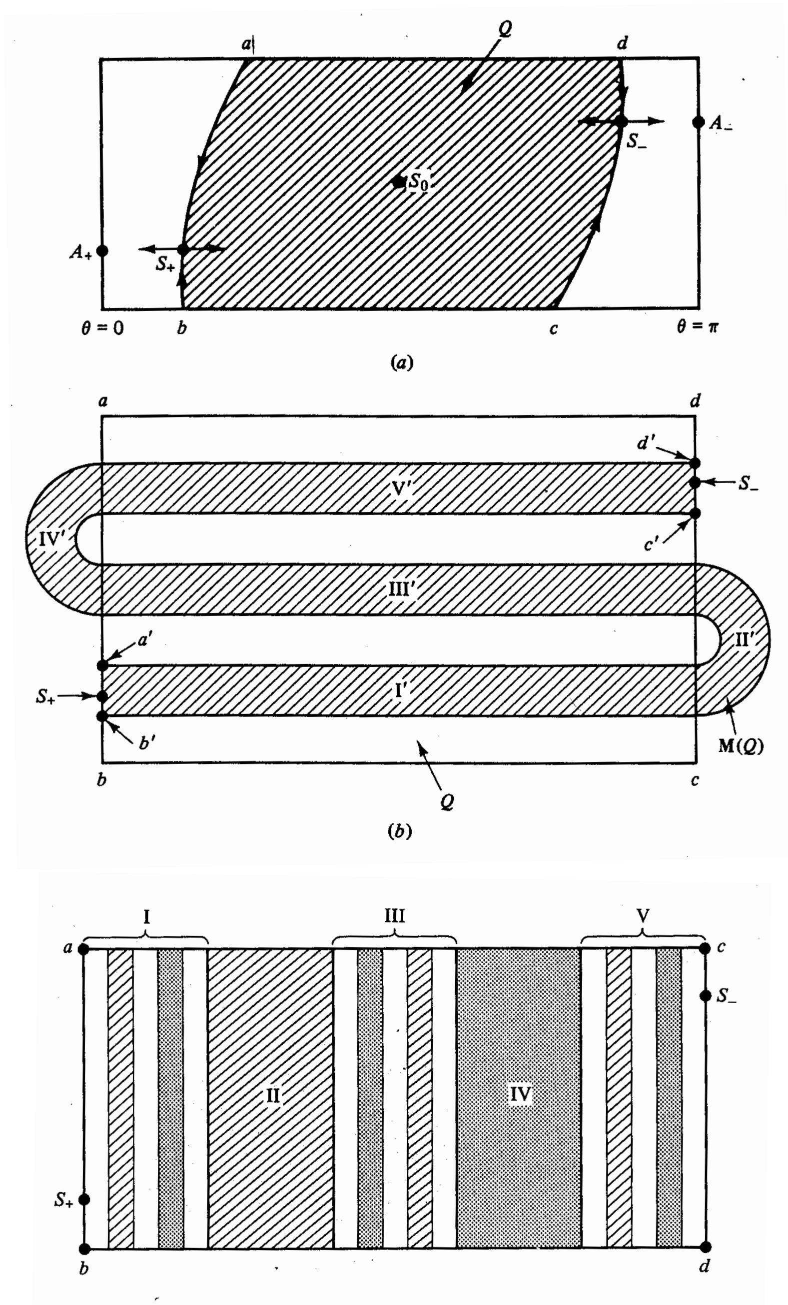

Figura 3.2: (a) e (b): ação do mapa M. (c): passos na construção das bacias de atração; regiões sombreadas fazem parte da bacia de atração de A_+, e regiões hachuradas fazem parte da bacia de atração de A_-.

$M(Q) \cap M^2(Q) \cap M^3(Q) \cap \cdots$.

Vamos tornar quantitativa a sensibilidade às condições iniciais de que falamos acima. Suponha que tenhamos um sistema com dois atratores (para simplificar), e queremos saber para qual deles vai uma certa condição inicial. Esta condição inicial, no entanto, só é conhecida a menos de uma incerteza ϵ; ou seja, a condição inicial "verdadeira" está contida em uma bola N-dimensional de raio ϵ. Denotaremos o centro da bola de x_0. Nós podemos calcular a trajetória partindo de x_0 e ver para qual dos atratores ela vai. Podemos tentativamente dizer que a "verdadeira" condição inicial tem o mesmo destino, ou seja, pertence à mesma bacia de atração que x_0. Há uma chance disto estar errado, quando x_0 está a menos de ϵ de distância da fronteira entre as bacias de atração; chamaremos tais pontos de "incertos". Se ϵ é pequeno e a fronteira não é fractal, estes pontos ocupam um volume proporcional a ϵ; neste caso, se escolhermos pontos randomicamente em uma região do espaço de fase que contenha a fronteira, a fração dos pontos incertos $f(\epsilon)$ é proporcional a ϵ:

$$f(\epsilon) \sim \epsilon. \tag{3.3}$$

Assim, a chance de cometermos erros quanto a que bacia de atração pertence um certo ponto do espaço de fase é diretamente proporcional à incerteza na condição inicial. Este crescimento linear do erro é típico de um sistema regular.

Se a fronteira for fractal com dimensão $d > N - 1$, podemos mostrar que [17]:

$$f(\epsilon) \sim \epsilon^{\alpha}, \qquad \text{com } \alpha = N - d. \tag{3.4}$$

Assim, para uma fronteira fractal $\alpha < 1$, o erro na determinação da bacia de atração decresce mais lentamente com a precisão do que no caso regular. Para dar um exemplo, se $\alpha = 0.1$, $f(\epsilon) \sim \epsilon^{0.1}$; para aumentar a precisão na determinação da bacia de atração de um ponto qualquer em 10 vezes, precisaríamos aumentar a precisão nas condições iniciais em 10^{10} vezes! Assim, se tivermos um ponto próximo à fronteira neste sistema, é praticamente impossível determinar para qual atrator ele vai.

A relação (3.4) pode ser usada para determinar numericamente a dimensão fractal de uma fronteira [17]. Para isso, escolhemos uma região R do espaço de fase que tem uma interseção não-nula com a fronteira. Escolhemos então randomicamente um grande número de pontos em R, e evoluimos numericamente estes pontos para saber a qual das bacias de atração eles pertencem; em seguida, para cada um dos pontos acima nós calculamos a evolução temporal de dois pontos deslocados de $\pm\epsilon$ em uma direção qualquer (não faz diferença qual seja); se pelo menos um deles pertencer a uma bacia de atração diferente da bacia do ponto original, consideramos este ponto como "incerto". Uma fração $g(\epsilon)$ dos pontos escolhidos vai ser "incerta"; das considerações feitas acima, esperamos que $g(\epsilon)$ seja proporcional a $f(\epsilon)$. Repetindo este procedimento para vários valores de ϵ, traçamos um gráfico log-log de $g(\epsilon)$, que deve ser uma reta, com coeficiente angular igual a $\alpha = N - d$. Determinamos desta maneira a dimensão fractal da fronteira.

3.3 Escape Caótico

Vamos agora estudar uma importante manifestação do caos em sistemas abertos (ou seja, sistemas onde as trajetórias não são confinadas a um volume finito no espaço de fase), que é o escape caótico [14, 18]. Para simplificar a exposição, vamos nos restringir a sistemas com dois graus de liberdade.

Considere um sistema hamiltoniano com dois graus de liberdade, tal que o potencial $V(x, y)$ apresente dois ou mais escapes distintos para energias acima de um certo valor crítico E_0. Para exemplificar, a fig. 3.3 mostra algumas curvas de nível do potencial de Hénon-Heiles, que é investigado em detalhes no artigo reproduzido no Apêndice A, e que é dado por [10]:

$$V(x, y) = \frac{1}{2}\left(x^2 + y^2\right) + x^2 y - \frac{1}{3}y^3. \tag{3.5}$$

Como podemos ver na fig. 3.3, o potencial apresenta três escapes para energias suficientemente altas (mais exatamente, para energias tais que $E > E_0 = 1/6$). O escape escolhido por uma partícula-teste vai depender de suas condições iniciais. Para sistemas caóticos (como é o caso do sistema de Hénon-Heiles), o escape pode ter uma grande sensibilidade às condições iniciais. Neste caso, a fronteira no espaço de fase entre as condições iniciais correspondendo a diferentes escapes é fractal, em analogia com o caso de diferentes bacias de atração analizado na seção anterior. Assim como naquele caso, a sensibilidade às condições iniciais é quantificada pela dimensão box-counting.

Uma situação análoga ao escape caótico é o espalhamento caótico [19]; a diferença básica entre os dois casos são as condições iniciais da partícula-teste, e o fato de que os potenciais de espalhamento só exercem uma influência apreciável no movimento das partículas em uma certa região finita do espaço.

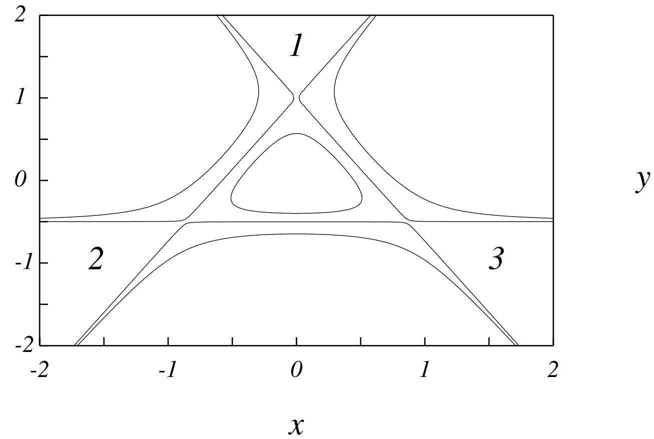

Figura 3.3: Curvas equipotenciais para o potencial de Hénon-Heiles.

Capítulo 4

Relatividade Geral

Neste capítulo, fazemos uma breve introdução à relatividade geral, com ênfase na dinâmica de partículas-teste em um dado campo gravitacional descrito por uma métrica espaço-temporal. Veremos como os conceitos de sistemas dinâmicos apresentados nos capítulos anteriores podem ser transportados para sistemas relativísticos. Por último, apresentamos em detalhes o caso de campos gravitacionais estacionários axisimétricos, que têm grande importância para o restante da tese.

4.1 Dinâmica em Relatividade Geral

O elemento essencial usado na construção do formalismo da relatividade geral é o contínuo espaço-temporal, composto de três dimensões espaciais e uma dimensão temporal. Usaremos a convenção de denotar coordenadas relativas às dimensões espaciais por x^1, x^2, x^3, e aquelas relativas à dimensão temporal por x^0. Também usaremos o sistema de unidades usual em relatividade geral, no qual a velocidade da luz e a constante gravitacional de Newton têm valor unitário:

$$c = 1; \qquad G = 1. \tag{4.1}$$

Um dos princípios fundamentais da relatividade geral é o princípio de equivalência, que diz que qualquer campo gravitacional pode ser localmente anulado por uma transformação de coordenadas adequada. Do ponto de vista de um observador no novo sistema de coordenadas, não existe campo gravitacional, pois este se encontra em queda livre[1]. O princípio de equivalência leva naturalmente à formulação do espaço-tempo como uma variedade pseudo-riemaniana quadridimensional com métrica com assinatura do tipo Minkowski [20]. A métrica é descrita pelo tensor $g_{\mu\nu}$, que é simétrico e de 'rank' 2. Índices gregos por convenção assumem valores de 0 a 3. Também adotaremos a convenção de que índices repetidos são somados. Dois pontos vizinhos no espaço-tempo definem através da métrica uma "distância" dada por:

$$ds^2 = g_{\mu\nu} dx^\mu dx^\nu. \tag{4.2}$$

Como a métrica não é positiva-definida, ds^2 pode ser positivo, negativo ou nulo. Em geral, $g_{\mu\nu}$ é função de todas as quatro coordenadas x^α.

No formalismo relativístico, o campo gravitacional é associado à curvatura do espaço-tempo. A curvatura é medida pelo tensor de curvatura de Riemann $R^\alpha_{\beta\gamma\delta}$, dado por:

$$R^\alpha_{\beta\gamma\delta} = \frac{\partial \Gamma^\alpha_{\beta\delta}}{\partial x^\gamma} - \frac{\partial \Gamma^\alpha_{\beta\gamma}}{\partial x^\delta} + \Gamma^\alpha_{\mu\gamma}\Gamma^\mu_{\beta\delta} - \Gamma^\alpha_{\mu\delta}\Gamma^\mu_{\beta\gamma}, \tag{4.3}$$

onde os $\Gamma^\alpha_{\beta\gamma}$ são os símbolos de Christoffel:

$$\Gamma^\alpha_{\beta\gamma} = \frac{1}{2} g^{\alpha\mu} \left(\frac{\partial g_{\mu\beta}}{\partial x^\gamma} + \frac{\partial g_{\mu\gamma}}{\partial x^\beta} - \frac{\partial g_{\beta\gamma}}{\partial x^\mu} \right). \tag{4.4}$$

Lembramos que índices repetidos são somados de 0 a 3. Índices são abaixados e levantados pelo tensor métrico $g_{\mu\nu}$ e seu inverso $g^{\mu\nu}$, definido por $g_{\alpha\nu} g^{\nu\beta} = \delta^\beta_\alpha$, onde δ^β_α é o delta de Kronecker. Um valor não-nulo de $R^\alpha_{\beta\gamma\delta}$ em algum ponto significa que o espaço-tempo é curvo e há um campo gravitacional presente. Caso $R^\alpha_{\beta\gamma\delta}$ seja nulo em todos os pontos, o espaço é plano e não há nenhum campo gravitacional.

A gravidade é gerada pela distribuição de matéria e energia no espaço, que é por sua vez afetada pelo campo gravitacional. Esta interação mútua entre gravidade e matéria é descrita pela equação de Einstein:

$$G_{\mu\nu} = 8\pi T_{\mu\nu}, \tag{4.5}$$

onde $T_{\mu\nu}$ é o tensor de energia-momento correspondente aos campos materiais existentes no espaço-tempo (excetuando o próprio campo gravitacional). O

[1] Na verdade, o princípio de equivalência não é válido na vizinhança de uma singularidade no espaço-tempo, como as que acredita-se existirem no centro de buracos negros.

tensor de Einstein $G_{\mu\nu}$ é:

$$G_{\mu\nu} = R_{\mu\nu} - \frac{1}{2} g_{\mu\nu} R, \tag{4.6}$$

onde o tensor de Ricci $R_{\mu\nu}$ e o escalar de Ricci R são definidos por:

$$R_{\mu\nu} = R^{\alpha}_{\mu\alpha\nu}; \qquad R = g^{\alpha\beta} R_{\alpha\beta}. \tag{4.7}$$

O tensor de Einstein satisfaz a identidade $\nabla_\mu G^{\mu\nu} = 0$, onde ∇_μ denota a derivada covariante. Pela equação de campo (4.5), devemos ter então

$$\nabla_\mu T^{\mu\nu} = 0, \tag{4.8}$$

que é a equação de movimento dos campos materiais.

As equações (4.5) são um sistema de equações diferenciais parciais não-lineares acopladas, e são em geral impossíveis de ser resolvidas analiticamente. Soluções exatas são encontradas apenas em casos muito particulares, em geral em situações onde o espaço-tempo tem grande simetria [22], como no caso dos campos estáticos axisimétricos que trataremos na seção seguinte.

Consideremos agora um dado campo gravitacional, descrito pela métrica $g_{\mu\nu}$. O movimento de uma partícula-teste neste campo é determinado pela extremização do funcional $\int ds$, onde ds é dado por (4.2). A equação de movimento resultante é a equação da geodésica:

$$\ddot{x}^\mu + \Gamma^{\mu}_{\alpha\beta} \dot{x}^\alpha \dot{x}^\beta = 0, \tag{4.9}$$

onde $\dot{x}^\mu = dx^\mu / d\lambda$ é a derivada em relação a um parâmetro afim λ da trajetória, que no caso de partículas massivas pode ser identificado com o tempo próprio de um observador que acompanha a partícula. A equação (4.9) pode ser derivada da equação de movimento geral de campos materiais (4.8) no caso limite em que o campo está concentrado em uma pequena região do espaço.

As equações (4.9) podem ser derivadas da Lagrangeana

$$L = \frac{1}{2} g_{\mu\nu} \dot{x}^\mu \dot{x}^\nu, \tag{4.10}$$

através da equação de Euler-Lagrange:

$$\frac{d}{dt} \frac{\partial L}{\partial \dot{x}^\mu} - \frac{\partial L}{\partial x^\mu} = 0. \tag{4.11}$$

As equações de movimento também podem ser escritas em forma hamiltoniana:

$$\frac{dx^\mu}{ds} = \frac{\partial H}{\partial p_\mu}; \qquad \frac{dp_\mu}{ds} = -\frac{\partial H}{\partial x^\mu}, \tag{4.12}$$

onde os momentos conjugados são dados por:

$$p_\mu = g_{\mu\alpha} p^\alpha; \qquad p^\mu = m_0 dx^\mu/ds, \tag{4.13}$$

onde m_0 é a massa de repouso da partícula-teste. e a hamiltoniana é:

$$H = \frac{1}{2} g^{\mu\nu} p_\mu p_\nu. \tag{4.14}$$

Note que a hamiltoniana é simplesmente a Lagrangeana reescrita em termos das variáveis conjugadas x^μ e p_μ, pois esta tem apenas termos cinéticos. Vemos assim que os conceitos de integrabilidade e caos em sistemas hamiltonianos que apresentamos nas seções anteriores podem ser aplicados diretamente ao movimento de partículas-teste em campos gravitacionais relativísticos.

Uma consequência imediata das equações (4.12) é que se a métrica $g_{\mu\nu}$ não depende de uma das variáveis x^α, ou seja se $\partial g_{\mu\nu}/\partial x^\alpha = 0$, então p_α é uma quantidade conservada pelo movimento, $p_\alpha = \text{const}$. Como a hamiltoniana não depende explicitamente do parâmetro afim da geodésica, esta é automaticamente conservada. Temos então a constante de movimento:

$$H = \text{const} = \frac{1}{2} g^{\mu\nu} p_\mu p_\nu \equiv \frac{1}{2} m_0^2, \tag{4.15}$$

No caso do movimento de raios de luz, ou outras partículas sem massa, o momento conjugado é definido por $\Pi^\mu = dx^\mu/d\lambda$, onde λ é um parâmetro afim, e $H = 0$.

4.2 Métricas Estáticas Axisimétricas

Em um espaço-tempo com simetria axial e com simetrias de translação e inversão temporal, é possível definir coordenadas tais que a métrica é escrita na forma [21, 22]:

$$ds^2 = e^{2\psi} dt^2 - e^{-2\psi} \left[e^{2\gamma}(dr^2 + dz^2) + r^2 d\phi^2 \right], \tag{4.16}$$

onde o eixo z é o eixo de simetria axial, e r é a coordenada radial cilíndrica. ϕ é o ângulo em torno do eixo de simetria z, e t é a coordenada temporal.

r, z, ϕ e t são as *coordenadas de Weyl.* ψ e γ são funções de r e z apenas. A métrica (4.16) não depende das coordenadas t e ϕ, o que é consequência direta das simetrias impostas sobre o espaço-tempo.

Usando a forma (4.16) para a métrica, as equações de Eintein reduzem-se a:

$$\frac{\partial^2\psi}{\partial r^2} + \frac{1}{r}\frac{\partial\psi}{\partial r} + \frac{\partial^2\psi}{\partial z^2} = 0; \tag{4.17}$$

$$d\gamma = r\left[\left(\frac{\partial\psi}{\partial r}\right)^2 - \left(\frac{\partial\psi}{\partial z}\right)^2\right]dr + 2r\frac{\partial\psi}{\partial r}\frac{\partial\psi}{\partial z}dz. \tag{4.18}$$

A eq. (4.17) é a equação de Laplace em coordenadas cilíndricas; isto automaticamente garante a integrabilidade de (4.18). O problema resume-se então a resolver a eq. (4.17), e então calcular γ integrando a eq. (4.18).

Observamos que apesar de as coordenadas r e z usadas em (4.16) serem convenientes em um espaço-tempo axisimétrico, devemos ter cuidado com sua interpretação, e não se deve cair no erro de pensar nelas como coordenadas cilíndricas usuais. Para exemplificar escrevemos a métrica de Schwarzschild (que descreve um buraco negro esfericamente simétrico sem carga e rotação) nas coordenadas de Weyl:

$$\psi = \frac{1}{2}\ln\frac{R_+ + R_- - 2m}{R_+ + R_- + 2m}, \tag{4.19}$$

onde

$$R_\pm^2 = r^2 + (z \pm m)^2. \tag{4.20}$$

Interpretando r e z como coordenadas cilíndricas em um espaço euclideano, este campo representa uma barra de densidade linear uniforme no eixo z, com massa total igual a m. Na verdade, a eq. (4.19) representa o campo gravitacional esfericamente simétrico de uma massa puntual, como revela a transformação de coordenadas definida por:

$$r = \sqrt{R(R-2)}\sin\theta; \tag{4.21}$$

$$z = (R-1)\cos\theta. \tag{4.22}$$

Nas novas coordenadas R e θ a métrica é:

$$ds^2 = \left(1 - \frac{2m}{R}\right)dt^2 - \frac{dR^2}{1-\frac{2m}{R}} - R^2 d\Omega^2, \tag{4.23}$$

onde $d\Omega^2 = d\theta^2 + \sin^2\theta d\phi^2$. Esta é a métrica de Schwarzschild, e as coordenadas R,θ,ϕ tornam evidente a simetria esférica. Note que a "barra" na eq. (4.19) é o horizonte de eventos $R = 2m$ do buraco negro; assim, a região do espaço-tempo no interior do horizonte de eventos não é mapeada pelas coordenadas de Weyl r,z.

Está claro das eqs. (4.16) e (4.17) que a função métrica ψ tende ao potencial gravitacional newtoniano no limite de campos fracos ($|\psi| \ll 1$). Além disso, no caso de métricas assintoticamente planas, a coordenada temporal t é o tempo medido por um observador no infinito.

A solução geral da equação de Laplace axisimétrica (4.17) pode ser escrita como uma expansão em polinômios de Legendre:

$$\psi = \sum_{n=0}^{\infty} \left\{ a_n R^n + b_n R^{-(n+1)} \right\} P_n(\cos\theta), \tag{4.24}$$

onde $R^2 = z^2 + r^2$, e $\cos\theta = z/R$. Os coeficientes a_n e b_n são proporcionais aos momentos de multipolo da distribuição de massa responsável pelo campo, no caso newtoniano. Esta identificação não pode ser feita em geral no caso relativístico, pelas razões apresentadas acima. De fato, se expandirmos a função ψ da métrica de Schwarzschild (4.19), encontramos $b_n \neq 0$ para todos os n pares, quando de fato o campo é puramente monopolar, como pode ser demonstrado por um cálculo relativístico dos momentos multipolares [23].

Uma outra maneira conveniente de escrever as soluções da eq. (4.17) é através de coordenadas prolatas esferoidais, u,v, definidas por:

$$z = uv; \tag{4.25}$$

$$r^2 = (u^2 - 1)(1 - v^2); \tag{4.26}$$

$$u \geq 1; \qquad -1 \leq v \leq 1. \tag{4.27}$$

Nestas coordenadas, a equações de Laplace (4.17) fica:

$$\frac{\partial}{\partial u}\left[(u^2 - 1)\frac{\partial\psi}{\partial u}\right] + \frac{\partial}{\partial v}\left[(1 - v^2)\frac{\partial\psi}{\partial v}\right] = 0. \tag{4.28}$$

Esta equação é imediatamente separável, e a solução geral é escrita em termos de polinômios de Legendre:

$$\psi = \sum_{n=0}^{\infty} \left[a_n Q_n(u) + b_n P_n(u)\right]\left[c_n Q_n(v) + d_n P_n(v)\right]. \tag{4.29}$$

Devido às simetrias axial e temporal, temos duas quantidades conservadas ao longo do movimento de partículas-teste no campo (4.16), que são identificadas como a projeção do momento angular no eixo de simetria (eixo z nas coordenadas de Weyl) $\hat{L}_z$ e a energia da partícula $\hat{E}$:

$$\hat{E} = p_t = m_0 e^{2\psi} \dot{t}; \tag{4.30}$$

$$\hat{L}_z = p_\phi = -m_0 r^2 e^{-2\psi} \dot{\phi}. \tag{4.31}$$

Além disso, temos a lei de conservação (4.15), que representa a conservação da massa de repouso m_0 da partícula-teste, e que é escrita na forma:

$$\hat{E}^2 e^{-2\Psi} - \hat{L}_z^2 r^{-2} e^{2\Psi} - m_0^2 e^{2(\gamma-\Psi)} \left(\dot{r}^2 + \dot{z}^2\right) = m_0^2. \tag{4.32}$$

Conclusão

Neste tese estudamos a dinâmica de sistemas dinâmicos hamiltonianos abertos, quando o sistema apresenta escapes, com particular ênfase no movimento de partículas-teste em campos gravitacionais, tanto relativísticos como newtonianos. O caos nestes sistemas se manifesta através de uma fronteira fractal que separa as condições iniciais no espaço de fase correspondendo a diferentes escapes. A sensibilidade às condições iniciais associada à existência da fronteira fractal é medida pela dimensão fractal (box-counting) da fronteira. Nós determinamos a existência de fronteiras fractais e investigamos o seu comportamento como função dos vários parâmetros físicos para vários sistemas: o sistema de Hénon-Heiles para energias acima da energia de escape (Apêndice A), o sistema composto por um halo de matéria cercando uma região interior vazia (Apêndice B) ou com um buraco negro central (Apêndice C), e um sistema idealizado composto por dois buracos negros distantes (Apêndice D), onde pudemos determinar rigorosamente a existência de uma dinâmica simbólica e de caos transiente.

A dinâmica de sistemas com caos transiente ainda é bastante inexplorada, especialmente em sistemas da relatividade geral, o que deixa em aberto muitas direções por onde o estudo apresentado aqui pode ser continuado. Uma extensão natural do modelo buraco negro central + halo apresentado no Apêndice C é incluir momento angular no buraco negro, o que é fisicamente mais realista, visto que a grande maioria dos objetos astrofísicos conhecidos tem rotação. Existem soluções exatas das equações de Einstein representando um buraco negro de Kerr e um halo, e estas podem ser usadas para investigar a dinâmica neste sistema [25]. Do ponto de vista dinâmico, a introdução de rotação quebra a simetria por inversão temporal, e deve por isso resultar em uma dinâmica diferente (e mais rica) que no caso sem rotação.

Além do modelo buraco negro + halo, existem outros modelos que aproximam distribuições de matéria encontrados em astrofísica; um deles é o modelo de disco, usado para descrever galáxias espirais ou discos de acresção de buracos negros. A dinâmica nestes sistemas para regimes abertos ainda não foi estudada (há estudos da dinâmica confinada, usando seções de Poincaré [24]).

Uma outra via de investigação é o estudo de sistemas não-axisimétricos, onde temos três graus de liberdade, e a dinâmica ocorre em um espaço de fase de cinco dimensões (em sistemas conservativos). A dinâmica de sistemas de mais de dois graus de liberdade é ainda quase totalmente desconhecida, e temos aqui inúmeras possibilidades de investigação.

Bibliografia

[1] L. D. Landau, E. Lifchitz, *Mécanique*, MIR, Moscow (1984)

[2] H. Goldstein, *Classical Mechanics*, Addison-Wesley, New York (1980)

[3] E. T. Whittaker, *A Treatise on the Analytical Dynamics of Particles and Rigid Bodies*, Cambridge University Press, Cambridge, UK (1970)

[4] V. I. Arnold, *Méthodes Mathematiques de la Mécanique Classique*, Mir, Moscow (1984)

[5] V. I. Arnold, *Dynamical Systems III*, Springer-Verlag, New York (1980)

[6] M. Tabor, *Chaos and Integrability in Nonlinear Dynamics*, John Wiley & Sons, New York (1989)

[7] M. V. Berry, "Regular and Irregular Motion", *AIP Conference Proceedings*, **46**, 16 (1978)

[8] B. Doubrovine, S. Novikov, A. Fomenko, *Géometrie Contemporaine — Méthodes et Applications (*2^{eme} *partie)*, Mir, Moscow (1982)

[9] J. Moser, "Is the Solar System Stable?", *Math. Intelligencer*, **1**, 65 (1978)

[10] M. Henon, C. Heiles, "The Applicability of the Third Integral of Motion: Some Numerical Experiments", *Astron. J.*, **69**, 73 (1964)

[11] L. D. Landau, E. Lifchitz, *Théorie du Champ*, Mir, Moscow (1984)

[12] C. Moller, *The Theory of Relativity*, Oxford University Press, Oxford (1966)

[13] H. Poincaré, *Les Méthodes Nouvelles de la Mécanique Celeste*, Gauthier-Villars, Paris (1966)

[14] E. Ott, *Chaos in Dynamical Systems* Cambridge University Press, Cambridge, UK (1993)

[15] J. Guckenheimer e P. Holmes, *Nonlinear Oscilations, Dynamical Systems, and Bifurcations of Vector Fields*, Springer-Verlag, New York (1990)

[16] K. Ferraz, G. Francisco, G. E. A. Matsas, "Chaotic and non-chaotic behavior in the mixmaster dynamics", *Phys. Lett. A*, **156**, 407 (1991)

[17] C. Grebogi, S. W. McDonald, E. Ott e J. A. Yorke, "Final state sensitivity: an obstruction to predictability", *Phys. Lett. A*, **99**, 415 (1983)

[18] S. Bleher, C. Grebogi, E. Ott and R. Brown, "Fractal boundaries for exit in Hamiltonian dynamics", *Phys. Rev. A*, **38**, 930 (1988)

[19] B. Eckhardt, "Irregular scattering", *Physica D*, **33**, 89 (1988)

[20] C. W. Misner, K. S. Thorne, J. A. Wheeler, *Gravitation*, W. H. Freeman and Company, New York (1973)

[21] H. P. Robertson, T. W. Nooman, *Relativity and cosmology*, W. B. Saunders Company, Philadelphia (1969)

[22] D. Kramer, H. Stephani, M. MacCallum and E. Herlt, *Exact solutions of Einstein's field equations*, Cambridge University Press, Cambridge (1980).

[23] H. Quevedo, "General static axisymmetric solution of Einstein's vacuum field equations in prolate spheroidal coordinates", *Phys. Rev. D*, **39**, 2904 (1989)

[24] A. Saa, R. Venegeroles, "Chaos around the superposition of a black-hole and a thin disk", *Phys. Lett. A*, **259**, 201 (1999)

[25] P. S. Letelier, W. M. Vieira, "Chaos and rotating black holes with halos", *Phys. Rev. D*, **56**, 8095 (1997)

Apêndice A

"Fractal Basins in Hénon-Heiles and Other Polynomial Potentials"

Reprodução do artigo "Fractal Basins in Hénon-Heiles and Other Polynomial Potentials", publicado em Physics Letters A **256**, 362 (1999).

Fractal Basins in Hénon-Heiles and other Polynomial Potentials

Alessandro P. S. de Moura
Instituto de Física Gleb Wataghin, UNICAMP, 13083-970
Campinas SP, Brazil

Patricio S. Letelier
Instituto de Matemática, Estatística e Ciência da Computação,
Departamento de Matemática Aplicada, UNICAMP,
13083-9790 Campinas SP, Brazil

Abstract

The dynamics of several Hamiltonian systems of two degrees of freedom with polynomial potentials is examined. All these systems present unbounded trajectories escaping along different routes. The motion in these open systems is characterized by a fractal boundary (and its corresponding fractal dimension) separating the basins of the escape routes. The fractal (basin boundary) dimensions for these systems are studied in some detail.

A.1 Introduction

The phenomenon of chaos in the escape of particles in Hamiltonian systems is well known in the field of dynamical systems, in particular in systems of two degrees of freedom with polynomial potentials, and has been intensively investigated in astrophysics (see for instance, [1] and references therein) and recently in general relativity [2, 3]. In these systems a test particle can escape from an inner region of the potential to infinity through several distinct escape routes. The escape route chosen by the particle is a function of its initial conditions. If this function has a fractal structure in phase space, the system is said to be chaotic, in the sense that the escape route followed by the particle depends strongly on the initial condition, i.e., a small change in the initial conditions can produce a considerable change in the particle motion. This sensibility to initial conditions can be quantified by the "box-counting" dimension or other topological dimensions of the boundary between regions corresponding to different escape routes [4].

In this communication, we study numerically some Hamiltonian systems of interest to astrophysics and general relativity that have escapes. The main tool used is the box-counting dimension. In section 2, we introduce some standard concepts employed to study open trajectories in Hamiltonian systems: invariant sets, basin boundaries, and box-counting dimension. We examine unbounded motions of the classical Hénon-Heiles system [5]. In section 3, we consider two galactic potentials extensively studied by Contopoulos and collaborators [1], in particular we compute the box-counting dimension for these systems. In section 4, we study a class of homogeneous models for which some rigorous analytic results about the existence of chaotic motion are known [6, 7]. Recently, these systems have been considered in connection with the motion of test particles in a plane fronted gravitational wave (pp wave) [2, 3]. In the last section our main results are discussed.

A.2 Hénon-Heiles System

Since it was first proposed as an idealized model for the potential of an axisymmetric galaxy, the Hénon-Heiles (HH) model gained life of its own and became a paradigm of chaotic Hamiltonian dynamics. Even though it is one of the simplest non-linear two-degrees-of-freedom Hamiltonians it shows the full complexity of chaotic dynamics [5].

The study of orbits of the HH model have been limited mainly to energies below the escape energy E_c, i.e., bounded motions. However, it is natural to investigate the dynamics for energies above E_c. We expect also that chaos be present for unbounded motions [6].

The HH Hamiltonian is[1]:

$$H = \frac{1}{2}\left(p_x^2 + p_y^2\right) + V(x, y), \tag{A.1}$$

$$V(x, y) = \frac{1}{2}\left(x^2 + y^2\right) + x^2 y - \frac{1}{3}y^3, \tag{A.2}$$

[1] Potential V in eq. (A.2) is a special case of the general potential $V_\lambda = \frac{1}{2}(x^2 + y^2) + \lambda(x^2 y - \frac{1}{3}y^3)$, where λ is a real parameter that measures the strength of the cubic terms responsible for chaotic behavior. In this article, we shall restrict ourselves to the standard choice $\lambda = 1$

where $p_x = \dot{x}$ and $p_y = \dot{y}$ are the conjugate momenta to x and y . The escape energy is $E_c = 1/6$. When $E < E_c$, the equipotentials $V(x, y) = E$ are closed curves and the motion is bounded. In limit case $E = E_c$ the equipotential is an equilateral triangle. For $E > E_c$, the vertices of the triangle open and the particles can escape. In fig. 1 we show the contour lines of the potential (A.2) for different values of E. For energies above 1/6 we have three escapes that we label 1, 2 and 3.

For an energy above E_c, the escape chosen by a particular orbit is a function of the initial conditions of this orbit, i.e., it is a function of the accessible phase space. The set of initial conditions leading to escape through the opening i (where i is one of the values 1, 2 or 3) is defined as the *basin* of the escape i. We observe that if the initial conditions are chosen in the inner region bound by the three openings and the equipotential curve, a trajectory directed outwards passing through any one of the openings will never return, due to the form of $V(x, y)$, so the basins are well defined for this region.

We have chaos in this system when the basin boundaries are fractal [4]. The sensitivity to different initial conditions is quantified by the topological dimension d of the set of initial conditions belonging to the basin, which is non-integer for a fractal basin boundary (FBB). Many systems have been shown to have FBBs [1, 8, 9].

In order to have a picture of the structure of the basins in phase space, we chose a 2-dimensional subset $\mathcal{S}$ of the 3-dimensional accessible phase space at a fixed energy E, defined by a segment $|x| \le a$ (where a is a length to be chosen appropriately) and $y = 0$. For each point in the segment, the modulus of the velocity $(\dot{x}^2 + \dot{y}^2)^{1/2}$ is fixed by the energy,

$$(\dot{x}^2 + \dot{y}^2)^{1/2} \equiv v = (2E - V(x, 0))^{1/2} = \left(2E - x^2\right)^{1/2}. \tag{A.3}$$

The direction of the velocity is a free parameter. Hence $\mathcal{S}$ is topologically equivalent to a segment of a cylinder, therefore it can be parameterized by x and θ, where θ is the angle of the velocity with respect to the x-axis,

$$\dot{x} = v \cos\theta, \qquad \dot{y} = v \sin\theta. \tag{A.4}$$

To obtain a picture of the basins in $\mathcal{S}$, we chose $a = 0.5$ (for $E = 0.3$), and we divided the intervals $-a \le x \le a$ and $0 \le \theta \le 2\pi$ into 500 parts each, and thus create a 500×500 grid of initial conditions in $\mathcal{S}$. We integrate numerically the equations of motion for each of these points until they leave through one of the openings; we know then to which basin each point in the grid belongs.

We obtain in this way a (finite resolution) portrait of the basin structure in $\mathcal{S}$. The result for $E = 0.3$ and $a = 0.5$ is shown in fig. 2a, with the following color-code: black regions belong to basin 1 (escape to $y \to +\infty$), grey regions belong to basin 2 (escape to $x \to -\infty$, $y \to -\infty$), and white regions belong to basin 3 (escape to $x \to +\infty$, $y \to -\infty$), see fig. 1. The magnification of a tiny region of fig. 2a is shown in fig. 2b. Therefore we have a complex mixing of the basins down to very small scales, which is an indication of the presence of a FBB. We proceed to calculate the box-counting dimension of the basin boundary [4] . To do this, we take a large number of initial conditions (x_0, θ_0) chosen randomly in $\mathcal{S}$. For each of these initial conditions we integrate the equations of motion and see to which basin it belongs. Then we pick for each (x_0, θ_0) the two initial conditions: $(x_0 + \epsilon, \theta_0)$ and $(x_0 - \epsilon, \theta_0)$, where ϵ is a given (small) number, and find their basins in the same way. When they do not belong to the same basin as the original point (x_0, θ_0) the point (x_0, θ_0) is labeled "uncertain". The fraction $P(\epsilon)$ of uncertain points as a function of the displacement ϵ can be shown to scale as

$$P(\epsilon) \propto \epsilon^{D-d}, \tag{A.5}$$

where D is the dimension of the ambient space (2 in our case) and d is the box-counting dimension of the intersection of the basin boundary with $\mathcal{S}$. We calculate d from a plot of $\ln P$ versus $\ln \epsilon$: this should be a straight line, and its inclination gives $D - d$. If the basin boundary is not fractal, we have $d = D - 1$; otherwise, $d > D - 1$. For $E = 0.3$, we found $d = 1.63 \pm 0.02$, showing that the basin boundary is indeed fractal.

The basin boundary is composed by the set of unstable trapped orbits, which is the stable manifold of an unstable invariant set (a *repellor set*), which is made of unstable orbits that do not escape for both $t \to -\infty$ and $t \to +\infty$. If the invariant set is fractal (that is, if we have a *strange repellor*), the basin boundary will also be fractal. Orbits starting near a FBB will follow the stable manifold of the repellor, will stay near it for long times (the particle bouncing back and forth many times in the inner region without escaping) and will finally escape following a trajectory near its unstable manifold. We have thus associated with the chaos in the choice of the escape, a chaos in the time of escape. This is illustrated in fig. 3, which shows the escape time versus the angle θ of the initial velocity for $x = 0$. The blow-up in fig. 3b shows the dramatic sensitivity to the initial conditions. We observe that since the escape time depends on when we consider an orbit to have escaped (in the case of figs. 3, orbits are considered to have escaped when $\sqrt{x^2+y^2} > 10$), it is to some extent arbitrary. Nevertheless, the structure observed in figs. 3 is independent on this choice. We observe that there is an almost-repeating pattern discernible in figs. 3, but the fractal nature of the picture makes a detailed comparison difficult.

In order to have a picture of how the FBB arises as a result of the dynamics of the system, we define the *twist number* n of an orbit $(x(t), y(t))$ as the number of times it crosses the phase-space surface of section $\mathcal{P}$ given by $\dot{y} = 0$ in the negative direction (that is, with $\ddot{y} < 0$) before escaping. If we take initial conditions on $\mathcal{S}$, there is a subset that corresponds to orbits with $n = 0$ that escape without ever crossing $\mathcal{P}$ in the negative direction; some orbits, on the other hand, cross $\mathcal{P}$ at least once; these have $n \geq 1$. We denote by I_k the set of initial conditions on $\mathcal{S}$ that generate orbits with $n \geq k$. We have the obvious hierarchical relation:

$$I_1 \supset I_2 \supset I_3 \supset \cdots. \tag{A.6}$$

The limit $\lim_{k\to+\infty} I_k$ is the restriction to $\mathcal{S}$ of the stable manifold of the repellor, that is, the FBB. The construction of the FBB can be followed in figs. 4a, 4b and 4c, which show I_1, I_2 and I_3 for $E = 0.3$ with the same grid used in fig. 2a. Every step $I_n \to I_{n+1}$ is made by taking out from I_n ever thinner intercalated strips, in a process identical to the construction of the Cantor set. This is the mechanism responsible for the creation of the FBB. The construction of the repellor can be followed in a similar way: defining R_k as the set of initial conditions in $\mathcal{S}$ that have crossed $\mathcal{P}$ at least k times (in the negative direction) for both directions of time before escaping, the limit $\lim_{k\to+\infty} I_k$ is the repellor set. In fig. 4d we show R_2. The division of phase space into regions corresponding to different twist numbers also has a fractal structure which is intimately connected to the structure of the escape basins. In fact, a calculation of the box-counting dimension for the boundary between the regions I_n yields exactly the same value d as that obtained for the basin boundary.

All the previous discussion was limited to a fixed value of the energy. It is also interesting to investigate how the dynamics changes as we vary E while keeping $E > E_c$. For $E \to E_c$, the openings in the equipotentials are small, and a particle typically bounces back and forth many times before it escapes.

We accordingly expect that the chaos is more intense (or that d is larger) as we lower the energy towards E_c. We have found that this is indeed the case. In fig. 5, we show how the box-counting dimension varies as a function of the energy, for E near E_c. As we expected, d is a decreasing function of E, and in the limit $E \to E_c = 0.166...$ it appears to reach the limiting value of 2, which represents maximum chaos. For E near E_c, d depends approximately linearly on E.

In fig. 6 we show the dependency of d on E for large values of E. It is clear from this figure that as $E \to +\infty$ d decreases monotonically to a limiting value $d_l \approx 1.2$, instead of tending to 1, as might have been expected. To understand this behavior, consider the homogeneous potential:

$$V_0(x, y) = x^2 y - \frac{1}{3} y^3, \tag{A.7}$$

obtained from (A.2) by dropping the quadratic terms. $V_0(x, y)$ is a homogeneous polynomial of third degree in x and y. It can be directly verified that for large values of E the level curves of V are well approximated by those of V_0 (attention: this is not true in general!). Thus, we hope that the dynamics of the system (A.7) gives us the motion in the Hénon-Heiles potential (A.2) in the limit $E \to +\infty$.

The equations of motion in a homogeneous potential of degree n are unaltered by the transformation $x \to \lambda x$, $y \to \lambda y$, $t \to t/\sqrt{\lambda}$, $E \to \lambda^n E$, where λ is a real scale factor. This means that in a homogeneous potential all orbits with a given energy are similar to the corresponding orbits with any other energy by the above scale transformation (as long as both energies are of the same sign). Therefore, we have to consider only one value of E in the study of the dynamics of the system. In particular, the box-counting dimension d is a number which depends only on the system, and not on the energy nor any other parameter. We have calculated d for the system (A.7), obtaining the value $d = 1.23 \pm 0.02$. Comparing this with fig. 6 we see that this agrees with the limiting value of d for the HH model for $E \to +\infty$.

A.3 Contopoulos' Potentials

Contopoulos and collaborators [1] studied in some detail the escapes of particles subjected to the two potentials:

$$V_1(x, y) = \frac{1}{2}\left(x^2 + y^2\right) - \epsilon x^2 y^2, \tag{A.8}$$

$$V_2(x,y) = \frac{1}{2}\left(x^2 + y^2\right) - \epsilon x y^2, \tag{A.9}$$

where ϵ is a free parameter.

The first potential V_1 has closed equipotential curves (and therefore bounded motion) for $0 \leq E \leq 1/4\epsilon$. For $E > E_c = 1/4\epsilon$, the equipotentials open, and the system has four distinct escapes. We have calculated the box-counting dimension in this system as a function of the energy for $\epsilon = 1$, by the same procedure we used in the Hénon-Heiles Hamiltonian. The result is shown in fig. 7. We see that, as in the HH case, d is a generally decreasing function of E, and we have also verified that it goes to the limiting value of 2 as E approaches the escape energy E_c. However, as opposed to the HH case, d tends to 1 for large E, that is, the basin boundaries become regular (non-fractal) for large E.

The second potential V_2 has only two escapes above its escape energy, but it has shown very similar features to the earlier case. In particular, $d \to 2$ as $E \to E_c$, and $d \to 1$ as $E \to \infty$. We remark that for both potentials studied in this section, the approximation of dropping the quadratic terms from the potential (used in section 2) does not work, because the equipotential curves obtained thus do not approximate the equipotential curves of the full potentials.

A.4 Homogeneous Potentials

Apart from a constant factor, potential (A.7) is a particular case of the class of homogeneous potentials defined by:

$$U_n(x,y) = Re\{z^n\}, \tag{A.10}$$

with $z = y + ix$; Re denotes the real part. In polar coordinates (ρ, ϕ) given by $\rho^2 = x^2 + y^2$ and $\phi = \arctan(y/x)$, U_n takes the form:

$$U_n(\rho, \phi) = \rho^n \cos(n\phi). \tag{A.11}$$

The origin $\rho = 0$ is a degenerate saddle, and has n distinct escapes for positive energies.

Eq. (A.10) or (A.11) defines a homogeneous potential of order n; (A.7) is given by $n = 3$. As explained in section 2, the box-counting dimension of systems described by homogeneous potentials is the same for all energies, and so d depends only on n. We have calculated d for some values of n; the result is plotted in fig. 8. The value of d calculated for $n = 3$ given in the previous section is compatible with the estimated value obtained in [3]. We see that d increases with n.

The potentials U_n have been studied analytically in [6, 7], where it is proved that the invariant set of these systems defines a symbolic dynamics, which shows rigorously that they have chaotic motion. These potentials have also been studied in the context of the motion of test particles in interaction with a plane fronted (pp) gravitational wave [2, 3].

A.5 Conclusions

We have studied numerically the structure of the basin boundaries of escape of the Hénon-Heiles and some related systems. We found that they have fractal structures, implying a great sensitivity to the initial conditions in the escape route followed by particles, measured by the box-counting dimension d. One common feature in the systems is that d tends to its maximum value (which is equal to the dimension of the ambient space) as the energy tends to the escape energy[2]. We conjecture that this is a general behavior, valid for all systems. The behavior for energies much greater than the escape energy is system-dependent. In the Hénon-Heiles system, $d-1$ tends asymptotically to a non-zero limiting value, while in the case of the two potentials of section 3, $d-1$ goes to zero as $E \to \infty$.

Acknowledgments

We would like to thank our referees, and especially referee no. 2, for pointing out some mistakes and providing some valuable suggestions and comments.

We want to thank FAPESP for financial support. Also, PSL thanks CNPq.

[2]for the class of homogeneous potentials given by (A.10), it is not possible to define an escape energy since the motion is unbounded for all values of E.

Bibliography

[1] G. Contopoulos, *Astron. Astrophys.* **231**, 41 (1990).
G. Contopoulos and D. Kaufmann, *Astron. Astrophys.* **253**, 379 (1992)
G. Contopoulos and C. Polymilis, *Phys. Rev. E* **46**, 1546 (1993)
G. Contopoulos, H. E. Kandrup and D. Kaufmann, *Physica D* **64**, 310 (1993)

[2] J. Podolský and K. Veselý, *Phys. Rev. D* **58**, 081501 (1998). (gr-qc 9805078)

[3] J. Podolský and K. Veselý, *Class. Quantum Grav.* **15**, 3505 (1998)

[4] E. Ott, *Chaos in Dynamical Systems*, Cambridge University Press, Cambridge (1993)

[5] M. Hénon and C. Heiles, *Astron. J.* **69**, 73 (1964)

[6] R. C. Churchill, G. Pecelli and D. L. Rod, *J. Diff. Equ.* **17**, 329 (1975)

[7] R. C. Churchill, D. L. Rod, *J. Diff. Equ.* **21**, 39 (1976); **21**, 66 (1976); **24**, 329 (1977)

[8] S. Bleher, C. Grebogi, E. Ott and R. Brown, *Phys. Rev. A* **38**, 930 (1988)

[9] I. M. Jánosi, T. Tél, D. E. Wolf and J. A. C. Gallas, *Phys. Rev. E* **56**, 2858 (1997)

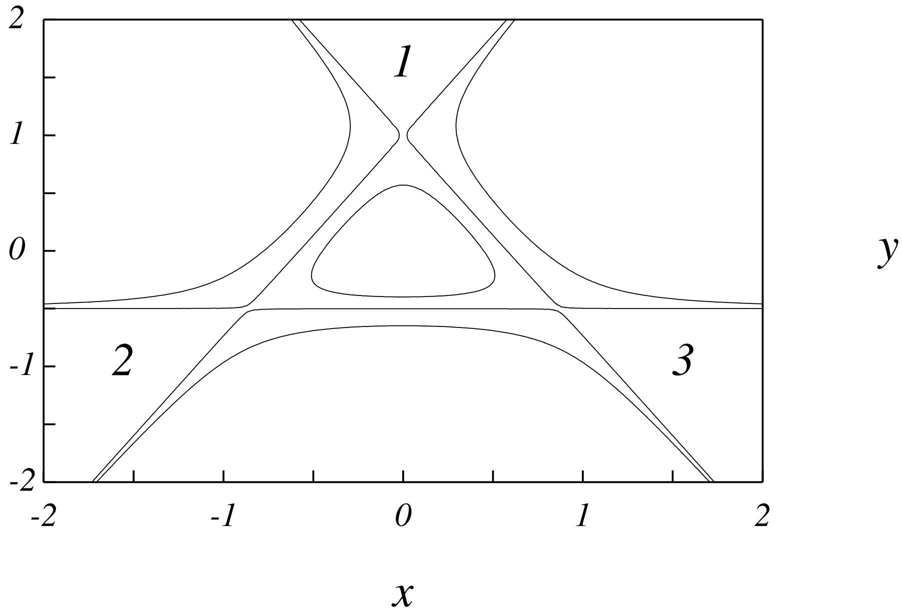

Figure A.1: Level contours of $V(x, y)$ for the Hénon-Heiles system.

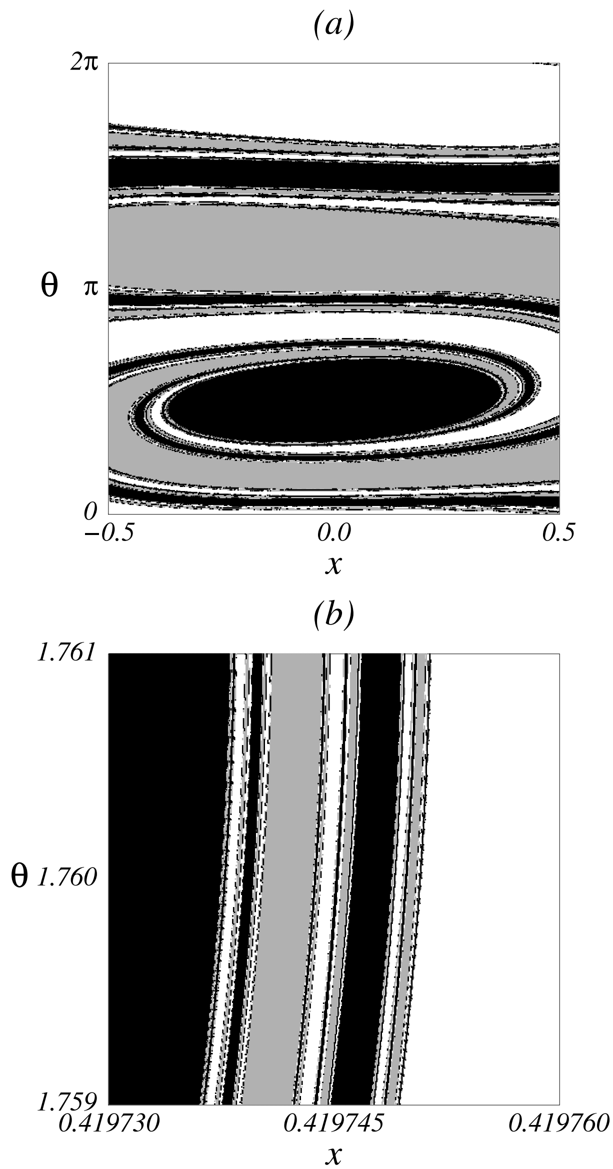

Figure A.2: Portrait of the basins of the HH system for $E = 0.3$. The initial conditions were chosen on a grid of 500×500. Regions in black correspond to orbits that escape to $y \to +\infty$; regions in gray correspond to orbits that escape for $x \to -\infty$, and regions in white correspond to orbits that escape for $x \to +\infty$. (b) is a detail of (a).

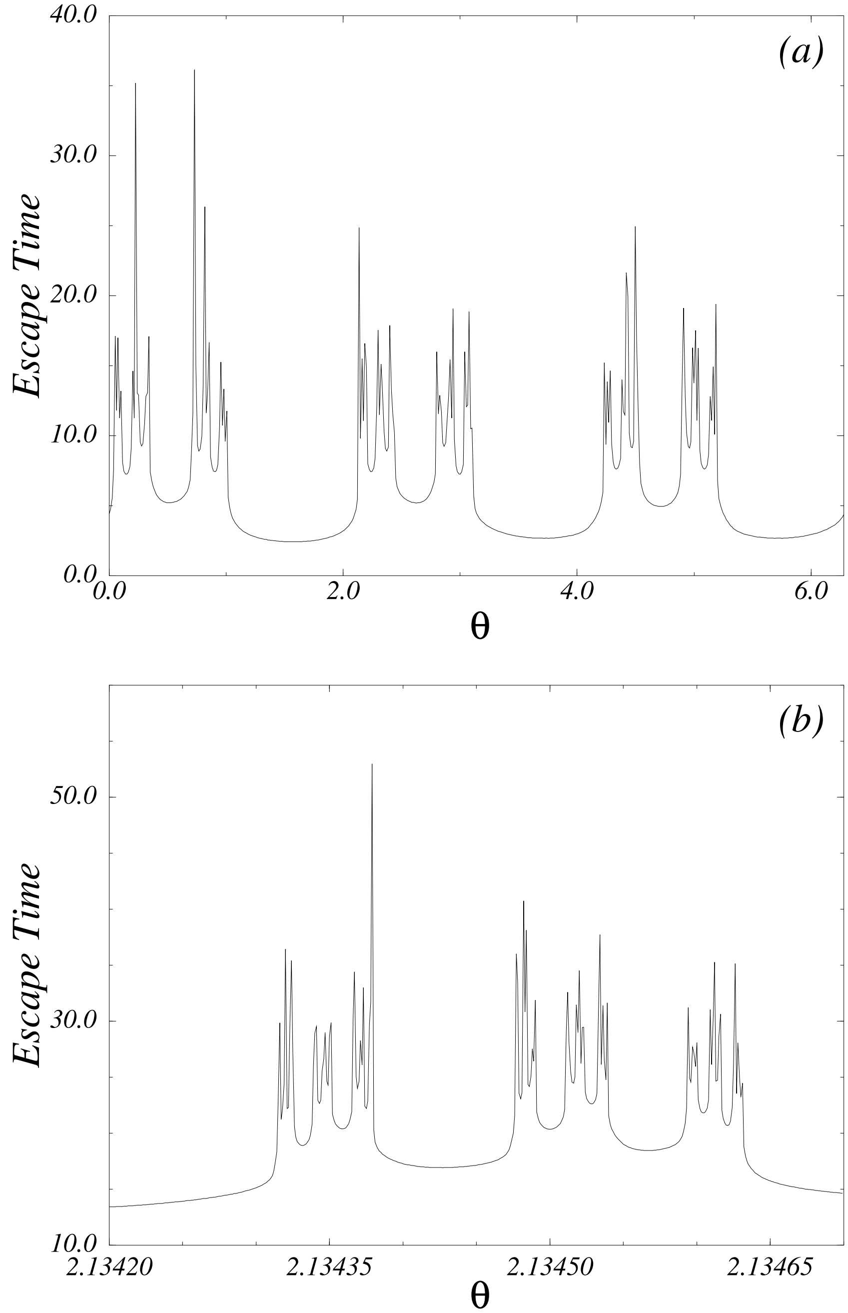

Figure A.3: Escape time in the Hénon-Heiles model versus the velocity angle θ, for $x_0 = y_0 = 0$ and $E = 0.3$. (b) is a detail of (a).

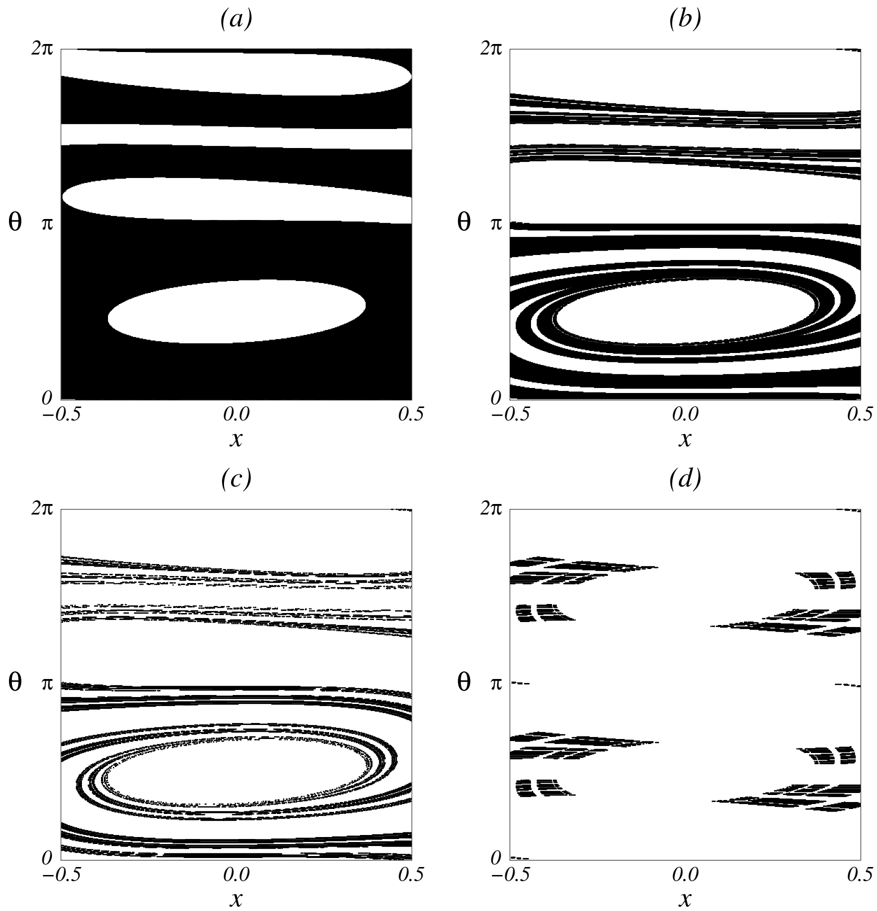

Figure A.4: Sets I_n and R_2 for the Hénon-Heiles potential with $E = 0.3$: (a) I_1, (b) I_2, (c) I_3, (d) R_2.

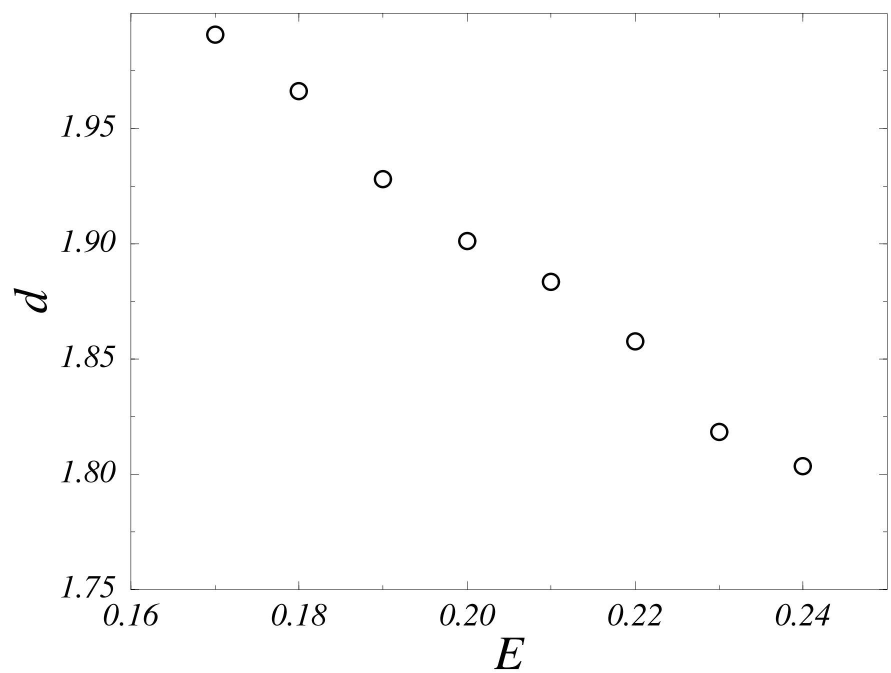

Figure A.5: Dimension d of the basin boundary for the Henón-Heiles model as a function of the energy, for E near E_c. The size of the circles correspond approximately to the statistical uncertainty of d.

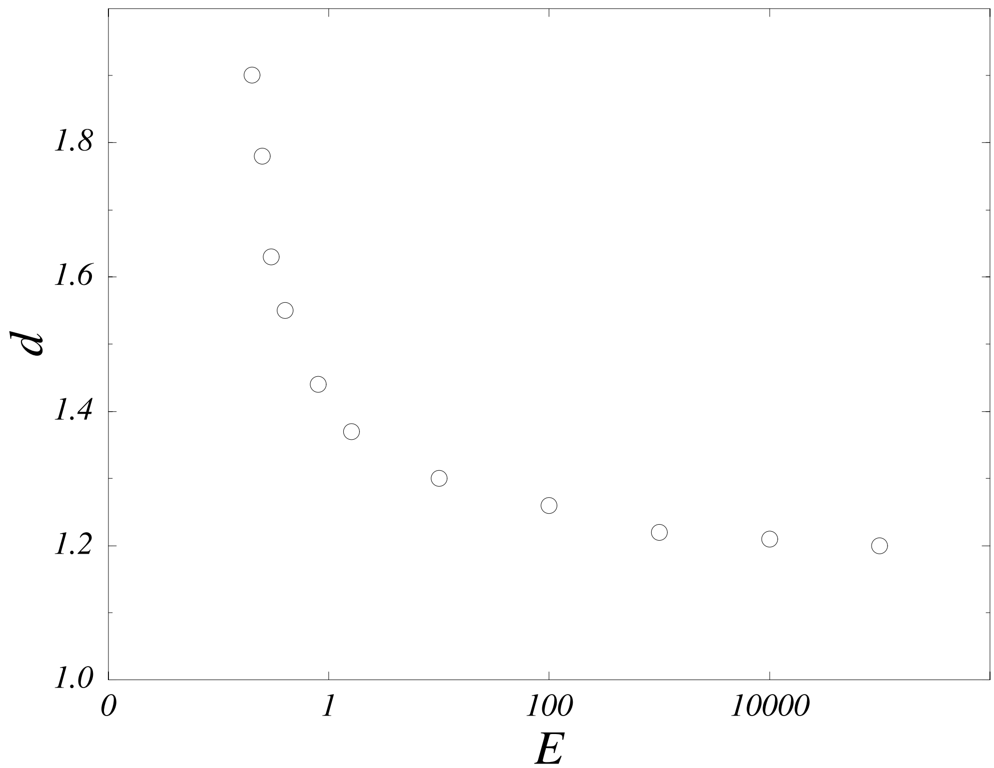

Figure A.6: Plot of the dimension d of the basin boundary for the HH model as a function of the energy, for large values of E. The size of the circles correspond approximately to the statistical uncertainty of d.

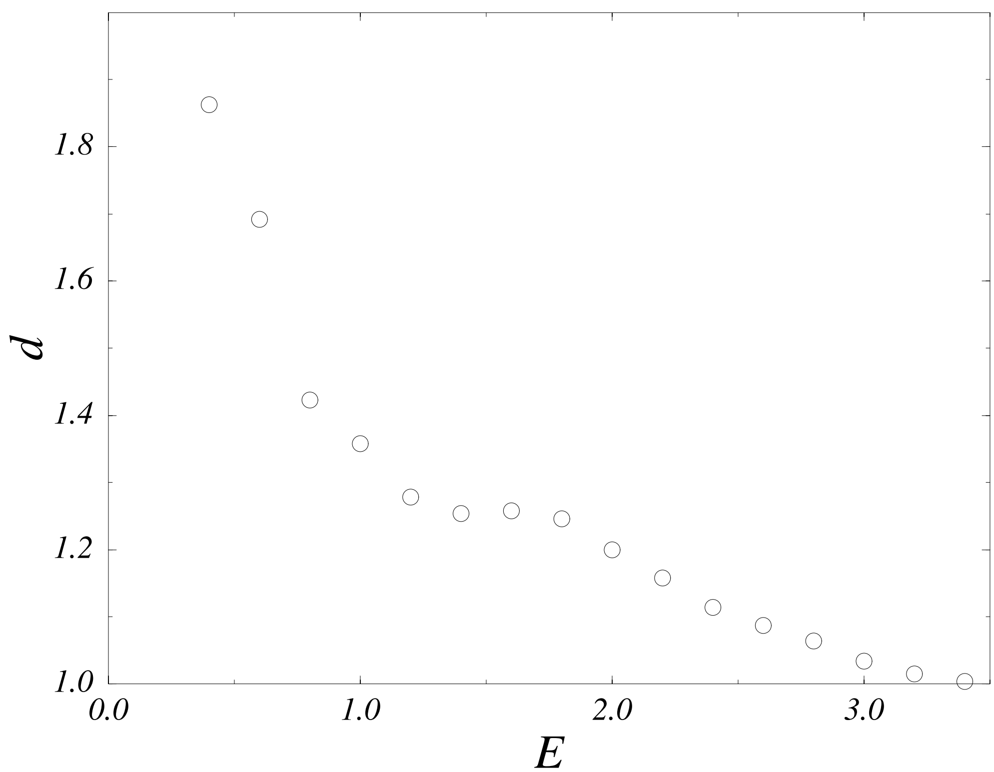

Figure A.7: Dimension d of the basin boundary for the V_1 potential (A.8) as a function of the energy. The size of the circles correspond approximately to the statistical uncertainty of d.

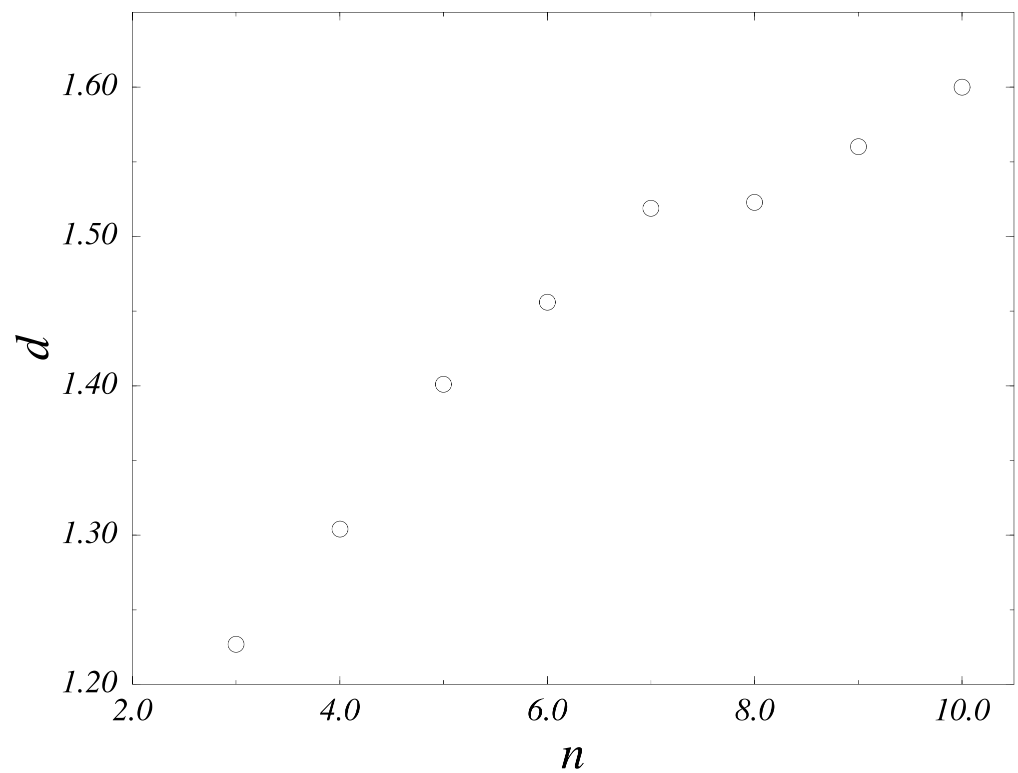

Figure A.8: Dimension d of the basin boundary for the U_n potentials (A.10) as a function of n. The size of the circles correspond approximately to the statistical uncertainty of d.

Apêndice B

“Fractal Escapes in Newtonian and Relativistic Multipole Gravitational Fields”

Reprodução do artigo “Fractal Escapes in Newtonian and Relativistic Multipole Gravitational Fields”, submetido à Physics Letters A.

Fractal Escapes in Newtonian and Relativistic Multipole Gravitational Fields

Alessandro P. S. de Moura
Instituto de Física Gleb Wataghin, UNICAMP, 13083-970
Campinas SP, Brazil

Patricio S. Letelier
Instituto de Matemática, Estatística e Ciência da Computação,
Departamento de Matemática Aplicada, UNICAMP,
13083-9790 Campinas SP, Brazil

Abstract

We study the planar motion of test particles in gravitational fields produced by an external material halo, of the type found in many astrophysical systems, such as elliptical galaxies and globular clusters. Both the Newtonian and the general-relativistic dynamics are examined, and in the relativistic case the dynamics of both massive and massless particles are investigated. The halo field is given in general by a multipole expansion; we restrict ourselves to multipole fields of pure order, whose Newtonian potentials are homogeneous polynomials in cartesian coordinates. A pure n-pole field has n different escapes, one of which is chosen by the particle according to its initial conditions. We find that the escape has a fractal dependency on the initial conditions for $n > 2$ both in the Newtonian and the relativistic cases for massive test particles, but with important differences between them. The relativistic motion of massless particles, however, was found to be regular for all the fields we could study. The box-counting dimension was used in each case to quantify the sensitivity to initial conditions which arises from the fractality of the escape route.

B.1 Introduction

It is common in astrophysics to find systems composed by an external material halo surrounding an inner region which is either void or has a massive black hole in the center. Examples of systems that are realistically described by such a model are elliptical galaxies and globular clusters[1]. The gravitational field in the inner region due to the halo satisfies the vacuum field equations, and in Newtonian gravitation it can be expanded in a sum of multipole terms of various orders. Due to the intrinsic nonlinearity of general relativity, in general this is not true for general relativistic fields. However, in many situations the halo can be supposed to be axisymmetric; in this case, the general solution of Einstein's equations is known, and the inner relativistic field can also be expanded in a series of multipolar terms. In this article, we study the dynamics of test particles in pure multipolar halo fields (without any matter in the inner region), both in the Newtonian and relativistic theories, for several multipole orders, for material particles and (in the relativistic cases) for light. We find that in each case the systems have distinct well-defined *escapes.* Different escapes are chosen by the test particles depending on its initial conditions; if the escape route is a fractal function of the initial conditions, the outcome of a particle starting from a given initial condition shows a sensitive dependence on these initial conditions. In this sense, we say that the system is chaotic[2, 3, 4]. Associated with this, we have a conveniently defined fractal dimension, which quantifies this sensitiveness. Fractal escapes have been found in a number of physical systems, including the Henon-Heiles system[5], astrophysical potentials[6], the motion of test particles in gravitational waves[7], classical ionization[8], motion of particles in a fluid[9], inflationary cosmology[10], and others. We study the fractal dimension for different multipole orders and for different energies, in the case of material test particles. For simplicity, we confine ourselves to the case of zero angular momentum, when the motion is planar.

This article is organized as follows: in section 2, we investigate the classical multipole gravitational field, showing the fractality of the escape basins and calculating the corresponding dimension for several multipole orders. In section 3, we turn to the relativistic case, and investigate the dynamics of both material particles and massless particles; we compare the results with those obtained in the classical case. In section 4, we summarize our results and draw some conclusions.

B.2 Newtonian multipole fields

The Newtonian gravitational field in the inner region due to the mass in the halo satisfies the vacuum (Laplace) field equation $\nabla^2\Psi = 0$, and therefore can be uniquely expanded in a sum of multipole terms. If the field is axisymmetric, as we admit from now on, its multipole expansion can be written as:

$$\Psi = \sum_{n=0}^{\infty} \left\{ a_n R^n + b_n R^{-(n+1)} \right\} P_n(\cos\theta),$$

where $R^2 = z^2 + r^2$, $\cos\theta = z/R$, and r and z are the usual cylindrical coordinates; the P_n are Legendre polynomials. If we consider the inner region to be empty of matter, Ψ cannot have singularities there. This means that $b_n = 0$ for all n in the inner region. Thus:

$$\Psi = a_0 + \sum_{n=1}^{\infty} a_n R^n P_n(\cos\theta), \tag{B.1}$$

where a_0 is a constant which can without lack of generality be chosen as zero.

The multipole expansion of Ψ contains only terms that become singular as $R \to \infty$ (with the exception of the constant term a_0). Here we are interested in studying the dynamics of the field due to each multipole term separately. We therefore define the n-th order multipole field Ψ_n as:

$$\Psi_n = a_n R^n P_n(\cos\theta). \tag{B.2}$$

We now consider a test particle moving in the field Ψ_n with no angular momentum in the direction of the symmetry axis z; in this case, the particle's motion is restricted to a plane that contains the z axis. A convenient set of coordinates in this plane is given by the z axis and the extended r axis, which reaches negative values. In order to avoid confusion, we shall denote the extended r axis by x, with $-\infty < x < +\infty$. Ψ is written in terms of x simply by replacing it for r. The Hamiltonian of a test particle of unit mass acted upon by the field Ψ_n is:

$$H_n = \frac{1}{2}\left(\dot{x}^2 + \dot{z}^2\right) + \Psi_n(x, z). \tag{B.3}$$

The corresponding equations of motion are $\ddot{x} = -\partial\Psi_n/\partial x$, $\ddot{z} = -\partial\Psi_n/\partial z$. Since Ψ_n is a homogeneous potential, satisfying $\Psi_n(\lambda x, \lambda z) = \lambda^n \Psi_n(x, z)$, these equations are invariant with respect to the similarity transformations $x \to \lambda x$, $z \to \lambda z$, $t \to t/\sqrt{\lambda}$, and $E \to \lambda^n E$, where λ is an arbitrary scale factor. Thus, to each orbit in the $\Psi_n(x, z)$ potential there corresponds a similar orbit in the transformed potential $\Psi_n(\lambda x, \lambda z)$, as long as λ is positive. This means that the dynamics for all positive values of E is the same except for scaling; we have to consider only one value of E for each multipole potential Ψ_n when we study its dynamical properties. We could use this scaling property of the Hamiltonian to make $a_n = 1$ in eq. (B.2), but we prefer to keep the constant arbitrary because of numerical convenience.

The region in the (x, z)-plane accessible by a particle moving in the potential Ψ_n with energy E is bounded by the equipotential curves $\Psi_n(x, z) = E$; the particle must satisfy $\Psi_n(x, z) \leq E$. This inequality can only be satisfied for a positive energy if Ψ_n is positive. From equation (B.2), it follows that the directions θ satisfying $P_n(\cos\theta) < 0$ are accessible for all positive energies, whereas directions satisfying $P_n(\cos\theta) > 0$, if followed far enough, reach values of R which violate the inequality $\Psi_n(x, z) \leq E$. Therefore, the directions with negative values of $P_n(\cos\theta)$ define distinct *escapes* of the potential Ψ_n; these escapes are separated by inaccessible regions lying at angles with $P_n(\cos\theta) > 0$. From the properties of Legendre polynomials, it follows that the potential Ψ_n has n distinct escapes.

As an example, Fig. 1 shows equipotential curves for some energies for the octopole field Ψ_3. The curves for different energies have the same shapes, which is a direct consequence of the potential's homogeneity. The three openings in the equipotential curves are seen clearly.

To give an idea of the kind of matter distribution that gives rise to fields of the form (B.1) and (B.2), consider two point masses (with mass m), located on the z axis at $z = +a$ and $z = -a$. On the (x, z)-plane, the potential generated by these two masses is given by $\Psi = -mG\left[\left((z-a)^2 + x^2\right)^{-1/2} + \left((z+a)^2 + x^2\right)^{-1/2}\right]$, where G is Newton's gravitational constant. At $x = 0$, $z = 0$, we have $\partial\Psi/\partial x = \partial\Psi/\partial z = 0$. Expanding Ψ in a Taylor series in the vicinity of this equilibrium point, we find that to second order in x and z, Ψ is given by:

$$\Psi = -\frac{2mG}{a^3}\left(2z^2 - x^2\right) = -\frac{4mG}{a^3} R^2 P_2(\cos\theta). \tag{B.4}$$

In the expression above we have discarded an unimportant additive constant. Thus, the field near the equilibrium point is approximately a quadrupole field Ψ_2, with $a_2 = -4mG/a^3$. This field has two escapes, directed towards the two point masses. As a more complicated example, consider a field generated by a point mass with mass M on the z axis at $z = h$ and a ring of uniform linear density and total mass m centered on the z axis at $z = b$ with radius a. A calculation similar to the one presented above shows that if the parameters of the system are chosen so as to satisfy the relations:

$$M = -4mb^3 \frac{\left(a^2+b^2\right)^{1/2}}{\left(2b^2-a^2\right)^2},$$

$$h = \frac{2b\left(a^2+b^2\right)}{2b^2-a^2},$$

with $b < 0$, $h > 0$ and $2b^2 < a^2$, then both the dipole and the quadrupole terms vanish at $(x, z) = (0, 0)$, and the field is described to a first approximation by an octopole field Ψ_3 with a coefficient a_3 given by:

$$a_3 = -\frac{m}{2}\left(a^2+b^2\right)^{-7/2}\left(2a^2b + \frac{a^4}{2b}\right).$$

This field has three escapes (see Fig. 1), directed towards the point mass and the two intersections of the (x, z)-plane with the massive ring.

To each escape we define the corresponding *basin*, which is the set of initial conditions in the phase space that lead to that escape. If the escape chosen by a particle is a fractal function of its initial condition, then the basins of the various escapes are mixed in a complex fashion, down to arbitrarily small scales, and the final state of the particle (i.e. which escape it chooses) can be extremely sensitive to its initial state. This happens when the basin boundary is fractal. We then say that the system presents chaos. This is the appropriate definition of chaos to open systems, whose motions are not confined to a limited volume of the phase space, and this is the definition used throughout this article.

The directions θ_e which are minima of $P_n(\cos\theta)$ correspond to valleys in the potential Ψ_n; the escape regions are centered around these directions. The walls on either side of these valleys became increasingly steeper as we go to $R \to \infty$. This makes the orbits of escaping particles become focused in beams around these directions as they move towards $R \to \infty$. This phenomenon can be seen in fig. 2a, which shows some numerically integrated orbits all beginning with initial conditions on $x = z = 0$, and varying initial velocity direction angle ϕ, defined by:

$$v_x = v\sin\phi; \quad v_z = v\cos\phi,$$

where v_x and v_z are the initial velocities in the x and z directions, and the velocity modulus v is fixed by the conservation of energy:

$$v = \sqrt{2E},$$

since $\Psi_n(0,0) = 0$.

The fractal nature of the basin boundary can be observed in a plot of the escape angle θ_e as a function on the initial velocity direction angle. This is shown in Fig. 3a. We had to choose a "cutoff distance" R_0 such that the integration stops when R reaches R_0. In the case of Fig.3, we chose $R_0 = 10.0$. The discreteness of the values assumed by the escape angle is clearly seen in Fig. 3; this is an illustration of the focusing effect. The magnification of a tiny region of fig. 3a shown in fig. 3b gives us a convincing proof that the basin boundary is fractal. An example of the sensitivity to initial conditions implied by the fractality of the basin boundary is given in fig. 2b, where three orbits with ϕ differing by less that one thousandth of a radian choose different escapes. We see that initially the orbits are indistinguishable, and after a time they separate rather abruptly and go to their distinct escapes. Figures 2 and 3 were plotted with $E = 1$ and $a_3 = 1$, but as we explained above, the result is exactly the same regardless of the parameters' values. We note that we have found no bounded orbits for any of the Ψ_n potentials, which might have been expected from the shapes of the equipotentials.

The reason why the escape basins are fractally mixed is that the particle can bounce many times off the potential "walls" before escaping. This means that associated with the fractality in the basin boundary we have also fractality in the escape time. To see that this is so, we plot the time it takes for a particle to escape (without discriminating among the various escapes) as a function of its initial velocity angle ϕ, for a fixed initial position x_0, z_0. Figure 4 shows the results for the octopole potential, with $x_0 = z_0 = 0$. The magnification shown in fig. 4b shows clearly the fractal nature of the escape time. Notice that fractal and non-fractal areas are mixed for all scales. The fractal nature of the escape time is a result of the existence of a fractal set of singularities in the escape time function, where the escape time diverges. This set of singularities results from the intersection between the set of initial conditions (a topological circle in this case) and the set in the phase space composed of orbits that never escape for $t \to \infty$, which in its turn is the stable manifold of the so-called *invariant set*, which is also fractal in our case and is composed of orbits that never escape for both $t \to \infty$ and $t \to -\infty$.

The sensitivity to initial conditions implied by the fractal nature of the basin boundary is made precise with the introduction of the *box-counting dimension* d, calculated in the following way. For a given initial position (which is $x_0 = y_0 = 0$ in our case), we pick a large number of random initial velocity angles ϕ, with $0 < \phi < 2\pi$. For each of these we integrate the equations of motion and see to which basin it belongs. We then take two neighboring angles $\phi - \epsilon$ and $\phi + \epsilon$ (with the same initial position), with ϵ being a small number, and find to which basin they belong. If all these three initial conditions do not belong to the same basin (if they lead to different escapes), then ϕ is said to be an "uncertain" angle. The number n of uncertain angles found in a sample of N randomly chosen points is a function of the displacement ϵ, and for large N the fraction n/N of uncertain points scales as

$$\frac{n}{N} \equiv f \propto \epsilon^{1-d}, \tag{B.5}$$

where d is by definition the box-counting dimension of the intersection of the basin boundary with the one-dimensional manifold in which we chose the initial conditions. We numerically calculate f for several values of ϵ, and d is directly obtained from the plot of $\ln f$ versus $\ln \epsilon$, which should be a straight line, and whose inclination α is related to d by $\alpha = 1 - d$.

We have calculated in this way the box-counting dimension for multipole fields with orders from 2 to 9. Since the dynamics is the same for every value of the energy, d does not depend on E, and is unique for each multipole order. Figure 5 shows the plot of $\ln f$ versus $\ln \epsilon$ we have obtained for the octopole field ($n = 3$). The data fit quite well into a straight line, whose inclination ($\alpha = 0.77 \pm 0.01$) gives a dimension $d = 0.23 \pm 0.01$, confirming the fractal nature of the basin boundary. Figure 6 shows d as a function of the multipole order n. We see that d increases monotonically with n, which means that the fractality of the basin boundary increases with n, and thus the dynamics becomes "more chaotic" with multipolar fields of higher orders. The dipole and quadrupole fields ($n = 1$ and $n = 2$, respectively) have regular basin boundaries, and show no chaos in their dynamics. In fact, the potentials Ψ_1 and Ψ_2 are separated using the x, z coordinates, as can be immediately seen from (B.2), which implies that the Hamiltonian is integrable and the basin boundaries are regular.

A field of the general form (B.1), with the contribution of more than one multipole order, is not homogeneous, and its dynamics changes with the energy. We have studied how the box-counting dimension changes with E for the field $\Psi = \Psi_3 + \Psi_4$, with equal contributions of the 3rd and 4th multipole orders. For high values of E, the particle's motion is dominated by the 16-pole component of the field, and the equipotentials are practically the same as the pure 16-pole field. Accordingly, for these energies the box-counting dimension was found to be numerically indistinguishable from the value we obtained for the pure 16-pole field Ψ_4. As the energy is lowered, however, d does *not* go to its pure octopole field value, as might be imagined. In fact, for $E = 0.1$, we found $d = 0.38 \pm 0.01$; this value of d is higher then that of both the pure octopole field and the quadrupole field. Thus, the fractal dimension from a field made by the mixture of two multipole orders is not necessarily an intermediate value between the dimensions of each pure multipole order separately.

B.3 Relativistic multipole fields

In this section we investigate the dynamics with a general-relativistic generalization of the Newtonian multipole fields we studied in the previous section. In general relativity, the dynamics results from the space-time metric $ds^2 = g_{\mu\nu}dx^\mu dx^\nu$, where $g_{\mu\nu}$ is the metric tensor and x^μ are the space-time coordinates. The equations of motion for a test particle in the field $g_{\mu\nu}$ are given by the geodesic equation $\ddot{x}^\mu = -\Gamma^\mu_{\alpha\beta}\dot{x}^\alpha\dot{x}^\beta$, where $\Gamma^\mu_{\alpha\beta}$ is the Christoffel symbol, and $\dot{x}^\mu = dx^\mu/d\lambda$, with λ being a convenient affine parameter.

For an axially symmetric and static field, the metric is most conveniently written in the Weyl form[11]:

$$ds^2 = e^{2\Psi}dt^2 - e^{-2\Psi}\left[e^{2\gamma}\left(dr^2 + dz^2\right) + r^2 d\phi^2\right], \tag{B.6}$$

where r, z and ϕ are cylindrical-like coordinates, and t is the time. We use units such that $c = 1$ throughout. The metric functions Ψ and γ depend on r and z only, and satisfy the vacuum Einstein field equations:

$$\nabla^2\Psi \equiv \frac{\partial^2\Psi}{\partial r^2} + \frac{1}{r}\frac{\partial\Psi}{\partial r} + \frac{\partial^2\Psi}{\partial z^2} = 0; \tag{B.7}$$

$$d\gamma = r\left[\left(\frac{\partial\Psi}{\partial r}\right)^2 - \left(\frac{\partial\Psi}{\partial z}\right)^2\right]dr + 2r\frac{\partial\Psi}{\partial r}\frac{\partial\Psi}{\partial z}dz. \tag{B.8}$$

Eq. (B.7) is just Laplace's equation in cylindrical coordinates, and eq. (B.8) is a quadrature whose integrability is automatically guaranteed by eq. (B.7). Thus, each axisymmetric solution of Newton's field equation corresponds to a general-relativistic metric (B.6), with γ being found by integration of eq. (B.8) with the requirement that the metric be regular in the symmetry axis. Based on this, we define the relativistic analogue to the multipolar fields Ψ_n

in eq. (B.2) to be the metric (B.6) with $\Psi = \Psi_n$ and $\gamma = \gamma_n$ obtained through eq. (B.8). The integration can be performed analytically, and the result is:

$$\gamma_n = \frac{n}{2} a^2 R^{2n} \left[P_n^2(\cos\theta) - P_{n-1}^2(\cos\theta) \right], \tag{B.9}$$

with $R^2 = r^2 + z^2$. Since there are many possible relativistic space-times which in the weak field limit correspond to a given Newtonian field, the choice of the metric is not unique. We have chosen the metric defined by Ψ_n and γ_n because it is the simplest choice, and because the field obtained in this way shares important features with the Newtonian field, as we shall see shortly.

As in the Newtonian case, the invariance of the system with respect to time translations and axial rotations implies the existence of two constants of motion, which can be identified as the energy E and the z-component of the angular momentum L_z. They can be found by using the Lagrangian associated with the metric (B.6):

$$2L = e^{2\Psi} \dot{t}^2 - e^{-2\Psi} \left[e^{2\gamma} \left(\dot{r}^2 + \dot{z}^2 \right) + r^2 \dot{\phi}^2 \right], \tag{B.10}$$

where the dot denotes differentiation with respect to the affine parameter. Since both Ψ and γ depend only on r and z, the Lagrangian L does not depend on t and ϕ; they are “cyclical coordinates” in the language of Hamiltonian dynamics, and they are associated with the conserved quantities:

$$E = \frac{\partial L}{\partial \dot{t}} = e^{2\Psi} \dot{t}; \tag{B.11}$$

$$L_z = \frac{\partial L}{\partial \dot{\phi}} = -r^2 e^{-2\Psi} \dot{\phi}. \tag{B.12}$$

Since the Lagrangian function (B.10) has only kinetic terms, and since L does not depend explicitly on the affine parameter, the Hamiltonian of this system is simply L itself, and its conservation gives us yet another constant of motion:

$$L = \frac{1}{2} m_0^2,$$

where m_0 is the test particle's rest mass. In the case of light, we have $m_0 = 0$; for massive particles, we can without loss of generality make $m_0 = 1$. Rewriting L with the help of eqs. (B.11) and (B.12), we have:

$$E^2 e^{-2\Psi} - L_z^2 r^{-2} e^{2\Psi} - e^{2(\gamma - \Psi)} \left(\dot{r}^2 + \dot{z}^2 \right) = \delta, \tag{B.13}$$

with $\delta = 0$ for particles with zero rest mass, and $\delta = 1$ for massive particles. As in the Newtonian case in the previous section, we will restrict ourselves to motion with zero angular momentum ($L_z = 0$), when the motion is planar. In complete analogy to what we did for the Newtonian potential, we define a new coordinate x, which is no more than r extended to negative values; the motion of our zero angular momentum test particle occurs on the (x, z)-plane. All the expressions above are written in terms of x simply by replacing r by x everywhere.

The accessible region of the (x, z)-plane is found by setting $\dot{x} = \dot{z} = 0$ in (B.13); taking into account that $L_z = 0$, we have:

$$E^2(\dot{x} = \dot{z} = 0) \equiv U(x, z) = \delta e^{2\Psi}. \tag{B.14}$$

The accessible region for a particle with energy E is given by $U(x, z) \leq E^2$. For massless particles ($\delta = 0$), $U = 0$, and this condition is always satisfied; thus, the whole (x, z)-plane is accessible to null geodesics. This is not so for massive particles ($\delta = 1$); the regions they are able to reach on the xz plane depend on their energy and are determined by Ψ.

We now consider the pure multipole potentials $\Psi_n = a_n R^n P_n(\cos\theta)$, with γ_n given by (B.9). We first treat the case of massive particles; the motion of light will be studied later. The effective potential is $U = e^{2\Psi} = g_{tt}$, where g_{tt} is the time-time component of the metric. It is clear that the dynamics in the relativistic field (Ψ_n, γ_n) is more complex than its Newtonian counterpart. In particular, since neither the effective potential (B.14) nor γ_n are homogeneous functions, and furthermore the relativistic equations of motion depend on the velocities $\dot{x}^\mu$, the orbits in the relativistic field do not satisfy the homogeneity property that guarantees for the orbits in the Newtonian field that the dynamics is the same for all energies, up to a global scaling. We thus expect the dynamics to change with the energy in the relativistic case; this is a fundamental difference between the two theories. In spite of this, we see from eq. (B.14) that the curves of constant effective potential are still given by $\Psi_n = const$ (although the constant is no longer just the energy). This means that the escapes in the potentials Ψ_n are the same as those in the Newtonian fields. As $R \to \infty$ along the asymptotically allowed directions, given by $P_n(\cos\theta) < 0$ (exactly as in the Newtonian case), we have $U = g_{tt} \to 0$, that is, we have an infinite red shift (as in section 2, we assume $a_n > 0$): particles are attracted to these regions. On the other hand, for asymptotically forbidden regions, with $P_n(\cos\theta) < 0$, we have $g_{tt} \to \infty$, an infinite blue shift: particles are attracted *away* from these regions.

We now study the dynamics in this field using the same techniques we used in the Newtonian case. We integrate numerically orbits with initial position $x_0 = z_0 = 0$ and variable velocity angle ϕ, with the magnitude v of the velocity being fixed by the conservation of energy. Since $\Psi_n(0,0) = \gamma_n(0,0) = 0$ for all n, from eq. (B.13) we see that:

$$\dot{x}_0 = v \sin\phi \quad \dot{z}_0 = v \cos\phi,$$

with

$$v^2 = E^2 - 1.$$

The equations of motion for the independent variables x and z are obtained directly from the geodesic equations:

$$\ddot{x} = -\frac{1}{2f}\left[g^{tt}_{,x}E^2 + f_{,x}\left(\dot{x}^2 - \dot{z}^2\right) + 2f_{,z}\dot{x}\dot{z}\right]; \tag{B.15}$$

$$\ddot{z} = -\frac{1}{2f}\left[g^{tt}_{,z}E^2 + f_{,z}\left(\dot{z}^2 - \dot{x}^2\right) + 2f_{,x}\dot{x}\dot{z}\right], \tag{B.16}$$

with $f = e^{2(\Psi-\gamma)}$ and $g^{tt} = e^{-2\Psi}$; these equations are valid for $L_z = 0$. Together with the quadrature (B.11), the above equations give the complete dynamics of the system.

Similar to what we found in the previous section, the orbits are focused along directions corresponding to the minima of $P_n(\cos\theta)$. Plots of the escape angle for $n > 2$ are very similar to Fig. 3, showing clearly that the escape has a fractal dependency on the initial conditions. As in the Newtonian case, the dipole and quadrupole fields ($n = 1$ and 2, respectively) show a regular basin boundary. However, the equations of motion are not separated in x, z coordinates, as is the case for the Newtonian fields.

As we explained above, we expect the fractal basin boundary present in the $n > 2$ fields to change with the energy in the relativistic case, as opposed to the Newtonian one. As in the Newtonian case, we have found no stable bounded orbits, neither for massive particles nor for massless ones.

We calculate the fractal dimension of this set in the same way we did previously for the motion in the Newtonian field. In that case the dimension did not depend on the energy, because the dynamics is the same for all (positive) energies. This is not true for the relativistic dynamics, and we expect the dimension to change with the energy. This is indeed what we have found. As an example, we take the field (Ψ_4, γ_4). We consider particles with energies higher than 1, corresponding to positive energies in the Newtonian case. For E close to 1 (corresponding to energies close to 0 in the Newtonian field), we find that the box-counting dimension is equal to its Newtonian value. For instance, for $E = 1.01$, we find $d = 0.33 \pm 0.02$, which is (within the error) the same value we found for the Newtonian field Ψ_4. For higher energies, however, d changes with E: for $E = 1.5$, we have $d = 0.30 \pm 0.02$, and for $E = 2.0$, $d = 0.26 \pm 0.02$. We have calculated d for more values of E than we show here, and it seems that d decreases monotonically with E, and the system becomes more chaotic for large energies; this is the contrary to what is usually the case in bounded dynamics, where commonly the chaos grows with the energy. The same behavior is observed in the octopole field ($n = 3$), but in this case the variations in the dimension are smaller. Because of the complexity of the equations of motion for high multipole orders, we have not been able to calculate d with enough accuracy for n larger than 4, but we think this behavior of d might be a general feature of the dynamics for the Ψ_n fields.

In the case of null geodesics, the equations of motion are again given by eqs. (B.15) and (B.16), but the initial conditions are required to satisfy the constraint (B.13) with $\delta = 0$ (and $L_z = 0$ in our case). This allows us to scale the affine parameter so as to eliminate E from the equations. This means that the planar motion of light depends only on the chosen field Ψ_n, and not on any other parameter, unlike the motion of massive particles.

Even though the whole (x, z)-plane is accessible to massless particles, as we have seen, null geodesics also show focusing effects similar to that shown by massive particles. An example is given in Fig. 7, where the escape angle is plotted as a function of the initial velocity angle for null geodesics, for the octopole field $n = 3$. We see clearly that the values assumed by the escape angle are indeed discrete. We do not see, however, any region where the escape angle shows rapid variations, that is typical of fractal functions. Magnifications of several regions of Fig. 7 show no small-scale structures, indicating that the escape angle is not fractal. This is confirmed by direct calculation of the box-counting dimension, which gives $d = 1$ to within statistical accuracy. This result also holds for $n = 4$ and $n = 5$, which is the highest multipole order for which we have been able to obtain reliable results. We speculate that this result might be true for all n.

B.4 Conclusions

We have studied the dynamics of test particles in pure multipole fields generated by external halos of matter, when the particles have zero angular momentum and the motion happens on a plane. Such a system could be used to approximate observed astronomical fields, such as the interior of galaxies. We have considered both the Newtonian and the general-relativistic fields, and we have compared the results of the two theories.

For the Newtonian fields, the homogeneity of the pure potentials Ψ_n implies that the dynamics is independent on the energy. We have found that the escape chosen by the test particles is a fractal function of the initial conditions for all pure multipole fields of order higher than 3. For $n = 1, 2$, the Hamiltonian is separable and the basin boundaries are regular. We have calculated numerically the box-counting dimension d associated with the escape function. Since the dynamics is the same for all energies, d depends only on the multipole order n. We have found that d is an increasing function of n for n up to 9; higher values of n could not be studied because of numerical limitations. The increasing in the intensity of chaos with n can be understood by the fact that fields of higher order have a higher number of escapes. We have also studied the dynamics of a field made by the superposition of two different multipole orders, specifically, the field $\Psi = \Psi_3 + \Psi_4$. For this field, the dynamics depends on the energy, and we found that, although for high energies the box-counting dimension tends to the value of the Ψ_4 field, for low energies d assumes values higher than the dimensions of both Ψ_3 and Ψ_4, maybe somewhat surprisingly.

We now discuss the results found for the relativistic fields, starting by the dynamics of massive particles. The relativistic pure multipole fields have not the homogeneous property shown by their Newtonian counterparts, and their dynamics does depend on the energy, and so does the escape function. We found that the escape chosen by the particle is a fractal function of the initial conditions for fields of order higher than 2 also in the relativistic case. The dipole and quadrupole fields have regular basin boundaries, but unlike the Newtonian fields, the relativistic equations of motion are not directly separable. For $n > 2$, we expect the box-counting dimension d to change with the energy. We have calculated d as a function of the energy, and we have found that for low energies, d goes to the Newtonian values, as might have been expected. As E increases, d was found to decrease monotonically, for all the energies for which we have been able to obtain reliable results. We have obtained these results for $n = 3, 4$ and 5, and this seems to be a general feature of the dynamics of these fields.

For massless test particles, the escape function was found to be regular (non-fractal) for n up to 5; at least as far as the fifth multipole order, null geodesics are not chaotic.

Acknowledgments

We would like to thank FAPESP and CNPq for their financial support.

Bibliography

[1] J. Binney and S. Tremaine, *Galactic Dynamics*, Princeton University Press, Princeton, New Jersey (1994)

[2] C. Grebogi, S. W. McDonald, E. Ott and J. A. Yorke, Phys. Lett. **99A**, 415 (1983)

[3] S. Bleher, C. Grebogi, E. Ott and R. Brown, Phys. Rev. A **38**, 930 (1988)

[4] E. Ott, *Chaos in Dynamical Systems*, Cambridge University Press, Cambridge (1993)

[5] A. P. S. de Moura and P. Letelier, Phys. Lett. A **256**, 362 (1999)

[6] G. Contopoulos, D. Kaufmann, *Astron. Astrophys.* **253**, 379 (1992); G. Contopoulos, C. Polymilis, *Phys. Rev. E* **46**, 1546 (1993); G. Contopoulos, H. E. Kandrup, D. Kaufmann, *Physica D* **64**, 310 (1993)

[7] J. Podolsky and K. Vesely, Phys. Rev. D **58**, 081501 (1998)

[8] F. Sattin and L. Salasnich, Phys. Rev. E **59**, 1246 (1999)

[9] I. M. Jánosi, T. Tél, D. E. Wolf and J. A. C. Gallas, Phys. Rev. E **56**, 2858 (1997)

[10] N. J. Cornish and J. J. Levin, Phys. Rev. D **53**, 3022 (1996)

[11] D. Kramer, H. Stephani, M. A. H. MacCallum and E. Herlt, *Exact Solutions of Einstein's Field Equations*, Cambridge University Press, Cambridge (1980)

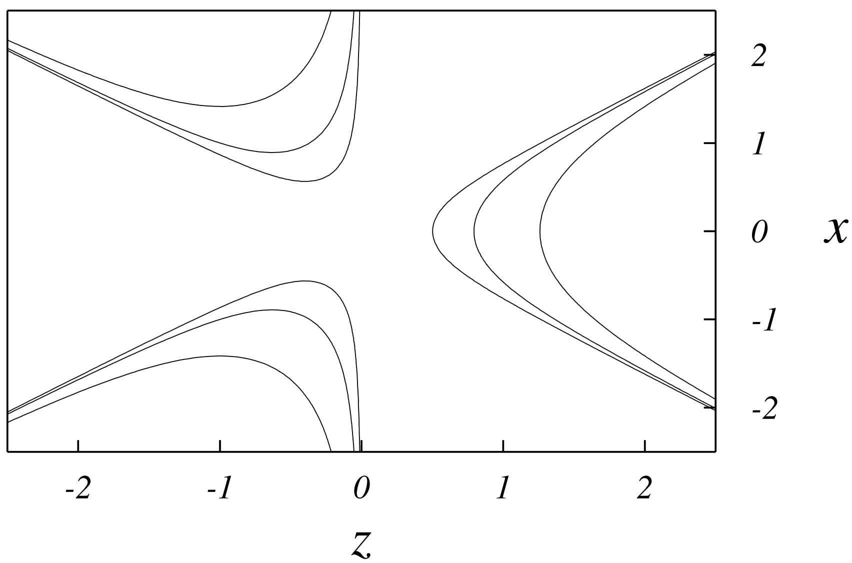

Figure B.1: Equipotential curves for the Newtonian octopole field Ψ_3. From the inside out, the energies are $E = 0.25$, $E = 1.0$ and $E = 4.0$.

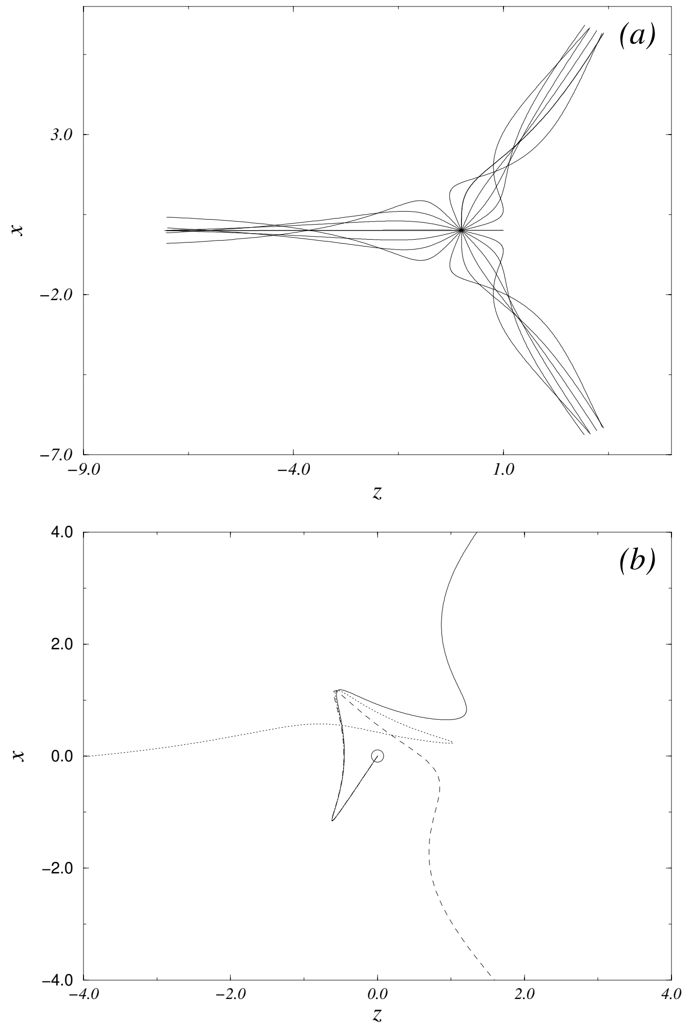

Figure B.2: Orbits in the Newtonian field Ψ_3 all starting from $x = z = 0$, with different initial directions and $E = 1.0$, $a_3 = 1$. Fig. 2b shows three orbits with initial velocity angles differing by 1/5000 radian; the circle marks the starting point $x = z = 0$.

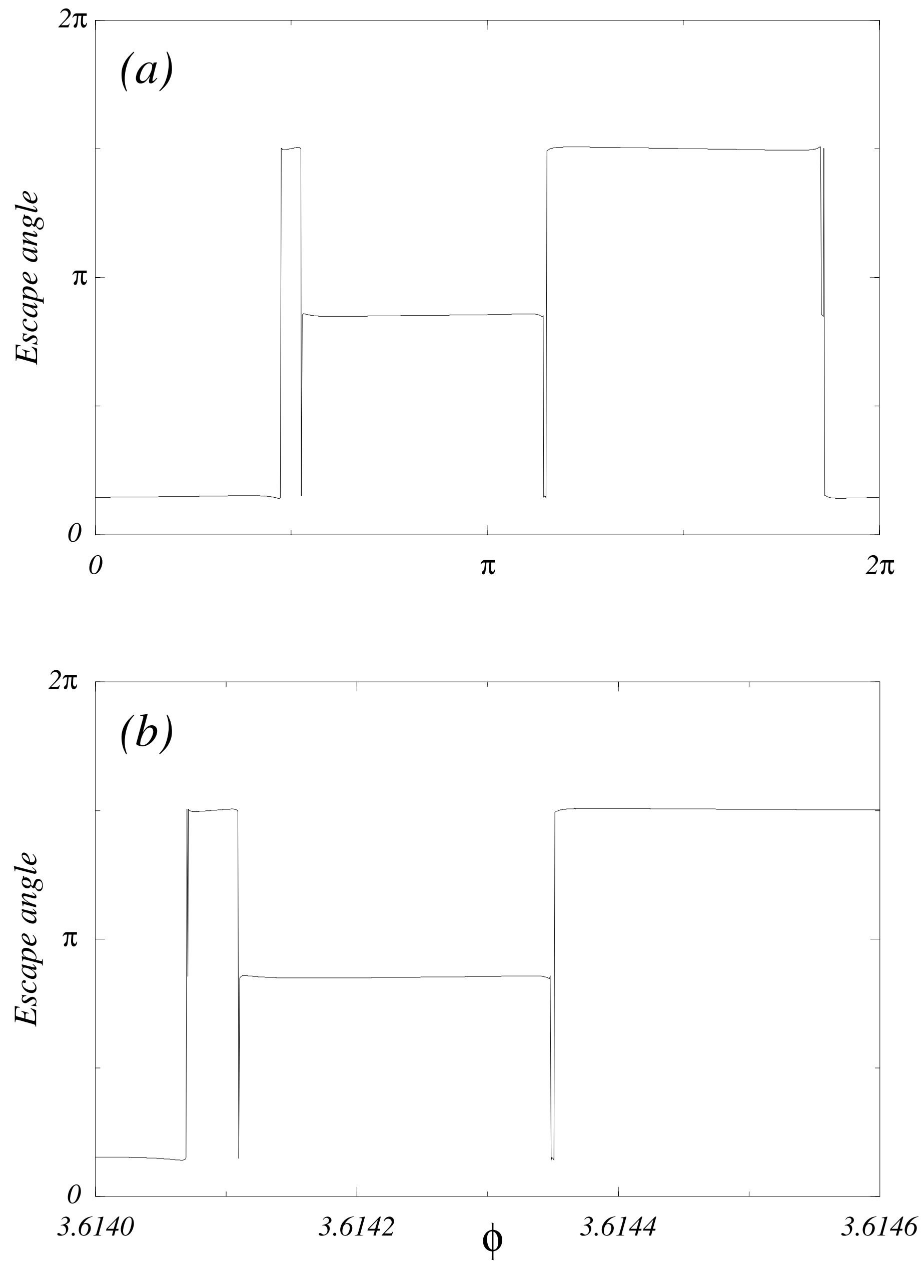

Figure B.3: Escape angle θ_e as a function of the initial velocity angle ϕ for the octopole field. Fig. 3b is a magnification of a small region of Fig. 3a.

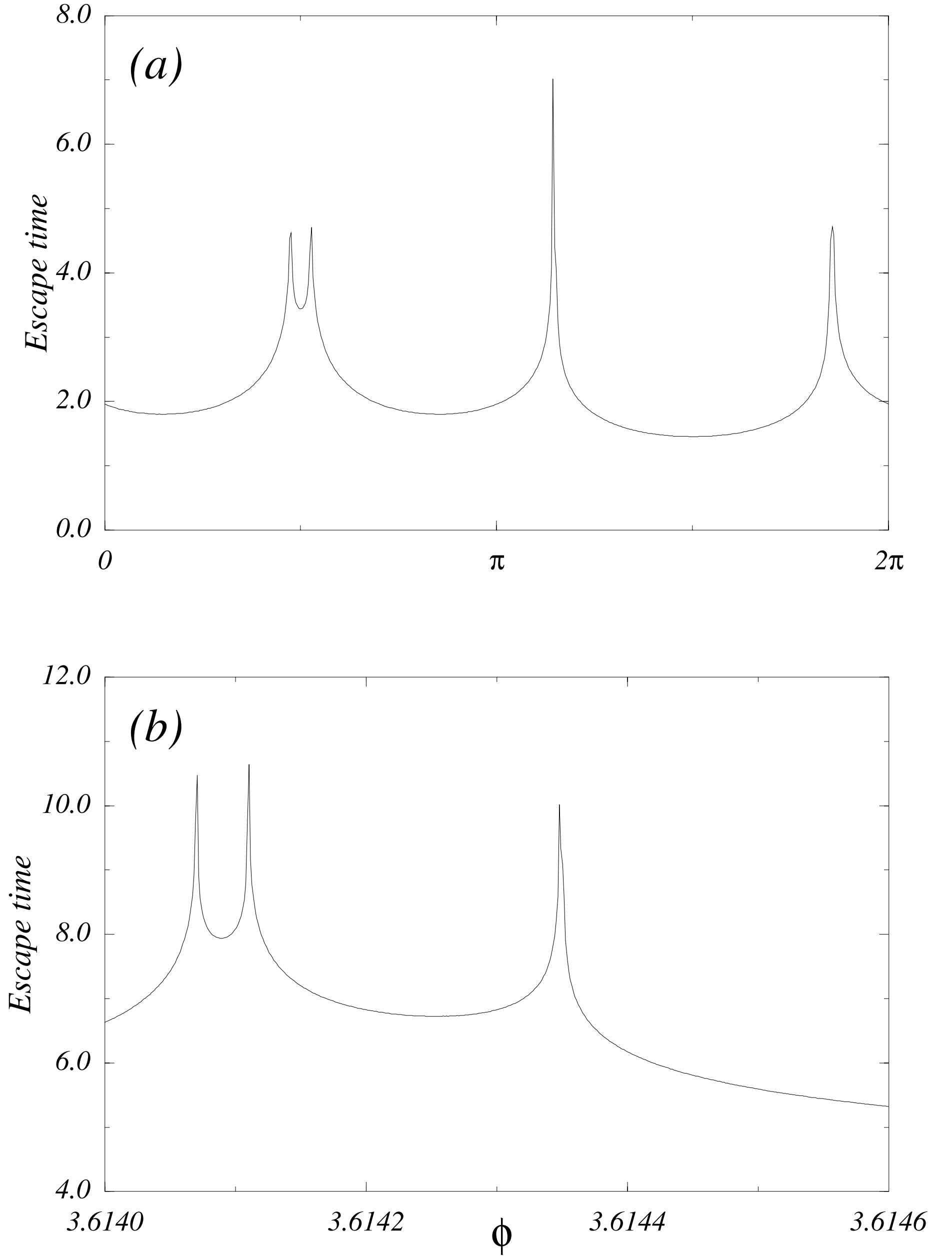

Figure B.4: Escape time as a function of the initial velocity angle ϕ for the octopole field. Fig. 4b is a magnification of a small region of Fig. 4a.

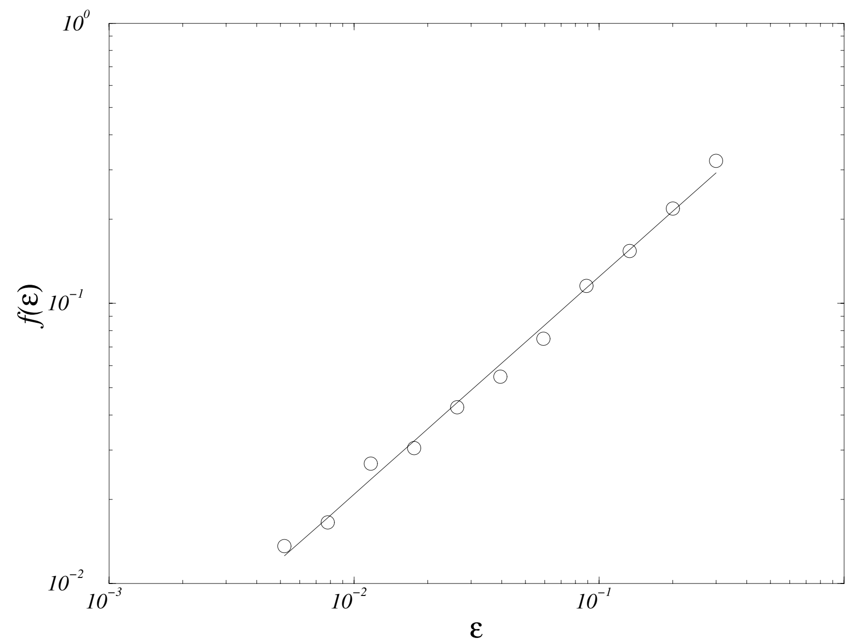

Figure B.5: $\ln f$ vs. $\ln \epsilon$ for the Newtonian octopole field. The straight line is the result of the fitting.

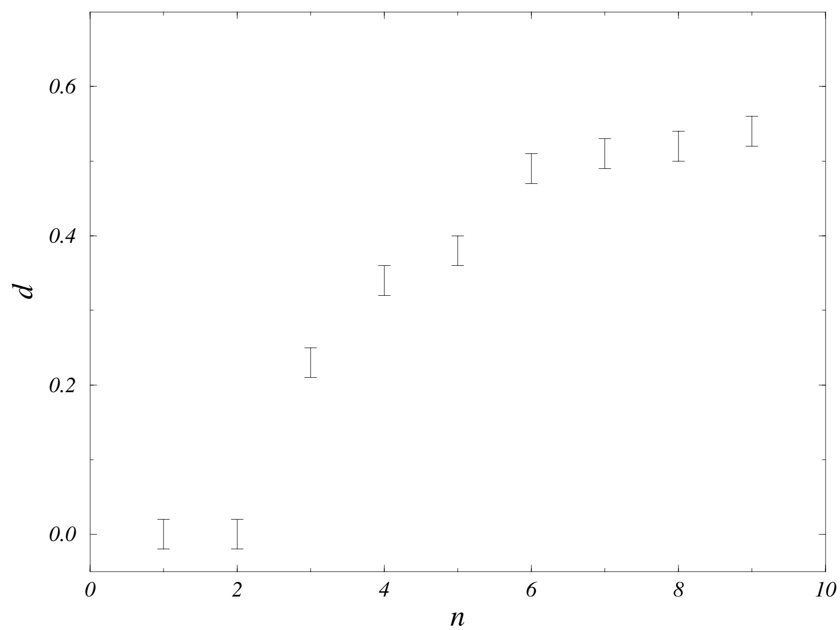

Figure B.6: Box-counting dimension d for Newtonian multipole field of order n. The error bars come from the statistical errors in the calculation of d.

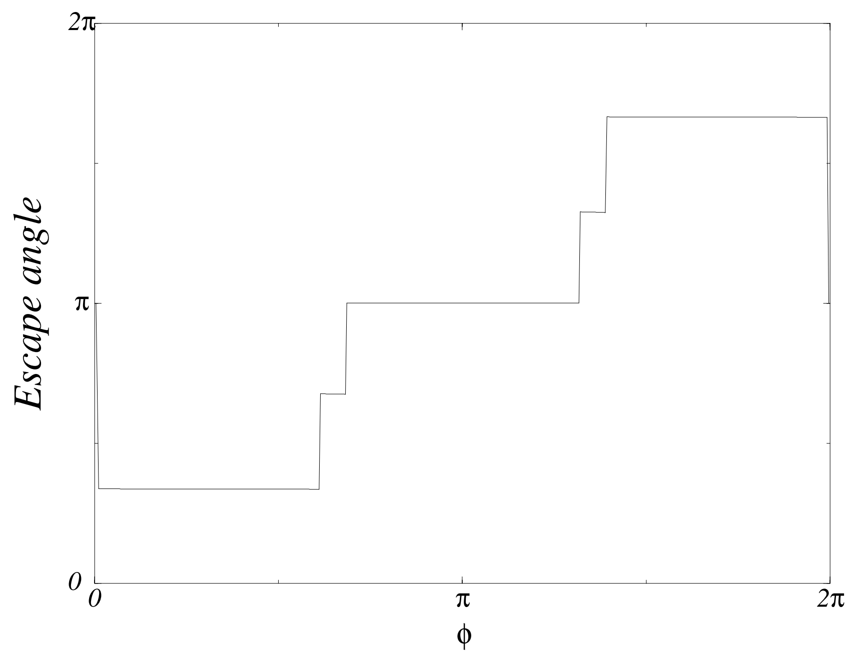

Figure B.7: Escape angle θ_e as a function of the initial velocity angle ϕ for the null geodesics in the relativistic octopole field.

Apêndice C

“Chaos and Fractals in Geodesic Motions Around a Non-Rotating Black-Hole with Halos”

Reprodução do artigo “Chaos and Fractals in Geodesic Motions Around a Non-Rotating Black-Hole with Halos”, submetido à Physical Review E.

Chaos and Fractals in Geodesic Motions Around a Non-Rotating Black-Hole with Halos

Alessandro P. S. de Moura
Instituto de Física Gleb Wataghin, UNICAMP, 13083-970
Campinas SP, Brazil

Patricio S. Letelier
Instituto de Matemática, Estatística e Ciência da Computação,
Departamento de Matemática Aplicada, UNICAMP,
13083-9790 Campinas SP, Brazil

Abstract

We study the escape dynamics of test particles in general-relativistic gravitational fields generated by core-shell models, which are used in astrophysics to model observed mass distributions, such as the interior of galaxies. As a general-relativistic core-halo system, we use exact axisymmetric static solutions of Einstein's field equations which represent the superposition of a central Schwarzschild black hole (the core) and multipolar fields from external masses (the halo). We are particularly interested in the occurrence of chaos in the escape, which is characterized by a great sensibility of the choice of escape by a test particle to initial conditions. The motion of both material particles and zero rest mass particles is considered. Chaos is quantified by the fractal dimension of the boundary between the basins of the different escapes. We find chaos in the motion of both material particles and null geodesics, but its intensity depends strongly on the halo. We have found for all the cases we have considered that massless particles are less chaotic than massive particles.

C.1 Introduction

Core-shell gravitational systems play an important role in astrophysics, because they are often good approximations to observed astronomical distributions of masses. These systems are characterized by a central massive core (possibly a black hole) and a surrounding halo of matter. The space between the core and the halo is assumed to be empty, and the gravitational field there satisfies the vacuum field equations. In real systems the assumption that the region between the core and the halo is empty is clearly not satisfied exactly, but we still expect the core-shell approximation to be valid in situations when the field in this region is dominated by the core-shell contributions.

In newtonian gravitation, a general way of treating the field by the halo is by means of a multipole expansion. Each multipole term is a solution of Laplace's equation, which increase with distance, contrary to the more usual decreasing multipoles. The field by a general halo can always be written as a linear superposition of such multipole terms. In general relativity, the situation is more complicated, because Einstein's field equations are not linear. However, in the particular case of axisymmetric (and static) vacuum fields, a general solution of the field equations is known, and this solution is parameterized by a certain metric function which is related in a simple way to the Newtonian gravitational field in the limit of weak fields, and it can be used to perform a multipole expansion. Although such expansion is by no means unique, and its relationship with the newtonian expansion is far from straightforward, it is still valuable and can be used to describe the general-relativistic gravitational field of a general halo.

This article is concerned with the motion of test particles (both massive particles and light will be considered) in a core-shell system in the region between the core (which we assume to be a non-rotating black hole) and the halo, whose gravitational field in this region is described by a multipole sum, in which we keep terms of up to the third order (octopole). The treatment is fully relativistic, using exact solutions of Einstein's equations that describe the gravitational (vacuum) field due to the superposition of the fields by a Schwarzschild black hole and the various multipole components of the halo; in some cases we also use the corresponding Newtonian field to compare the results. The motion of test particles in the core-halo field may depend on several parameters: the energy, the angular momentum, the multipole strengths, etc. Depending on the values of these parameters, the motion may be either bounded or unbounded. Bounded motion means that the particle is restricted to a finite volume of phase space; unboundedness means that a particle has access to an infinite phase-space volume. In this paper, we are interested in the escape properties of these systems. If a system has two or more physically well-defined escapes for a given set of parameters of the metric (for instance, regions where a particle runs away to infinity, or where it falls into an event horizon), then the escape it chooses is a function of its initial conditions; when this function has a fractal structure, we have a well-defined kind of chaos, and the correspondent fractal dimension gives a good quantitative characterization of the chaos, besides having a simple physical interpretation as a measure of the sensitivity to initial conditions (see section III). Since the fractal nature of the boundary between the escapes is a topological feature, it is independent of the choice of the space-time coordinates; this assures the meaningfulness of this characterization for General Relativity.

The study of chaos in dynamical systems with unbounded orbits is relatively recent [1]. The characterization of chaos for this class of problems is different from that used for bounded hamiltonian dynamics, which is based upon the destruction of KAM tori. One of the most important situations with unbounded motion is that of the escape of particles from a certain region; this problem is closely related to scattering, the difference between the two being essentially the choice of the initial conditions. Escapes have been studied for several systems: two-dimensional autonomous Hamiltonian systems [2, 3, 4], nonlinear oscillations [5, 6], two-dimensional conservative mappings [7] and inflationary cosmology [8] are only a few examples.

This paper is organized as follows: in section II we review the general vacuum static axisymmetric metric and some of its properties; in section III we define the box-counting dimension and discuss its physical significance; in section IV, we investigate the basins of escape in the motion of material particles for some choices of static axisymmetric metrics, and show numerically the existence of chaos; the axial and temporal symmetries of the space-time allow us to define a two-dimensional "effective potential", which as in the Newtonian case determines the regions in space that are accessible to the particle, thereby making the analysis of the relativistic system analogous to that of the Newtonian systems in many ways. In section V, we show that null geodesics are regular (non-chaotic) in the field of a dipolar halo (plus the black hole), but chaos arises if we add multipole moments of higher order to the halo; and in section VI we summarize our results and draw some conclusions.

C.2 The Weyl Metric

Many astrophysical systems have axial symmetry, and their mass distribution can often be approximated by a static configuration. Throughout this article, we consider only axisymmetric static gravitational fields, and use the Weyl metric to describe a general static axisymmetric space-time[9]:

$$ds^2 = e^{2\psi} dt^2 - e^{-2\psi} \left[e^{2\gamma}(dr^2 + dz^2) + r^2 d\phi^2 \right], \tag{C.1}$$

where r and z are the radial and axial coordinates, and ϕ is the angle about the z axis, which is the axial symmetry axis. Throughout this article, we will use units such that $c = 1$ and $m = 1$, where m is the mass of the central black hole (C.1). ψ and γ are functions of r and z only. In these coordinates, the vacuum Einstein equations reduce to:

$$\frac{\partial^2 \psi}{\partial r^2} + \frac{1}{r}\frac{\partial \psi}{\partial r} + \frac{\partial^2 \psi}{\partial z^2} = 0; \tag{C.2}$$

$$d\gamma = r \left[\left(\frac{\partial \psi}{\partial r} \right)^2 - \left(\frac{\partial \psi}{\partial z} \right)^2 \right] dr + 2r \frac{\partial \psi}{\partial r}\frac{\partial \psi}{\partial z} dz. \tag{C.3}$$

The first expression is just Laplace's equation in cylindrical coordinates; the second equation defines γ, once ψ is found. From Eq. (C.2) and the form of the metric (C.1) it is clear that in the weak-field limit Ψ can be identified as the Newtonian scalar gravitational field.

The metric (C.1) is independent of the time t and of the symmetry angle ϕ. From this we obtain the two constants of motion $\hat{E}$ (energy) and $\hat{L}_z$ (projection of the angular momentum on the symmetry axis), that are conserved along the trajectories of test particles in the metric (C.1). They are given by:

$$\hat{E} \equiv p_t = g_{tt}\dot{t}; \tag{C.4}$$

$$\hat{L}_z \equiv p_\phi = g_{\phi\phi}\dot{\phi}, \tag{C.5}$$

where the dot denotes differentiation with respect to the proper time in the case of a massive test particle, or an affine parameter, in the case of particles with zero rest mass. The only independent dynamical variables are thus r, z and their momenta p_r and p_z: the time evolution of t and ϕ are given by the quadratures above. This means that the dynamical system corresponding to the motion of test particles in the Weyl metric has only two degrees of freedom.

Besides the energy and the z component of the angular momentum, there is another quantity which is conserved along the trajectory of a test particle, namely its rest mass. This conserved quantity is given by:

$$g^{\mu\nu}p_\mu p_\nu = \hat{E}^2 g^{tt} + \hat{L}_z^2 g^{\phi\phi} + f(\dot{r}^2 + \dot{z}^2) = m_0^2, \tag{C.6}$$

where $f = -g_{rr} = -g_{zz} = e^{2(\psi-\gamma)}$ and m_0 is the rest mass of the test particle, which must satisfy $m_0 \ll 1$. Dividing both sides by m_0 (if $m_0 \neq 0$), we rewrite the above equation in a more convenient form:

$$E^2 g^{tt} + L_z^2 g^{\phi\phi} + f\left(\dot{r}^2 + \dot{z}^2\right) = \delta, \tag{C.7}$$

where $E = \hat{E}/m_0$ is the test particle's energy per mass, $L_z = \hat{L}_z/m_0$ is the z component of the angular momentum per mass, and the dot now means differentiation with respect to the new affine parameter obtained from the previous one by multiplication by m_0. $\delta = 1$ for massive particles, and $\delta = 0$ for particles with zero rest mass. The conservation equations for the scaled quantities E and L_z are:

$$E = g_{tt}\dot{t}; \tag{C.8}$$

$$L_z = g_{\phi\phi}\dot{\phi}. \tag{C.9}$$

Remember that the differentiation is performed with the scaled affine parameter.

The equations of motion for the test particles are:

$$\ddot{x}^\mu + \Gamma^\mu_{\alpha\beta}\dot{x}^\alpha\dot{x}^\beta = 0, \tag{C.10}$$

where $\Gamma^\mu_{\alpha\beta}$ are the Christoffel symbols. The equations for t and ϕ reduce to the quadratures (C.8) and (C.9). Using these equations and Eq. (C.1), we cast the equations for the remaining variables r and z in the convenient form:

$$\ddot{r} = -\frac{1}{2f}\left[g^{tt}_{,r}E^2 + g^{\phi\phi}_{,r}L_z^2 + f_{,r}\left(\dot{r}^2 - \dot{z}^2\right) + 2f_{,z}\dot{r}\dot{z}\right]; \tag{C.11}$$

$$\ddot{z} = -\frac{1}{2f}\left[g^{tt}_{,z}E^2 + g^{\phi\phi}_{,z}L_z^2 + f_{,z}\left(\dot{z}^2 - \dot{r}^2\right) + 2f_{,r}\dot{r}\dot{z}\right]. \tag{C.12}$$

To proceed further, it is convenient to define the prolate spheroidal coordinates u and v by:

$$z = uv; \tag{C.13}$$

$$r^2 = (u^2 - 1)(1 - v^2); \tag{C.14}$$
$$u \geq 1; \qquad -1 \leq v \leq 1.$$

In these coordinates, equation (C.2) separates, and a general solution is obtained in a series of products of Legendre polynomials and zonal harmonics [10]. We must select a class of solutions that represents the physical system we are interested in: the field (C.1) should be the result of the superposition of a Schwarzschild black hole and multipolar contributions from an external halo. It is well known that in Weyl's coordinates the black hole's event horizon the black hole is represented as a singular bar lying on the symmetry axis, the inner region being excluded from the picture[9]; the "bar" singularity is therefore due to the choice of coordinates, which do not cover the whole space-time. On the other hand, the halo field, being the result of external matter sources, cannot have singularities in the region interior to the halo. The general solution which satisfies these conditions is:

$$\psi = \frac{1}{2} \ln \left(\frac{u-1}{u+1} \right) + \sum_{n=1}^{\infty} a_n P_n(u) P_n(v). \tag{C.15}$$

The first term represents a Schwarzschild black hole with unit mass $m = 1$, and the terms under the summation sign are multipolar contributions from the halo.

Using the coordinates u and v and the expression (C.15) for ψ, γ can be obtained from a straightforward integration of Eq. (C.3); the constant of integration is chosen so as to avoid conical singularities on the z axis, by imposing $\gamma = 0$ for $r = 0$ and $|z| > 1$.

In this article, we are interested in the multipole contributions only up to the octopole term ($n = 3$ in Eq.(C.15)). Redefining the coefficients in the expansion, we can write ψ as:

$$\begin{aligned} \psi \;=\; & \frac{1}{2} \ln \left(\frac{u-1}{u+1} \right) - Duv + (Q/6)(3u^2 - 1)(3v^2 - 1) + \\ & (O/10)uv(5u^2 - 3)(5v^2 - 3), \end{aligned} \tag{C.16}$$

where D, Q and O are related to the dipole, quadrupole and octopole moments; we will refer to them as the dipole, quadrupole and octopole strengths, respectively. Now an explicit expression for γ may be found by direct integration. Since the expressions are cumbersome and not particularly illuminating, we will not write them here; they can be found in [12, 13, 14]. We only observe that due to the nonlinearity of Einstein's equation, there are nonlinear terms of interaction between the multipole terms in γ: the gravitational field due to the different terms in the expansion (C.15) is not simply the superposition of the fields due to each term separately; this is a dramatic difference between the Newtonian and the relativistic theories.

We finish this discussion by reminding again that the coordinates u and v describe the metric only outside the black hole; in these coordinates, the event horizon is given by the segment $r = 0$, $|z| \leq 1$. Since we are interested only in the motion of particles outside the event horizon, this singular behavior of the coordinates will not concern us here.

C.3 Fractal Basin Boundaries

We now review briefly some basic concepts on fractals in dynamical systems with escapes; a complete discussion is found in [1].

Systems allowing escapes have isolated unstable periodic orbits lying near the openings of the potential (we are considering Hamiltonian systems with two degrees of freedom, such as those treated here); these are the so-called Lyapunov orbits [2]. We define the *inner region* of the system to consist of the closed region in the configuration space bounded by the Lyapunov orbits and by the equipotential curves of a given energy. In order to simplify the discussion, we suppose for the moment that we have an inner region which has two distinct escapes, denoted by 1 and 2 (the generalization of the discussion for a higher number of escapes is straightforward). By *escape* we mean a route that allows the particle to leave the inner region permanently. The particular escape chosen by a particle is dependent on the initial conditions of that particle. For a given dynamical system and a given energy, the set of points in phase space which correspond to initial conditions such that the particle chooses escape 1 is the *basin* corresponding to escape 1; the basin corresponding to escape 2 is defined analogously. A point in phase space is defined to be a boundary point if every neighborhood of such a point contains points belonging to both basins. The basin boundary is the set formed by all the boundary points.

This system is chaotic if its basin boundary is fractal. Near a fractal basin boundary the points belonging to the different basins are mixed in a very complex way, down to arbitrarily small scales. If we draw a plot of the basins with a finite resolution, and amplify a region containing a fractal boundary, then no matter how much we amplify it, we will always find complex structures of intermixing points of both basins. This implies a strong dependency on the initial conditions near a fractal basin boundary.

If a system has a fractal basin boundary, then it has a fractal set of unstable "eternal" bounded orbits, that never escape in the past and in the future (orbits that have never entered nor will ever leave the inner region), called the *chaotic saddle*. The basin boundary is formed by trajectories belonging to the stable manifold of the chaotic saddle, that is, by trajectories that never escape in the future ("trapped" trajectories); the unstable manifold is formed by orbits that do not escape for $t \to -\infty$. The chaotic saddle, as well as its stable and unstable manifolds, are sets of zero measure within the phase space. The chaotic saddle is part of the full *invariant set*, which is the set of *all* eternal orbits. Notice that in general not all eternal trajectories belong to the chaotic saddle: if the system has a stable periodic orbit for energies above the escape energy, then orbits near this one will also be eternal, and they form a non-zero-measure set of eternal orbits that are not part of the chaotic saddle. For Hamiltonian systems with two degrees of freedom such as the ones considered in this article, these orbits are bounded by the outermost KAM torus, which separates the inner region filled with bounded orbits from the outer regions filled with escaping orbits (with the exception of the zero-measure set or orbits on the stable manifold of the chaotic saddle). The region of phase space bounded by the outermost KAM torus consists in general of a mixture of chaotic and regular orbits. This region is a non-hyperbolic part of the invariant set.

We note that, for a system (at a given energy) to have a fractal basin boundary, it needs not only to be non-integrable, but also it must be such as to allow the presence of such fractal set of trapped trajectories. In other words, the potential must be such that the particle can bounce back and forth many times before it escapes, if the system is to have a fractal basin boundary. An example of a non-integrable dynamical system with regular basin boundaries is given by the motion of null geodesics in the black hole plus dipole field, discussed in Section V.

The presence of a fractal set of unstable orbits is the result of transversal crossings of the stable and unstable manifolds of the Lyapunov orbits [2]. The basin boundaries between the different escapes are the stable manifolds of the Lyapunov orbits. The homoclinic and heteroclinic crossings imply a horseshoe symbolic dynamics, which is responsible for the chaos and the fractal character of the basin boundaries. The horseshoe dynamics results also in the existence of a set of countable unstable periodic orbits, that must thus exist if the system has a fractal basin boundary.

To give a quantitative measure of the sensibility to initial conditions of a system with a fractal basin boundary, we define the box-counting dimension [15] of the boundary as follows: let two points chosen randomically in a region of the phase space be separated by a small distance ϵ; it is then generally the case that the probability that the two points belong to different basins scales as:

$$P(\epsilon) \propto \epsilon^{D-d}, \tag{C.17}$$

where D is the (integer) dimension of the region where the ensemble of points was chosen; and d is the (possibly non-integer) dimension of the intersection of the basin boundary with this region. If the boundary is non-fractal, then $d = D - 1$, while if the boundary is fractal, we have $d > D - 1$. By choosing randomly a large number of points in a region of the phase space for a certain fixed ϵ, we can calculate $P(\epsilon)$ numerically, and doing this for several values of ϵ, we can calculate the fractal dimension d; this is the method we use in this article (see [15] for more details).

If our system has a stable periodic orbit for energies above escape, then as we said above it has a set of positive measure of non-escaping orbits bounded by tori in phase-space. Escaping orbits that come close to this set stay in its neighborhood for a long time before leaving; in other words this set is "sticky" [7]. This complicates the task of calculating the box-counting dimension, for it demands a greater integration time. We also observe that for this same reason, the boundary between the escaping and the non-escaping regular orbits does not have a well-defined box-counting dimension.

We observe that since the fractal structure of the basin boundary is a topological feature of the dynamical system, it is a valid characterizations of chaos in general relativity.

C.4 Dynamics of Material Particles

In this section, we study the motion of material test particles in the metric (C.16) for some choices of the multipole moments D, Q and O. Important properties of the dynamics can be understood by means of the "effective potential" associated with this metric [11].

The boundary of the region in the configuration space which is accessible to the particle is found by setting $\dot{r} = \dot{z} = 0$ in Eq. (C.7), with $\delta = 1$ for massive test particles:

$$E^2 g^{tt} + L_z^2 g^{\phi\phi} - 1 = 0. \tag{C.18}$$

The "effective potential" $V(r,z)$ is then given by:

$$V(r,z) \equiv E^2 = \frac{1 - L_z^2 g^{\phi\phi}}{g^{tt}}; \tag{C.19}$$

Substituting for the Weyl metric (C.1), we have:

$$V(r,z) = e^{2\psi}\left(1 + \frac{e^{2\psi} L_z^2}{r^2}\right); \tag{C.20}$$

The region on the rz plane accessible to the particle is given by $V(r,z) \leq E^2$. Using equation (C.16) for ψ, we thus have an expression for the effective potential in terms of the multipole moments. We note that V depends only on ψ, and not on γ.

In the following subsections, we will analyze the dynamics for some interesting choices of D, Q and O. For bounded trajectories, this system was shown through Poincaré sections to be chaotic [12, 13, 14].

C.4.1 Dipole Potential

If we make $Q = O = 0$ in (C.16), we have a pure dipole field together with a Schwarzschild black hole. The Newtonian system equivalent to this is the field due to a point mass superposed to a Newtonian shell dipole field, which is simply a field of constant acceleration. Bounded trajectories of the relativistic system have been studied, and chaos has been found using Poincaré sections[13]; the Newtonian system can be shown to be integrable, so the chaos is due to general relativistic contributions to the dynamics. We shall now study this system in the open regime, that is, with energies large enough as to allow them to escape either to infinity or to the event horizon.

In Figure 1 we show some contour levels of the effective potential $V(r,z)$ for $D = 3 \times 10^{-4}$ and $Q = O = 0$, with $L_z = 3.0$. The first feature we notice is the "tunnel" formed by the equipotential curves for small values of r, that leads to the event horizon (remember that in these coordinates, the event horizon is given by $r = 0$ and $|z| \leq 1$). This is the route followed by particles that fall into the black hole. We observe that V is invariant under the transformation $z \to -z; \quad D \to -D$.

If a particle has high enough energy (E^2 higher than about 0.94 for the parameters of Fig. 1), it can also escape to infinity. This is shown clearly in Fig. 1 by the opening that appears in the equipotentials for high energies.

Now let us pick one specific value for the energy, for instance $E^2 = 0.95$. At this energy, a particle's orbit can have three outcomes: (1) escape into the black hole; (2) escape to infinity; and (3) keep bouncing back and forth forever, and never leave the inner region.

To investigate the nature of the basin boundaries, we need a portrait of the basins; to do this, we define a 2-dimensional section of the 3-dimensional energy shell of the phase space that is accessible to the particle. For $E^2 = 0.95$ we define this section as the set of initial conditions with spatial coordinates lying on the segment given by $z = 0$ and $15 \leq r \leq 25$, with velocities given by:

$$\dot{r} = v\cos(\theta); \qquad \dot{z} = v\sin(\theta), \tag{C.21}$$

where

$$v = (\dot{r}^2 + \dot{z}^2)^{1/2} = \frac{1}{f}\left(1 - E^2 g^{tt} - L_z^2 g^{\phi\phi}\right) \tag{C.22}$$

is defined by the conservation equation (C.7) with $\delta = 1$, and $0 \leq \theta \leq 2\pi$. This section is thus a topological segment of a cylinder embedded within the phase space, and we will denote it by S.

To obtain numerically the intersection of the basins with this section, we divide the intervals $15 \leq r \leq 25$ and $0 \leq \theta \leq 2\pi$ into 400 equal parts each; this defines a grid on S composed of 400×400 points. For each of these points, we integrate numerically the equations of motion for the dipole metric, and record the outcome: if the trajectory falls into the black hole (numerically, if r becomes too small, or less than 0.5 in this case), that initial condition belongs to basin 1; if the trajectory escapes to infinity (numerically, if r or z becomes too large, larger than 60 in this case), it belongs to basin 2; and if after a certain proper time τ_{max} (in this case we have chosen $\tau_{max} = 100000$; for reference, the typical exit time is about 2000) the trajectory chooses none of the two escapes above, then we admit that it belongs to the set of "trapped" trajectories that never leaves the confining region. We choose τ_{max} such that the set of "trapped" trajectories is well resolved for the scale of the grid we use.

The results of this calculation are shown in Fig. 2a. A black dot means that the corresponding point (r, θ) in S belongs to basin 1; a white dot indicates that it belongs to basin 2; and a grey dot means it belongs to the set of "trapped" trajectories. We notice a complex Cantor-like mixing of basins, indicating that the structure continues down to smaller scales. This is confirmed by the amplification of a detail of Figure 2a, shown in Fig. 2b. The area covered by Fig. 2b is about 10 orders of magnitude smaller than that of Fig. 2a, giving strong evidence that the basin boundary is indeed fractal. We note that the set of trapped trajectories has a non-zero measure; this is clear from Fig. 2a. In Fig. 3a, which shows the intersection of some of these trapped orbits with the surface of section $z = 0$. The parameters are the same as in Fig. 2.

To have a more precise and quantitative characterization of the fractal structure seen in Fig. 2, we proceed to the calculation of the fractal dimension, as discussed in section III. The random points are chosen in S, and for each point (r, θ) we find through numerical integration to which of the basins it belongs, and then do the same for two nearby phase space points given by $r + \epsilon$ and $r - \epsilon$ and the same θ. If all three points do not belong to the same basin, then the point (r, θ) is considered an "uncertain" point, meaning that it lies close to a basin boundary. For a large number N of points randomly chosen in S, the fraction of uncertain points is $f(\epsilon) = N'/N$, where N' is the number of uncertain points found in the sample of N points. For N large enough, f is proportional to P in Eq. (C.17); finding in this way f for several values of ϵ, a log-log plot of $f(\epsilon)$ should give a straight line, and the basin boundary dimension d is found by the angular coefficient through Eq. (C.17). For reasons explained in sec. III, we calculate d choosing points in a region that does not intersect the trapped region bounded by KAM tori. By getting rid in this way of the "stickiness" of the regular region, we are able to obtain a meaningful result for d.

The results are shown in Fig. 3b. We have chosen N such that $N' > 100$; this means a statistical uncertainty of about 10% in f. We see that the points lie on a clearly defined straight line; the angular coefficient is $\alpha = 0.47 \pm 0.02$, which gives a dimension of $d = 1.53 \pm 0.02$, showing unambiguously that the boundary is fractal. We remember that d is the dimension of the intersection of the basin boundary with the 2-dimensional section S; the dimension of the basin boundary in the accessible 3-dimensional space is $d + 1$. We have calculated d for some subregions of S, and we have obtained always the same value to within the statistical uncertainty, showing that the method is self-consistent and the result is meaningful.

We have studied how the box-counting dimension changes as we change the various parameters of the metric. If $D = 0$, a particle needs an energy

E higher than 1 to be able to escape to infinity. If $D \neq 0$, the escape energy becomes less than 1, and depends on the angular momentum L_z. We denote the escape energy by $E_0 = E_0(L_z)$. The basin boundary dimension d is defined only for $E > E_0$. We have found that for $E > 1$, $d = 1$ (to within the statistical error), and the basin boundary is regular. We have verified this result for several values of L_z and E, and three different values of D.

We have also investigated how d changes with the dipole strength D. In the limit $|D| \to \infty$, we have a field dominated by the dipole component; the geodesics defined by a pure dipole field are integrable, and thus we expect d to approach 1 for high values of D. If we decrease D enough, we end up reaching a value D_0 below which the particle can no longer escape to infinity, and d is no longer well defined. Near $D = D_0$, with $D > D_0$, the opening of the equipotential to the escape to infinity is small, and the particle is likely to bounce more times before it escapes through this route than in the case of higher values of D, and we accordingly expect the chaos to be "larger" in this case, that is, d to be larger. These features are indeed verified in a plotting of d versus D for $E^2 = 0.95$ and $L_z = 3.0$, shown in Fig. 4. For these values of D and L_z, we have $D_0 \equiv 2.5 \times 10^{-4}$. The system is regular ($d = 1 \pm 0.01$) for $D \geq 9 \times 10^{-4}$, and d reaches its highest value of about 1.6 at $D = D_0$.

C.4.2 Quadrupole Potential

We next turn to the case $D = O = 0$. This quadrupole field has a reflection symmetry with respect to the z axis: the metric is unchanged by $z \to -z$. For the oblate case ($Q > 0$), the open equipotentials are similar to the pure dipole case discussed above (except for the aforementioned symmetry). A more interesting choice is $Q < 0$ (prolate case); in this case, as shown in Fig. 5, there are two different escapes to infinity, besides the escape into the event horizon. We investigate this system for the energy $E^2 = 0.97$, with $L_z = 2.6$ and $Q = -4 \times 10^{-6}$. For these parameters, the invariant set appears to have zero measure, since we were able to find no stable orbit in the inner region.

We proceed as we did for the dipole case. We choose initial conditions in the segment $r = 25.0$, $|z| < 25.0$; the velocities are given by (C.21). The results are in Fig. 6a, with black dots denoting trajectories that escape upwards, white dots denoting trajectories that escape downwards, and grey dots denoting trajectories that fall into the event horizon. Figure 6b shows an amplification of a very small area of Fig. 6a, and the absence of smoothness in the basin boundary shows clearly its fractal character. The fractal dimension was computed as described above, and the value we obtained was $d = 1.60 \pm 0.03$. In the corresponding oblate case, with $Q = +4 \times 10^{-6}$ and all other parameters being equal, we found no detectable chaos, and the basin boundary was found to be regular, with $d = 1$ to within our numerical accuracy. This is in agreement with the results found in [14], where it was found (by using Poincaré sections) that for a black hole plus oblate quadrupole field the bounded orbits show an almost regular behavior, the chaotic regions being restricted to very small volumes in phase space, while the corresponding prolate field shows strong chaos.

We have calculated d for other values of the energy and angular momentum, and we found that, as opposed to the dipolar halo system studied in the previous section, this system is chaotic for $E > 1$. In fact, we found that the boundary is fractal for arbitrarily large values of the energy (for $Q < 0$), as far as we have been able to investigate; this appears to be an important difference between the dipolar and quadrupolar halos.

Since the basin boundary between the escapes is the stable manifold of the chaotic saddle, we have associated with the chaos in the choice of the escape route a chaos in the escape time as well, as is well-known in chaotic scattering. This happens because orbits starting from very close initial conditions may make a different number of bounces before escaping, leading to very different escape (proper) times. We have illustrated this by finding numerically the escape proper times τ_e for orbits starting from a fixed position $r = 25$, $z = 0$, for several velocity angles θ, as defined by Eq. (C.21). We plot $\tau_e(\theta)$ in Fig. 7a. The "spiked" character of the graph is striking, suggesting a fractal structure. This is confirmed by Fig. 7b, which shows that the function $\tau_e(\theta)$ has a fractal set of singular points, where $\tau_e(\theta)$ goes to infinity; this set is the intersection of the line of initial conditions with the basin boundary. We observe that the escape time τ_e is to some extent arbitrary, because it depends on where we stop the integrations of the trajectories before we consider them to have escaped. However, the fractal structure seen in Fig. 7 is topological, and is not affected by this choice. These features of the escape time function remain the same for r and z within the inner region.

In order to gain more insight into the fractal structure of the basin boundary and its related complex dynamics, we now define a surface of section in phase space denoted by $\mathcal{P}$ and given by $\dot{z} = 0$, for a given E and L_z. We define I_n $(n \geq 1)$ as the set of points on the surface of initial conditions S that generate orbits that cross $\mathcal{P}$ at least n times in the negative direction (that is, satisfying $\ddot{z} < 0$) before escaping. Obviously I_n is a subset of I_k if $k < n$, and we have that:

$$I_1 \supset I_2 \supset I_3 \supset \cdots . \tag{C.23}$$

For systems without KAM tori (as appears to be the case of the quadrupole field with the parameters of Fig. 7), the basin boundary is given by $\lim_{n\to+\infty} I_n$. If we let I_n, with n being a negative integer, denote the set of points in S corresponding to past-directed orbits which cross $\mathcal{P}$ in the negative direction at least $|n|$ times, then the unstable manifold of the chaotic saddle is analogously given by $\lim_{n\to-\infty} I_n$. Defining now the set $R_n = I_n \cap I_{-n}$, the chaotic saddle is given by $\lim_{n\to+\infty} R_n$. This simply states that the chaotic saddle is the intersection of its stable and unstable manifolds.

The mechanism of the construction of the fractal basin boundary by the dynamics of the system may be followed by examining the sets I_n ($n > 0$). Figs. 8a, 8b and 8c show I_1, I_2 and I_3 respectively, using the same grid as that of Fig. 7a. As n increases, the structure of I_n becomes more and more complicated: every step $I_n \to I_{n+1}$ results in taking from I_n increasing numbers of ever thinner strips, alternately. We recognize this as the mechanism for the construction of a Cantor set, in the limit $n \to +\infty$.

We can follow in the same way the construction of the chaotic saddle itself: in Fig. 8d we show R_2; compare this with Fig. 8b.

The Newtonian system equivalent to the multipole field we are dealing with is given by the Hamiltonian:

$$H = \frac{1}{2}\left(p_r^2 + p_z^2\right) + V(r,z), \tag{C.24}$$

where $V(r,z)$ is the effective potential:

$$V(r,z) = \frac{L_z^2}{2r^2} - \frac{1}{r} + \psi(r,z), \tag{C.25}$$

and ψ is given by (C.16). For the dipole field ($Q = O = 0$), as we mentioned before, the Hamiltonian (C.24) is integrable. For the quadrupole field, however, it is not[12], so we expect to have a fractal basin boundary for this case as well. Figure 9 shows some level contours of V with $L_z = 2.6$ and $Q = -4 \times 10^{-6}$, $D = O = 0$; these are the same parameters we have used for the relativistic case. For this negative value of Q, we have two escapes (for

$Q > 0$, there is only one escape). Since we want to compare the Newtonian and the relativistic cases, we choose the energy to be $E - 1$, where E is the energy we used in the relativistic case, which gives -0.0151. We proceed as in the relativistic case to calculate the basin boundary dimension. The initial conditions are chosen in the segment $|z| < 5$, $r = 13$. The result is $d = 1.64 \pm 0.02$, which is roughly the same (actually a little larger) value we obtained for the relativistic case.

C.4.3 Quadrupole + Octopole Potential

The last case we investigate in this section is the field formed by the superposition of the quadrupole and octopole components, $D = 0$ with $Q, O \neq 0$. The octopole term breaks the reflection symmetry of the quadrupole potential, as can be seen in Fig. 10, which shows some level contours of the effective potential for $D = 0$, $Q = -4 \times 10^{-6}$, $O = -1 \times 10^{-7}$ and $L_z = 2.6$. We still have three escapes as in the previous case, but the equipotentials are distorted, and are no longer symmetrical with respect to the $z = 0$ axis. We select the energy $E^2 = 0.97$, and pick the initial conditions on the segment $|z| < 20$, $r = 20$. Using these parameters, we have calculated the basin boundary dimension, and found $d = 1.59 \pm 0.02$, which is practically the same value obtained for the pure quadrupole field $O = 0$. If we calculate d for the pure octopole field $O = -10^{-7}$, $Q = 0$, keeping the other parameters fixed, we find $d = 1.70 \pm 0.02$, which is *larger* than the value obtained for the mixed field. This is a somewhat surprising result, and it shows that a "more complicated" field does not necessarily result in a more complicated (or "more chaotic") motion.

C.5 The Null Geodesics

We will now study the dynamics of the null geodesics in the metric (C.16). For null geodesics, $ds^2 = 0$ and $\delta = 0$ in Eq. (C.7), and we have:

$$E^2 g^{tt} + L_z^2 g^{\phi\phi} + f(\dot{r}^2 + \dot{z}^2) = 0, \tag{C.26}$$

with $f = -g_{zz} = -g_{rr}$. The effective potential is then given by:

$$\frac{E^2}{L_z^2} \equiv \frac{1}{b^2} = V(r, z) = -\frac{g^{\phi\phi}}{g^{tt}} = \frac{e^{4\psi}}{r^2}, \tag{C.27}$$

where b is the impact parameter with respect to the z axis. The curve $V(r,z) = 1/b^2 =$ constant is the boundary of the accessible regions of the rz plane to a particle having an impact parameter of b. We notice that in the case of massive particles, the effective potential depends separately on E and L_z, while for the case of massless particles, it only depends on the ratio $E/L_z = b$. The equations of motion for the null geodesics are Eqs. (C.11) and (C.12), together with the quadratures (C.8) and (C.9), with E and L_z related by $b = L_z/E$. The initial conditions must be such as to satisfy the constraint (C.26).

In the case of the dipole field ($Q = O = 0$), we find that below a certain value of the impact parameter b the equipotential curves open, and the orbits can either fall into the event horizon or escape to infinity. We find, however, by numerical calculations of pictures of the basins, which show regular basin boundaries, and by the computation of the basin boundary dimension, which gives $d = 1$ to within the statistical uncertainty, that the basin boundaries are regular and the system presents no chaos. This result holds for all values of D and b we have investigated, and it seems safe to conclude that massless test particles in the field of a black hole surrounded by a dipolar material halo move in regular orbits.

When we introduce terms of higher order in the multipolar expansion of the halo, this situation changes. We illustrate this with a pure quadrupolar halo. If $Q > 0$, there are only two escapes (towards infinity and towards the event horizon), and the orbits are again regular. If $Q < 0$, however, we have three escape routes (towards the event horizon, towards $z \to \infty$ and towards $z \to -\infty$), and chaotic behavior arises. This can be seen in Fig. 11, where we show some equipotential curves for $Q = -0.05$, with $D = O = 0$. Choosing $b^2 = 12.5$, we obtain a picture of the basins by numerical integration, with the initial conditions in the segment $r = 2$, $|z| < 2$. The result is shown in Fig. 12a, and an amplification of several orders of magnitude shows (Fig. 12b) that the basin boundary is fractal. This is further confirmed by the calculation of the basin boundary box-counting dimension, which yields $d = 1.25 \pm 0.02$. We have verified that an octopole halo also gives rise to chaos, as is probably the case for multipole terms of higher order.

Now we make some general remarks on the motion of massless particles in the metric (C.16). The absence of stable periodic orbits, and therefore of a non-zero measure set of confined orbits, was verified in all cases we have investigated, leading us to make the hypothesis that this is a general feature of the motion of zero mass particles in the black-hole-halo field; we speculate that this may be the case for all static axisymmetric metrics. We also observed that in all cases in which there are only two escapes (as for instance in the dipolar halo field and in the quadrupolar field with $Q > 0$), the motion of zero rest mass particles is always regular, as opposed to the motion of material particles in the same fields. When there are three or more escapes, on the other hand, chaotic behavior appears. We have found, however, that the motion of massless particles is always less chaotic (that is, the box-counting dimension d of the basin boundary is lower) than the motion of massive particles for the same field, for all cases considered by us.

C.6 Conclusions

In this article we have considered core-shell gravitational models, which could describe inner regions of elliptical galaxies. Our study focused on the dynamics of test particles moving in the gravitational field of such objects, and we have particularly studied unbounded motions and their associated escape dynamics, both for massive test particles and for light.

In the case of massive particles, chaos was found in the form of fractal basin boundaries. We single out the case of a dipolar halo, which has a Newtonian counterpart that is known to be integrable; the chaos for this case is thus a result of relativistic corrections to the dynamics. This is compatible with earlier results obtained with bounded orbits [12]. Also for this case, we have investigated the set of trapped orbits with non-zero measure, and we showed that it is formed by orbits which are bound by KAM tori in phase space. This means that even for energies above the escape energy, there are regions in phase space wherein the motion remains bounded. Such stable regions are surrounded by unstable ones, where particles either fall into the black hole or escape to infinity, these two outcomes being separated in phase space by a fractal basin boundary.

We have found that the core-dipole system is not chaotic for energies above 1, which is the escape energy for an isolated non-rotating black-hole. The system appears to be most chaotic (its boundary dimension attains its highest value) for energies near escape.

If the halo is composed by a pure quadrupole term, the situation changes. For a prolate halo ($Q < 0$), there can be three escape routes, as opposed to only two present in the dipole case, and in this case the system is chaotic for arbitrarily large values of the energy, as far as we could determine. Oblate halos ($Q > 0$) show no detectable chaos for the parameters we have used, as opposed to the prolate ones. This is in agreement with results found previously for bounded orbits[14], which show that oblate halos have very little chaos.

In the case of massless particles (null geodesics), we find that the black hole + dipolar halo system is not chaotic, the basin boundary between the escapes being regular for all values of the parameters we have investigated. If we add a quadrupole term to the halo, the motion becomes chaotic if $Q < 0$; the orbits are still regular for $Q > 0$, further confirming that oblate halos are a weak source of chaos. Terms of higher order also introduce chaos in the system. Contrary to the case of material particles, we have not found any stable periodic orbit, with its accompanying non-zero measure set of confined orbits. We believe the absence of stable periodic orbits of massless particles is a general feature of axisymmetric static gravitational fields.

Acknowledgments

This research was partially funded by FAPESP and CNPq.

Bibliography

[1] E. Ott, *Chaos in Dynamical Systems*, Cambridge University Press, Cambridge (1993)

[2] G. Contopoulos, Astron. Astrophys. **231**, 41 (1990)

[3] G. Contopoulos, H. E. Kandrup, D. Kaufmann, *Physica D* **64**, 310 (1993)

[4] S. Bleher, C. Grebogi, E. Ott and R. Brown, Phys. Rev. A **38**, 930 (1988)

[5] J. M. T. Thompson, Proc. R. Soc. Lond. A **421**, 195 (1988)

[6] H. B. Stewart, J. M. T. Thompson, Y. Ueda, A. N. Lansbury, Physica D **85**, 259 (1995)

[7] F. Christiansen, P. Grassberger, Phys. Lett. A **181**, 47 (1993)

[8] N. J. Cornish and J. J. Levin, Phys. Rev. D **53**, 3022 (1996)

[9] D. Kramer, H. Stephani and E. Herlt, *Exact Solutions of Einstein's Field Equations*, Cambridge University Press, Cambridge, 1980

[10] A. G. Webster, *Partial Differential Equations of Mathematical Physics*, Dover Publications, New York (1966)

[11] C. W. Misner, K. S. Thorne, J. A. Wheeler, *Gravitation*, W. H. Freeman and Company, New York (1973)

[12] W. M. Vieira and P. S. Letelier, Phys. Rev. Lett. **76**, 1409 (1996)

[13] W. M. Vieira and P. S. Letelier, Phys. Lett. A **228**, 22 (1997)

[14] W. M. Vieira and P. S. Letelier, Ap. J. **513**, 383 (1999)

[15] C. Grebogi, S. W. McDonald, E. Ott and J. A. Yorke, Phys. Lett. **99A**, 415 (1983)

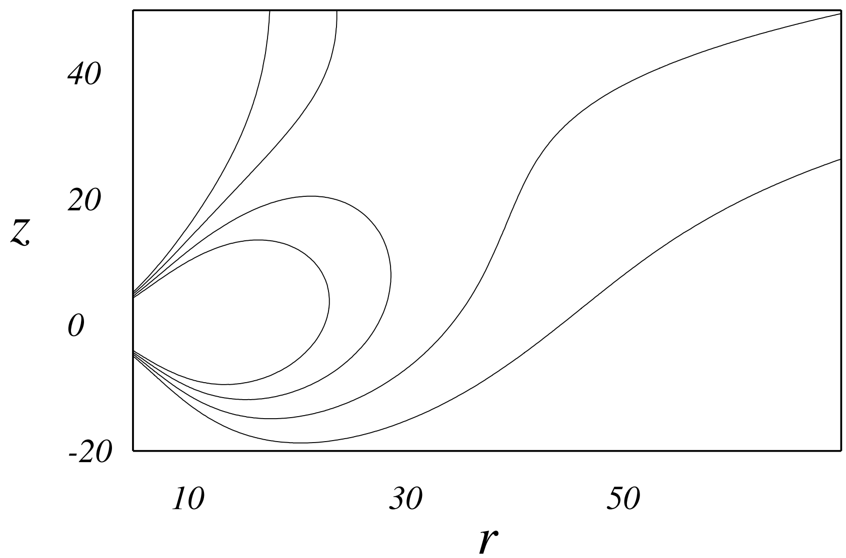

Figure C.1: Level contours of the effective potential for the dipole field ($Q = O = 0$), with $D = 3 \times 10^{-4}$ and $L_z = 3.0$. The values of E^2 for the equipotentials are, from the inside out, 0.93, 0.94, 0.95 and 0.96. Since we have chosen units such that $G = c = m = 1$ (m is the black hole's mass), all quantities in this and the other Figures are dimensionless. In regular units, r and z are given in units of Gm/c^2, which is half the Schwarzschild radius of the black hole.

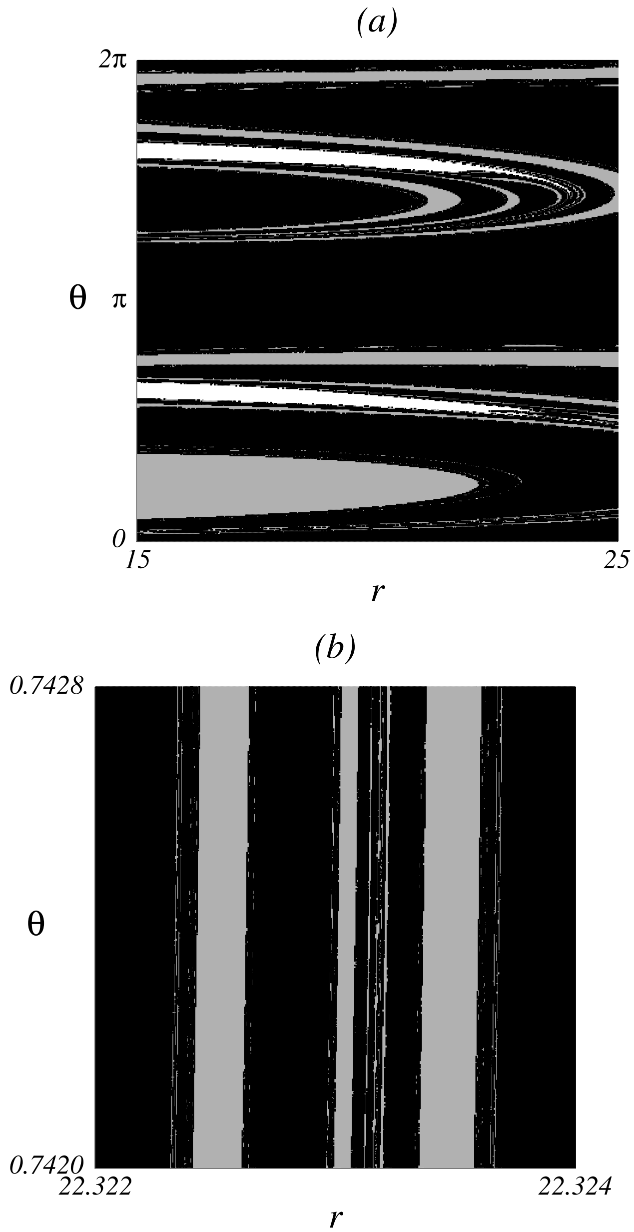

Figure C.2: Basin portrait of the section S of the phase space for the dipole field, with initial conditions on the axis $z = 0$, for $D = 3 \times 10^{-4}$, $L_z = 3.0$ and $E^2 = 0.95$. The black areas correspond to regions of S whose trajectories fall into the event horizon; white areas correspond to trajectories that escape to infinity; and grey areas correspond to trajectories that remain trapped inside the confining region. This Figure was calculated on a grid of 400×400 points. (b) is a magnification of (a).

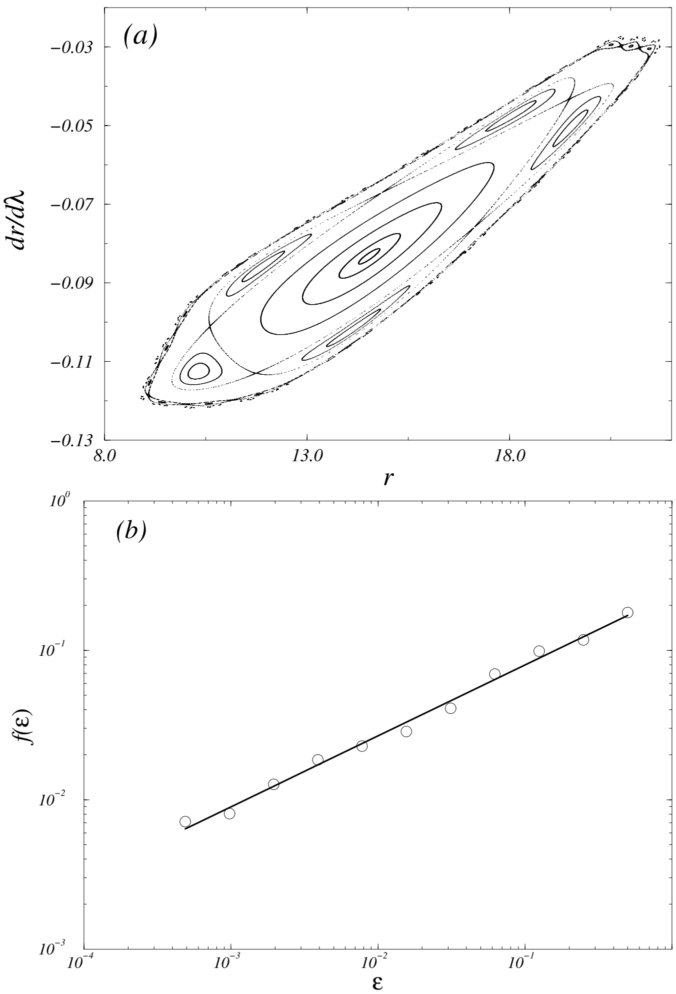

Figure C.3: (a) Poincaré section of trapped orbits, with the surface of section $z = 0$, for $D = 3\times10^{-4}$, $L_z = 3.0$ and $E^2 = 0.95$; λ is an affine parameter. (b) Plot of the fraction of "uncertain" points $f(\epsilon)$ as a function of the separation ϵ.

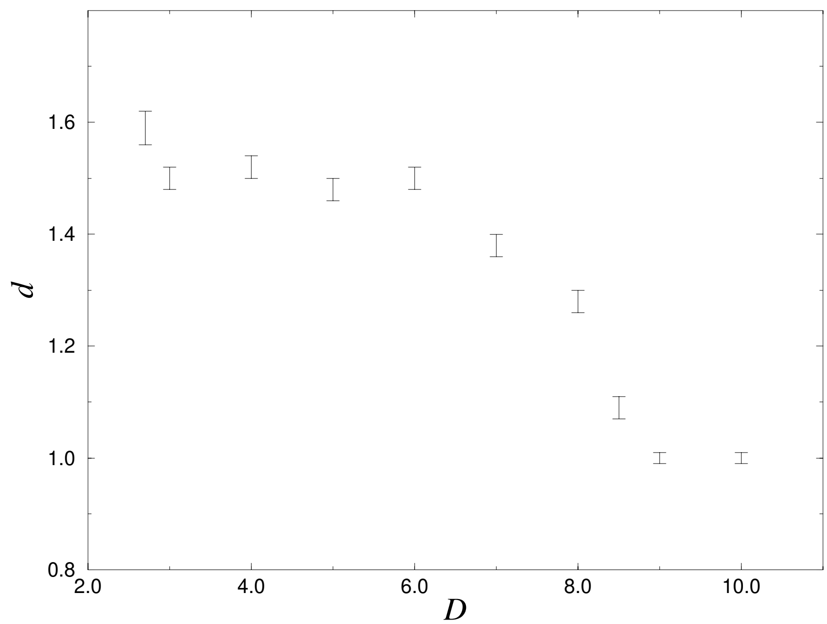

Figure C.4: Box-counting dimension of the basin boundary as a function of the dipole strength D, for $E = 0.95$ and $L_z = 3.0$.

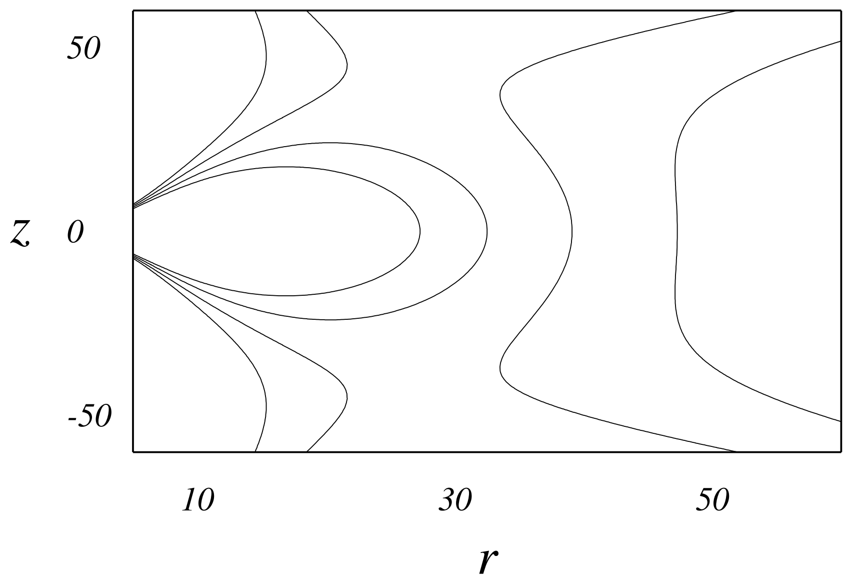

Figure C.5: Level contours of the effective potential for a quadrupole field ($D = O = 0$) with a prolate halo ($Q = -4 \times 10^{-6}$) and $L_z = 2.6$. The values of E^2 for the equipotentials are, from the inside out, 0.93, 0.94, 0.95 and 0.96.

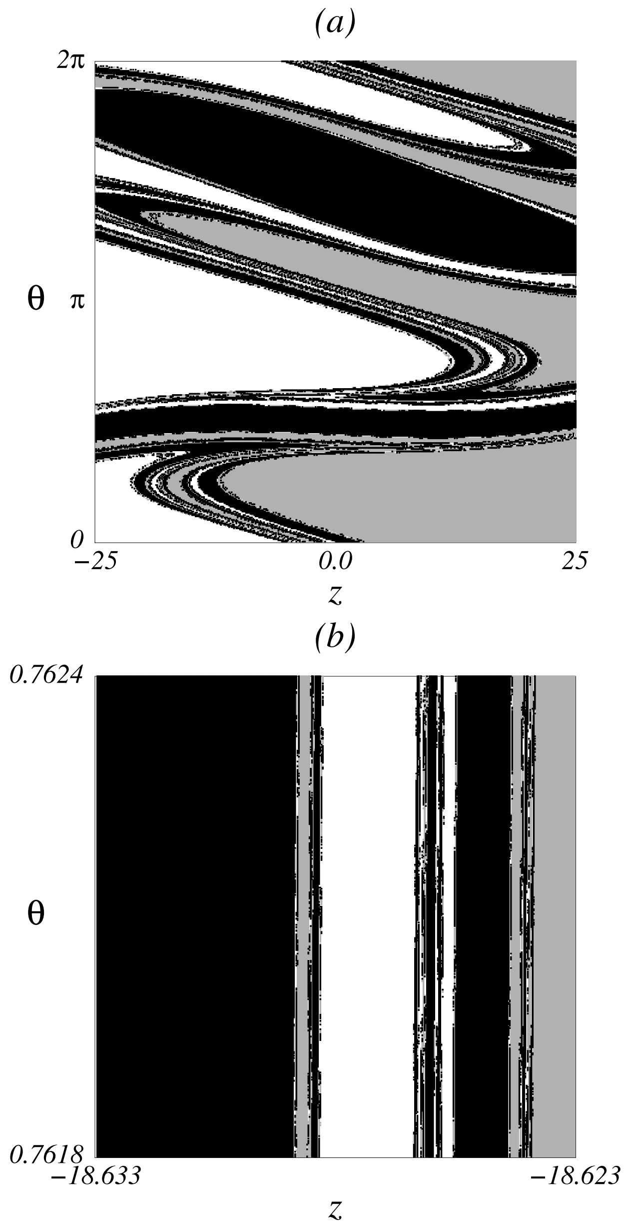

Figure C.6: Basin portrait for the quadrupole field, with $Q = -4 \times 10^{-6}$ and $L_z = 2.6$. Black areas denote regions whose trajectories fall into the event horizon; gray areas correspond to trajectories that escape towards $z \to +\infty$; and white areas correspond to trajectories that escape towards $z \to -\infty$. (b) is a magnification of (a).

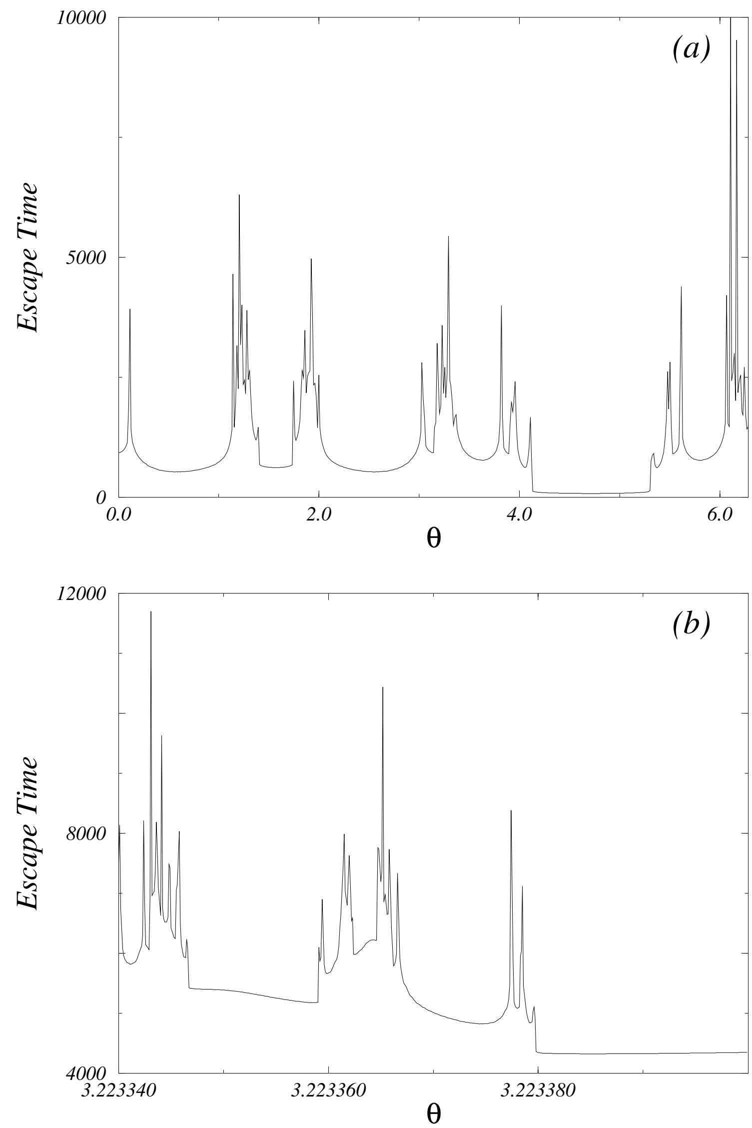

Figure C.7: Time of escape versus the velocity angle ($Q = -4 \times 10^{-6}$, $L_z = 2.6$), for $r = 25$ and $z = 0$. (b) is a magnification of (a).

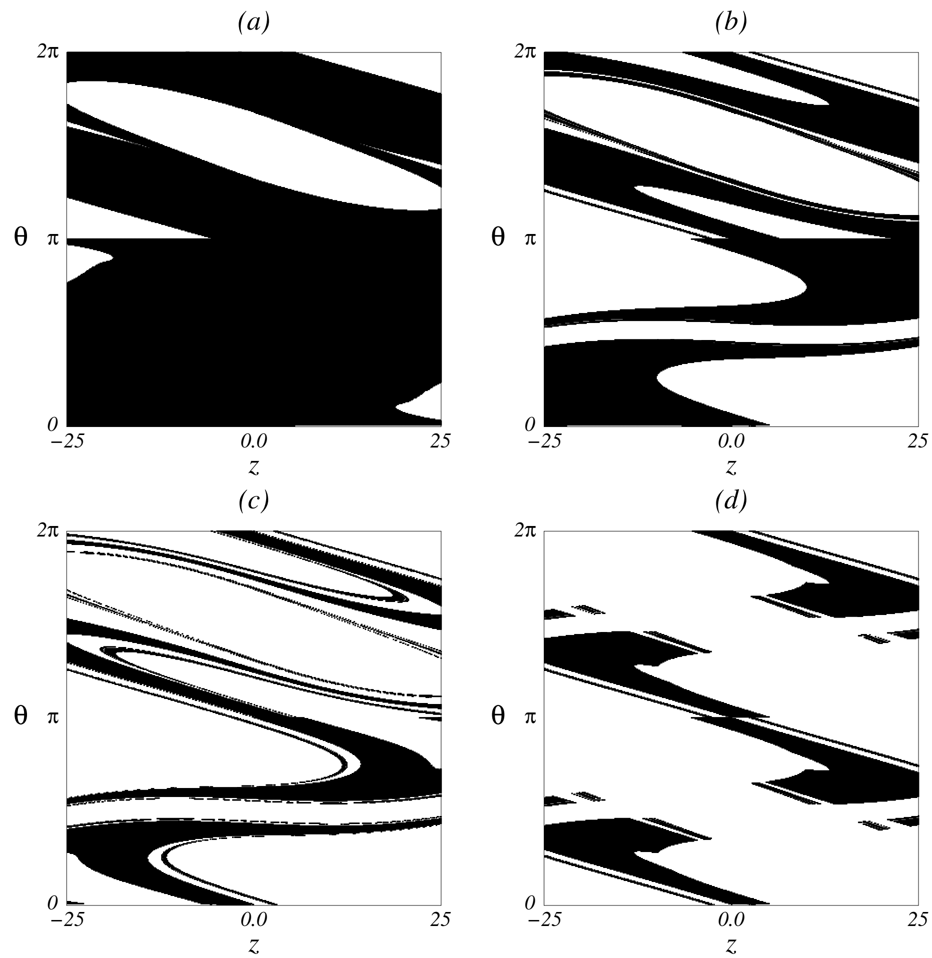

Figure C.8: (a) I_1, (b) I_2, (c) I_3, (d) R_2, for $Q = -4 \times 10^{-6}$, $L_z = 2.6$ and $D = O = 0$.

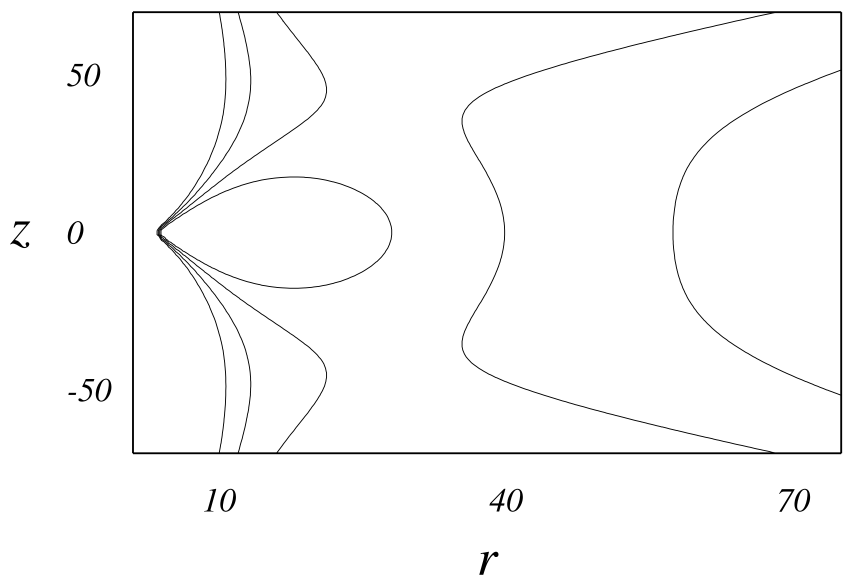

Figure C.9: Level contours of the effective potential for the classical quadrupole field with $Q = -4 \times 10^{-6}$ and $L_z = 2.6$. The values of E^2 for the equipotentials are, from the inside out, 0, -0.01, -0.02 and -0.03.

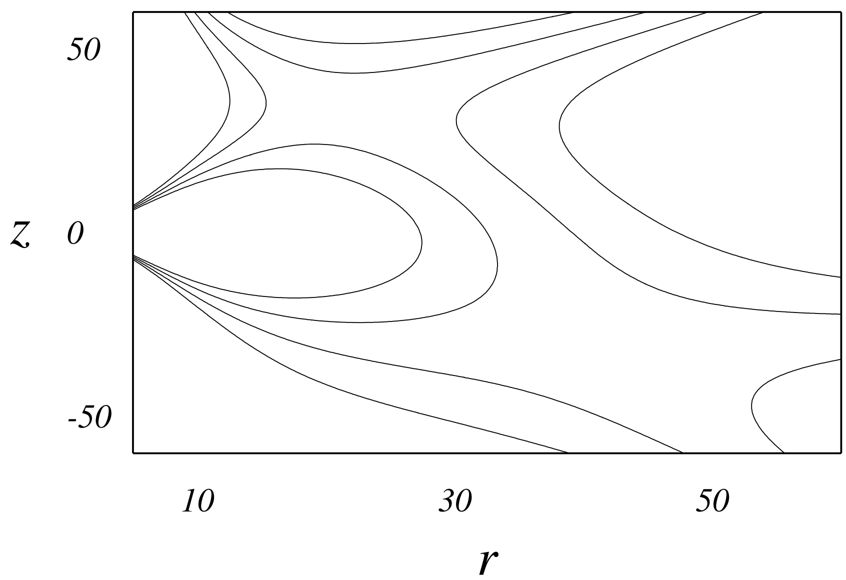

Figure C.10: Level contours of the effective potential for the field with $D = 0$, $Q = -4 \times 10^{-6}$, $O = -10^{-7}$ and $L_z = 2.6$. The values of E^2 for the equipotentials are, from the inside out, 0.94, 0.95, 0.96 and 0.97.

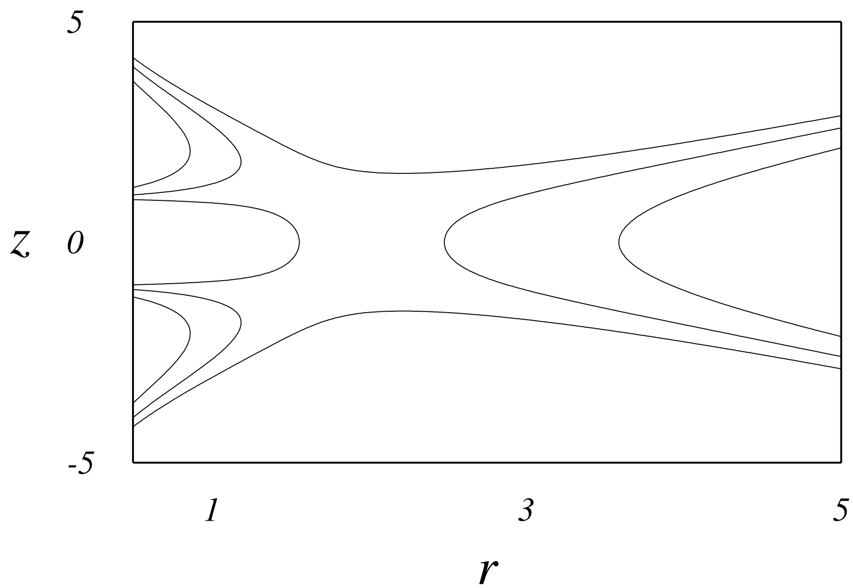

Figure C.11: Level contours of the effective potential for null geodesics for the quadrupole field $Q = -0.05$, $D = O = 0$. The values of b^2 (b is the impact parameter with respect to the symmetry axis) are, from the inside out, 10.0, 15.0 and 20.0.

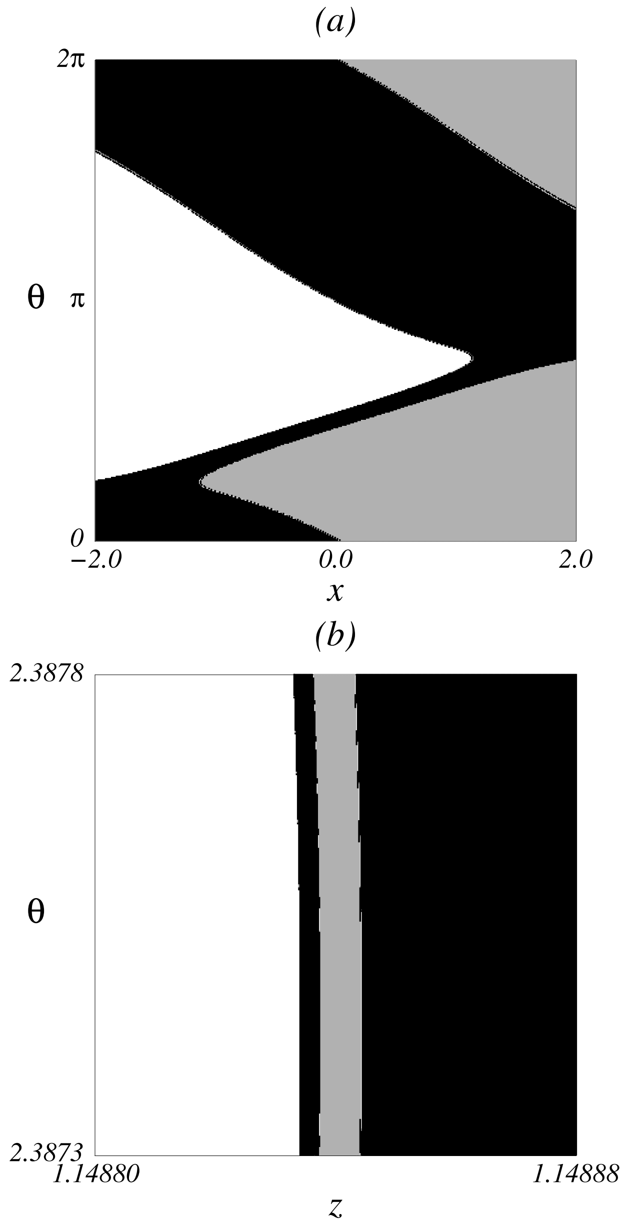

Figure C.12: Basin portrait for null geodesics with $Q = -0.05$, $D = O = 0$ and $b^2 = 12.5$. Areas in black correspond to trajectories that fall into the event horizon; areas in gray correspond to trajectories that escape towards $z \to +\infty$, and areas in white denote trajectories that escape to $z \to -\infty$.

Apêndice D

"Scattering Map for Two Black Holes"

Reprodução do artigo "Scattering Map for Two Black Holes", submetido à Physical Review E.

Scattering Map for Two Black Holes

Alessandro P. S. de Moura
Instituto de Física Gleb Wataghin, UNICAMP, 13083-970
Campinas SP, Brazil

Patricio S. Letelier
Instituto de Matemática, Estatística e Ciência da Computação,
Departamento de Matemática Aplicada, UNICAMP,
13083-9790 Campinas SP, Brazil

Abstract

We study the motion of light in the gravitational field of two Schwarzschild black holes, making the approximation that they are far apart, so that the motion of light rays in the neighborhood of one black hole can be considered to be the result of the action of each black hole separately. Using this approximation, the dynamics is reduced to a 2-dimensional map, which we study both numerically and analytically. The map is found to be chaotic, with a fractal basin boundary separating the possible outcomes of the orbits (escape or falling into one of the black holes). In the limit of large separation distances, the basin boundary becomes a self-similar Cantor set, and we find that the box-counting dimension decays slowly with the separation distance, following a logarithmic decay law.

D.1 Introduction

In this article, we study the motion of light (null geodesics) in the gravitational field of two non-rotating Schwarzschild black holes. In general relativity, solutions of the field equations describing more than one purely gravitational sources are necessarily non-stationary, because gravity is always attractive (we are not considering exotic matter); there is no possibility of arbitrarily "pinning" sources as is done in Newtonian gravitation, because of the automatic self-consistency of the nonlinear Einstein's equations. If we demand that the two black holes be fixed in space, then the solution includes a conical singularity (a “strut”) lying on the axis on which the two masses are located[1]. This singularity appears as a natural consequence of the field equations, and it is necessary to keep the two masses from falling towards each other. However, this singularity would have to be made of very exotic matter, and this solution does not describe any realistic system in astrophysics. The real solution to the relativistic two-body problem can have no conical singularities, and it is necessarily non-stationary. The two black holes will spiral around each other, emitting gravitational waves, which makes this problem even more difficult. There is no exact solution for the relativistic two-body problem, and even a numerical solution has eluded the most powerful computers.

In order to cope with this problem, Contopoulos and others [2, 3] have used the Majumdar-Papetrou solution [1] to study the dynamics of test particles in a space-time with two black holes. The Majumdar-Papetrou metric used by Contopoulos describes two non-rotating black holes with extreme electric charge ($Q = M$ in relativistic units), whose gravitational pull is exactly matched by their electrostatic repulsion, thereby allowing a static mass configuration. They have found that in this metric the motion of both light and massive particles is chaotic, with a fractal invariant set and a fractal basin boundary. However, it is very unlikely that the Majumdar-Papetrou metric describes realistic astronomical objects, since there is no known realistic astrophysical process by which a black hole with extreme charge could be formed. Even though the system of two black holes with extreme charge has proven useful a useful model, it is important to address the more realistic problem of two uncharged black holes. This is what we do in this article, for the motion of light and other massless particles.

In order to overcome the fact that there is no static solution for the two-black-hole system, we consider the case when the two black holes are far apart, with a distance much larger than their Schwarzschild radii. In this case, nonlinear effects in the field equations are expected to be small, and we can approximate the motion of test particles in the neighborhood of one of the masses as being the result of the field of that mass alone, and disregard the effect of the other black hole as being negligible. Using this approximation, the motion of test particles in the two-black-hole system is treated as a combination of motions caused by isolated Schwarzschild black holes. Since the equations of motion for the Schwarzschild geometry can be analytically integrated, our dynamical system is reduced to a map, which is much easier to study than a system of ordinary differential equations. This scattering map is built in Section 2, for the simple case of two black holes with equal masses. In Section 3, we show that this map has a fractal basin boundary separating the possible outcomes of a light ray in the two-black-hole field, namely, falling into either of the black holes or escaping towards the asymptotically plane infinity. The fractal (box-counting) dimension of this basin boundary is numerically calculated, and the sensitivity to initial conditions implied by the fractal nature of the boundary is thereby quantified. In Section 4 we use explicitly the condition of large separation between the black holes. In this limit, the basin boundary becomes a self-similar Cantor set, which allows us to obtain some analytical results. One of our main results is that the fractal dimension decays very slowly (logarithmically) with distance. The slow decay of the fractal dimension makes it more likely that the fractal nature of the basin boundary has some importance for astrophysics. In section 5, we consider the case of two black holes with unequal masses, in the limit of a large separation; we find that the logarithmic decay law of the fractal dimension for large distances is also valid in this case. In section 6, we summarize our results and draw some conclusions.

D.2 Scattering map for two black holes with equal masses

We begin by reviewing some basic results concerning the motion of test particles in the field of an isolated Schwarzschild black hole[4, 5]. We consider specifically the case of null geodesics.

The Schwarzschild metric is written in spherical coordinates as:

$$ds^2 = \left(1 - \frac{2M}{r}\right) dt^2 - \frac{dr^2}{1 - \frac{2M}{r}} - r^2 d\Omega^2,$$

with $d\Omega^2 = d\theta^2 + \sin^2\theta d\phi^2$ being the element of unit area, and t is the time measured by a distant observer. M is the black hole's mass in geometrized units. We are interested only in the region of space-time outside the event horizon, $r > 2M$. Due to the conservation of angular momentum, test particles move on a plane, which is conveniently chosen as $\theta = \pi/2$. The plane whereon the motion occurs is then described by the coordinates r and ϕ. The geodesic equations which describe trajectories of test particles on this plane can be analytically integrated by means of elliptical functions[4]. Here we are interested in the scattering of null geodesics by the black hole. A light ray coming from infinity towards the black hole is characterized by the impact parameter b defined by the ratio $b = L/E$, where the angular momentum L and the energy E are constants of motion given by:

$$E = \left(1 - \frac{2M}{r}\right)\frac{dt}{d\lambda};$$

$$L = r^2\frac{d\phi}{d\lambda};$$

λ is the geodesic's affine parameter. For null geodesics only the ratio of L and E is of importance to the dynamics. In the asymptotically plane region $r \to \infty$, b corresponds to the usual impact parameter of classical scattering problems.

If the impact parameter is below the critical value $b_c = 3\sqrt{3}M$, the light ray spirals down the event horizon and plunges into the black hole. If $b > b_c$, the ray circles the black hole and escapes again towards infinity, being deflected by an angle Δ. The lowest value P of the radial coordinate r along the trajectory (the "perihelium") is given by:

$$b^2 = \frac{P^3}{P - 2M}. \tag{D.1}$$

Following Chandrasekhar[4], we define the quantities Q, k and χ by:

$$Q^2 = (P - 2M)(P + 6M); \tag{D.2}$$

$$k^2 = \frac{Q - P + 6M}{2Q}; \tag{D.3}$$

$$\sin^2(\chi/2) = \frac{Q - P + 2M}{Q - P + 6M}. \tag{D.4}$$

The scattering angle Δ is then given by

$$\Delta = \pi - 2f(b), \tag{D.5}$$

and the function $f(b)$ is:

$$f(b) = 2\sqrt{\frac{P}{Q}}\left[K(k) - F(\chi/2, k)\right]. \tag{D.6}$$

Here F is the Jacobian elliptic integral and K is the complete elliptic integral. In Fig. 1 we show a plot of $\Delta(b)$. We observe that $\Delta(-b) = -\Delta(b)$. As b approaches the critical value b_c from above, Δ goes to infinity; trajectories with b sufficiently near b_c can circle the black hole an arbitrary number of times before escaping, and for $b = b_c$, the light ray makes an infinite number of rotations, and never escapes. This is a consequence of the existence of an unstable periodic orbit at $r = 3M$, which appears as a maximum in the effective potential. The orbits with $b = b_c$ spiral towards the $r = 3M$ orbit, and in the language of dynamical systems they make up the stable manifold associated with this periodic orbit.

The fact that Δ assumes values above π for a non-zero range of b implies the existence of a rainbow singularity in the scattering cross section; this is to be contrasted with the Newtonian Rutherford scattering, which shows no such singularities. In fact, Δ assumes arbitrarily large values, and the differential cross section at any given angle θ is made up by an infinite number of contributions arising from trajectories with $\Delta = \theta$, $\Delta = \theta + 2\pi$, in general $\Delta = \theta + 2n\pi$, corresponding to trajectories that circle the black hole n times before being scattered towards θ. However, large values of n correspond to very small ranges of b: the set of trajectories that scatters by $\theta + 2n\pi$ has a measure that decreases very rapidly with n. Chandrasekhar [4] shows that the impact parameter b_n corresponding to a scattering by $\theta + 2n\pi$ for large values of n is given approximately by:

$$b_n \equiv b_c + 3.48Me^{-(\theta+2n\pi)}. \tag{D.7}$$

This expression shows that the measure of the set of trajectories scattered by $\theta + 2n\pi$ decays exponentially with n, and the contribution of orbits with large n to the cross section is small. In fact, we shall see later that in many cases it is a good approximation to consider only orbits with $n = 0$.

After reviewing some properties of an isolated black hole, we now consider the case of two black holes with equal mass M (we consider the case of different masses in Section 5). As we mentioned in the introduction, there is no exact solution of Einstein's field equations that describes this system. Because of this, we assume that the two black holes are separated by a distance D much larger than their Schwarzschild radius $2M$; in this limit the nonlinear interaction between the two gravitational fields can be ignored. In a real system, the two black holes will be rotating around their center of mass; however, their rotation speed is much smaller than the velocity of light. For the purpose of studying the dynamics of null geodesics, we can thus consider the two black holes to be fixed in space, without incurring in too much error. Notice that this approximation is generally not be valid for massive test particles.

We are interested in the orbits that never escape to infinity nor fall into one of the event horizons; these orbits make up the basin boundary of the system, which will be discussed later in more detail. For the orbits not to escape, they need to have impact parameters such that they are scattered by at least π by one of the black holes. In the case of an isolated black hole, this corresponds to an impact parameter lower than $b = b_{esc} \approx 5.35696M$, which is less that three times the Schwarzschild radius. Since in our approximation $D \gg 2M$, for the purpose of finding the basin boundary we can consider that the light rays are scattered by each black hole separately, the other black hole being too far away to make a significant difference in the scattering. After suffering a scattering by one of the black holes, the ray may reach the other black hole, depending on its emerging trajectory after the first scattering. It is then scattered again, and may return to the first black hole, and so on. Since $D \gg 2M$, we consider the scattering process of each black hole separately and use formulas (D.5) and (D.6) to determine the deflection angle due to each black hole as a function of the incident impact parameter.

By making the approximations mentioned above, we reduce the motion of light in the two-black-hole space-time to a 2-d map. To do this, we make the further assumption that the light rays have zero angular momentum in the direction of the axial symmetry axis, on which lie the two black holes; the orbits are then confined to a plane containing the two black holes. Due to the axial symmetry of the system, the motions on all such planes are similar. Now suppose we have a light ray escaping from one of the black holes with impact parameter b_n and with an escaping angle ϕ_n with respect to the symmetry axis, as shown schematically in Figure 2. Since the black holes are considered to be very far apart, the impact parameter b_{n+1} of the light ray with respect to the other black hole is the segment l shown in Figure 2 (one black hole can be considered to be "at infinity" as regards the other). We use the convention that positive values of b means that the ray is directed to the right side of the black hole, and rays with negative b are directed to the left. From elementary geometry, we have $l = b_n + D \sin \phi_n$. The deflection angle is given by $\Delta(b_{n+1})$. The map is then written as:

$$b_{n+1} = b_n + D \sin \phi_n; \tag{D.8}$$

$$\phi_{n+1} = \pi + \phi_n - \Delta(b_{n+1}) \qquad \mathrm{mod}\ 2\pi. \tag{D.9}$$

The angles ϕ_n are measured counterclockwisely with respect to each black hole; the first term in Eq. (D.9) comes from the change in the angle's orientation necessary to take account of that.

Consider the initial conditions $b_0 = b_{esc}$ and $\phi_0 = 0$. Since $\Delta(b_{esc}) = \pi$, we see from the above equations that these values of b and ϕ are a fixed point of the map. It corresponds to the periodic orbit depicted in Figure 3a, which revolves around the black holes, making a U-turn at each black hole and then heading towards the other. Another periodic orbit is shown in Fig. 3b. This orbit is such that $b_{n+1} = -b_n$ and $\phi_{n+1} = -\phi_n$. Inserting these conditions in Eqs. (D.8) and (D.9), we find $2b_0 = -D \sin \phi_0$ and $\Delta(b_0) = \pi + 2|\phi_0|$ (remember that the angles are defined modulus 2π), with $b_0 > 0$. ϕ_0 is given by the solution of the equation

$$\Delta\left(\frac{D}{2} \sin|\phi_0|\right) = \pi + 2|\phi_0|.$$

These are the simplest periodic orbits, but there are many others. Indeed, we shall see later that there is a countably infinite set of periodic orbits circling the two black holes.

We observe that Equations (D.8) and (D.9) are valid only as long as b remains within the range $b_c < b < b_{esc}$. If b falls out of this interval, the ray either escapes or falls into one of the black holes, and the iteration must be stopped.

D.3 Analysis of the scattering map

We now proceed to study in detail the map defined by Equations (D.8) and (D.9). We begin by a direct numerical investigation of these equations.

In order to iterate Equations (D.8) and (D.9) for given initial values ϕ_0 and b_0, we first have to be able to calculate the deflection angle Δ for a given impact parameter b. To do this, we must begin by finding the "perihelium distance" P corresponding to b; this is done by solving the third-order equation (D.1) for P. We use the well-known Newton-Raphson method, which guarantees a very fast convergence[6]. We then use Eqs. (D.2), (D.3) and (D.4) to calculate Q, k and χ, and we finally substitute these quantities in Eqs. (D.5) and (D.6) to obtain $\Delta(b)$. The elliptical functions F and K are computed by numerical routines found in [6].

Depending on its initial conditions, a light ray may either fall into one black hole, fall into the other black hole, or escape towards infinity. The set of initial conditions which leads to each of these outcomes is called the *basin* of that outcome. In our numerical iteration of the map (D.8,D.9), we are interested in obtaining a basin portrait of the system. To do this, we have to choose a set of initial conditions and iterate them to find out to which basin they belong. Our choice is the one-dimensional set with $\phi_0 = 0$ and an interval of b. As we have seen in the previous Section, if $|b| < b_c$, the light ray always falls into the event horizon, and if $|b| > b_{esc}$, it always escapes. We thus choose the interval to be $b_c < b < b_{esc}$. We divide this segment into 5000 points, and iterate the map (D.8,D.9) for each of these initial conditions, recording the final outcome for each point: if at any point in the iteration $|b_n| < b_c$, this means that the light ray falls into one of the black holes, and if $|b_n| > b_{esc}$, it escapes to infinity. We define the discrete-valued function $g(b)$ to be 1 if the orbit with initial conditions $\phi_0 = 0$, $b_0 = b$ falls into one of the black holes, -1 if it falls into the other, and 0 if it escapes to the asymptotically plane region. $g(b)$ gives a picture of the intersections of the three basins with the segment $\phi_0 = 0$, $b_c < b < b_{esc}$.

The result is shown in Fig. 4a, for $D = 15M$. We see that there are large intervals in which g is constant, intercalated by ranges of b where g varies wildly. If b_0 lies within one of these latter ranges, the final outcome of the light ray is highly uncertain. In Fig. 4b we show a magnification of one of these regions. Except for the scale, it is very similar to Fig. 4a. A further magnification is shown in Fig. 4c, again revealing structure in small scales. We have obtained even further magnifications, which are not shown here, and all show similar structures, down to the smallest scales allowed by the numerical limitations. This shows that g has a fractal dependency on b. Notice that there are large intervals of b where g is perfectly regular. These regular regions are mixed in all scales with the fractal regions, where the outcome of a light ray is highly uncertain. This sensitivity of the dynamics to the initial conditions is made precise with the definition of the *box-counting dimension*, which we now present briefly[7].

We define the *basin boundary* of the system to be the set of points (initial conditions) such that all neighborhoods of these points have points belonging to at least two different basins, no matter how small that neighborhood is. The fractal nature of the basins shown in Fig. 4 results from a fractal basin boundary[7]. It is not difficult to see that a fractal basin boundary implies a fundamental uncertainty in the final outcome of an orbit. We now define the box-counting dimension of the basin boundary, which gives a measure of this uncertainty. Let b_0 be a randomly chosen impact parameter in the interval $[b_c, b_{esc}]$; we consider $\phi_0 = 0$ throughout for simplification. Let $f(\epsilon)$ be the probability that there is a point of the basin boundary lying within a distance ϵ from b_0. In the limit $\epsilon \to 0$, f generally scales with ϵ by a power law. We thus write:

$$f(\epsilon) \propto \epsilon^{1-d}. \tag{D.10}$$

d is the box-counting dimension of the intersection of the basin boundary with the one-dimensional section of initial conditions given by $b \in [b_c, b_{esc}]$ and $\phi_0 = 0$. Clearly, we must have $0 \leq d \leq 1$. If the basin boundary is regular, then $d = 0$; fractal boundaries have $d > 0$. f can be interpreted as a measure of the uncertainty as to which basin the point b belongs, for a given error ϵ in the initial condition, which is always present in a real situation. For a regular basin boundary, f decreases linearly with ϵ. If we have a fractal boundary, however, the exponent in the power law (D.10) is less than 1, and f decreases much more slowly with ϵ, which makes the uncertainty in the outcome much higher than in the case of a regular boundary. Thus, d is a good measure of the sensitivity to the initial conditions that results from a fractal basin boundary, and since it is a topological invariant[7], it is a meaningful characterization of chaos in general relativity.

We calculate the box-counting dimension d numerically by using the method we now explain[7]. We pick a large number of initial conditions b randomly, and for each one of them we compute the map (D.8-D.9), finding out its outcome and therefore to which basin it belongs. We then do the same thing to the two neighboring initial conditions $b + \epsilon$ and $b - \epsilon$, for a given (small) ϵ, for each b. If the three points do not belong to the same basin, b is labeled an "uncertain" initial condition. For a large number of initial conditions, we expect that the fraction of uncertain points for a given ϵ approximates $f(\epsilon)$. Calculating in this way f for several values of ϵ, we use Eq. (D.10) to obtain d from the inclination of the log-log plot of f versus ϵ. Applied to the two-black-hole map with $D = 15M$, this method gives $d = 0.17 \pm 0.02$. The error comes from the statistical uncertainty which results from the finite number of points used in the computation of f. In our calculation, the number of initial conditions was such that the number of "uncertain points" is always higher than 200.

How does the fractal basin boundary arise from the dynamics of the map (D.8-D.9)? In order to answer this question, we first observe that every point in the basin boundary gives rise to orbits that neither escape nor fall into one of the black holes (otherwise they would be part of one of the basins, which violates the definition of the basin boundary); that is, the basin boundary is made up of "eternal orbits" which move forever around the two black holes. We need thus to investigate these orbits to understand the formation of the basin boundary.

Consider the one-dimensional set of initial conditions parameterized by the impact parameter b with $\phi_0 = 0$. We have seen that if $|b| < b_c$ the orbit falls into the event horizon of a black hole, and if $|b| > b_{esc}$ the orbit escapes. Thus, the points of the basin boundary belong to the interval

$$|b| \in [b_c, b_{esc}], \tag{D.11}$$

which is actually two disjoint intervals, corresponding to positive and negative values of b. However, not all points in this interval are part of the basin boundary; in order to survive the next iteration of the map (D.8-D.9) without escaping or falling, the corresponding orbits must be deflected in such a way that they reach the other black hole with an impact parameter within the interval (D.11). From Fig. 5 we see that for this to happen the orbits must be deflected by an angle θ in the neighborhood of $(2n+1)\pi + \alpha$, and either $(2n+1)\pi$ or $(2n+1)\pi + 2\alpha$, depending on the previous deflection suffered by the orbit; the angle α depends on the distance separating the black holes. n is the number of turns the orbit makes around one of the black holes before moving on to the other one. For each n, there are two intervals of the deflection angle θ for which the orbit survives the next iteration without escaping or falling; these two intervals correspond to the positive and negative values of b satisfying Eq. (D.11). In the first iteration, the initial interval (D.11) is divided into infinitely many pairs of sub-intervals, each pair labeled by the number n of times the orbit circles the black hole. From Eq. (D.7), intervals corresponding to large n's decrease exponentially with n. In the next iteration, each of these sub-intervals are themselves divided into an infinite number of intervals, and so on in the next iterations. In the limit of infinite iterations, the set of surviving orbits is a fractal set with zero measure. This set is the basin boundary, and its fractality is responsible for the complex dynamics shown in Fig. 4. The two fractal regions on the right of Fig. 4a consist of orbits whose first scattering has $n = 0$, that is, they are deflected by the black hole by π and $\pi + \alpha$. The leftmost fractal region in Fig. 4a is actually an infinite number of very small regions, corresponding to orbits with $n \neq 0$; the scale of Fig. 4a is too gross for them to be distinguished.

This gives us an indication that the orbits with $n > 0$ make up only a very small fraction of the basin boundary; we shall return to this later in this Section.

Each orbit which is part of the basin boundary can be labeled by an infinite sequence of symbols $a_1 a_2 a_3 \cdots$ (including bi-infinite sequences $\cdots a_{-2} a_{-1} a_0 a_1 a_2 \cdots$), where each symbol $a_m = n_m(k_m)$ gives the neighborhood of the deflection angle $(2n_m + 1)\pi + k_m \alpha$ after the m-th scattering. As an example, the periodic orbit shown in Fig. 3a is represented by the sequence $0(0)0(0)0(0)\cdots$. Periodic orbits correspond to repeating sequences, and they define a countably infinite set. However, not all sequences are allowed. It is clear from Fig. 5 that a symbol $n(0)$ must be followed either by one of type $m(0)$ or $m(1)$, but it cannot be followed by a symbol like $m(2)$, that is, of the form $m(k)$ with $k = 2$. Analogously, a symbol with $k = 1$ of $k = 2$ cannot be followed by one with $k = 0$. Even with these restrictions, however, there is an uncountable set of non-repeating sequences which label orbits that are part of the basin boundary. The uncountability of this set is a reflection of the fractal nature of the boundary.

The basin boundary is the stable manifold of the invariant set, which is made by orbits labeled by bi-infinite symbols $\cdots a_{-2} a_{-1} a_0 a_1 a_2 \cdots$. These are orbits that do not escape for both forward and backward iterations of the map (D.8-D.9).

It is important to observe that the basin boundary is fractal because the scattering function $\Delta(b)$ of the isolated black hole (D.5) assumes values higher than π, which makes it possible for orbits to be scattered to both sides of the black hole, giving rise to the fractal basin boundary. The scattering of particles by two fixed Newtonian mass points is immediately seen to be regular, because Rutherford's scattering function does not assume values higher than π. This is of course in accordance with the fact that the fixed two-mass problem in Newtonian gravitation is integrable, since the Hamilton-Jacobi equation of this system is separated in elliptical coordinates [8].

We have seen that after being scattered by a black hole, the light ray must have an impact parameter lying on the interval (D.11) to belong to the basin boundary. Since $b_c = 3\sqrt{3}M \approx 5.19615M$ and $b_{esc} \approx 5.35696M$, the impact parameter must belong to one of two intervals of length $\Delta b = b_{esc} - b_c \approx 0.16081M$ (the two intervals correspond to positive and negative impact parameters). In our approximation, we have $\Delta b \ll D$. Using this fact, we can approximate the value of b in Fig. 5a by b_{esc}, with an error of Δb at worst, which means a fractional error of about $\Delta b / b_{esc} \approx 0.03$. The distance L in Fig. 5a traveled by orbits which were deflected by $(2n+1)\pi+\alpha$ or $(2n+1)\pi+2\alpha$ in the previous scattering is thus given by $(L/2)^2+b_{esc}^2=(D/2)^2$, that is,

$$L=\sqrt{D^2-4b_{esc}^2}. \tag{D.12}$$

For the map (D.8-D.9) to be well-defined, we must have $D>2b_{esc}$. Of course, this condition is satisfied in our approximation $D\gg 2M$. The angle α is calculated from Fig. 5 in this approximation, using elementary geometry:

$$\sin\alpha=\frac{2b_{esc}}{D}. \tag{D.13}$$

Consider a set of orbits with impact parameters filling the interval $[b_c,b_{esc}]$ of length Δb, which may have already suffered several previous scatterings. The subsets of these orbits that survive the next scattering without escaping nor falling in one of the black holes are sub-intervals in the neighborhood of b_n^k, where b_n^k are the values of the impact parameter such that the orbit is deflected by an angle of $(2n+1)\pi+k\alpha$ ($k=0$, 1 or 2). They are solutions of the algebraic equation

$$\Delta(b_n^k)=(2n+1)\pi+k\alpha, \tag{D.14}$$

with Δ given by Eq. (D.5). The fractal regions of Fig. 4a are located around values of b given by Eq. (D.14) with $k=0$ and $k=1$. Depending on the previous deflections suffered by a given set of trajectories, the values $k=1$ and $k=2$ must be used instead in Eq. (D.14), according to the rules of the symbolic dynamics we exposed above.

Because the distance D is much larger than Δb, the allowed range in the deflection angle $\delta\theta_n^k$ around $(2n+1)\pi+k\alpha$ of an orbit such that it arrives at the other black hole with b in one of the intervals (D.11) is approximately:

$$\delta\theta_n^0=\frac{\Delta b}{D};\quad \delta\theta_n^{1,2}=\frac{\Delta b}{L}, \tag{D.15}$$

where L is given by Eq. (D.12). The length Δb_n^k of the interval of surviving orbits around b_n^k is in this approximation much smaller than Δb: $\Delta b_n^k\ll\Delta b$. We can therefore approximate Δb_n^k by the first-order expression $\Delta b_n^k\approx\delta\theta_n^k/|\Delta'(b_n^k)|$, with $\Delta'=d\Delta/db$. We define $\lambda_n^k=\Delta b_n^k/\Delta b$ as the fraction of the interval $[b_c,b_{esc}]$ (or $[-b_{esc},-b_c]$) occupied by the surviving orbits with b around b_n^k. We have:

$$\lambda_n^0=\frac{1}{D|\Delta'(b_n^0)|};\quad \lambda_n^{1,2}=\frac{1}{L|\Delta'(b_n^{1,2})|}. \tag{D.16}$$

Given a value of D, it is easy to solve Eq. (D.14) numerically for b_n^k, with L and α given by Eqs. (D.12) and (D.13). For $D = 15M$, we find $L \approx 10.5M$ and $\alpha \approx 0.7956$. By a direct numerical calculation of Δ and its first derivatives, we find:

$$\begin{aligned} b_0^0 &= b_{esc}; \quad \Delta'(b_0^0) = -5.863/M; \quad \Delta''(b_0^0) = 38.30/M^2; \\ b_0^1 &= 5.26629M; \quad \Delta'(b_0^1) = -13.35/M; \quad \Delta''(b_0^1) = 202.5/M^2; \\ b_0^2 &= 5.22729M; \quad \Delta'(b_0^2) = -31.66/M; \quad \Delta''(b_0^2) = 1030/M^2; \\ b_1^0 &= 5.19643M; \quad \Delta'(b_1^0) \approx -3600/M; \quad \Delta''(b_1^0) \approx 1.3 \times 10^7/M^2. \end{aligned} \tag{D.17}$$

Here $\Delta'' = d^2\Delta/db^2$. The second derivative of Δ will be used below. Notice that b_n^0 is independent of D. Using Eq. (D.16), we obtain:

$$\lambda_0^0 = 0.01137; \quad \lambda_0^1 = 0.007134; \quad \lambda_0^2 = 0.003008;$$

$$\lambda_1^0 \approx 1.85 \times 10^{-5}.$$

We see that λ_1^0 is two or three orders of magnitude smaller that λ_0^k, and the other λ_n^k's with $n \geq 1$ are even smaller. From Eq. (D.7), they decrease exponentially with increasing n. These values show that for most purposes we can disregard the contributions to the dynamics from deflections with $n > 0$: the measure of the set of orbits that make multiple turns around a black hole is negligible. This approximation will be used extensively in the next Section.

Equations (D.14-D.16) are not exact, because the derivative $\Delta'(b)$ varies in the intervals Δb_n^k. To estimate the error, we use the fact that the Δb_n^k are small. The error $\delta\lambda_n^k$ in λ_n^k is then to first order:

$$\delta\lambda_n^0 = \frac{\Delta b_n^0}{D}\frac{\Delta''(b_n^0)}{[\Delta'(b_n^0)]^2}; \quad \delta\lambda_n^{1,2} = \frac{\Delta b_n^{1,2}}{L}\frac{\Delta''(b_n^{1,2})}{\left[\Delta'(b_n^{1,2})\right]^2}.$$

Using $\Delta b_n^k = \Delta b \lambda_n^k$, we get the fractional error $\delta\lambda_n^k/\lambda_n^k$:

$$\frac{\delta\lambda_n^0}{\lambda_n^0} = \frac{\Delta b}{D}\frac{\Delta''(b_n^0)}{[\Delta'(b_n^0)]^2}; \quad \frac{\delta\lambda_n^{1,2}}{\lambda_n^{1,2}} = \frac{\Delta b}{L}\frac{\Delta''(b_n^{1,2})}{\left[\Delta'(b_n^{1,2})\right]^2}. \tag{D.18}$$

The terms $\Delta''(b_n^k)/\left(\Delta'(b_n^k)\right)^2$ are of the order of 1, and the terms $\Delta b/D$ and $\Delta b/L$ are much smaller than 1. Thus, the fractional errors in the values λ_n^k given by the approximate formula (D.16) are very small, of about 0.01 for $D = 15M$. In the limit of large D, we have $L \approx D$, and $\delta\lambda_n^k/\lambda_n^k \sim 1/D$: the fractional error is inversely proportional to the separation D, and the approximation (D.16) gets better and better as D increases.

D.4 The limit $D \to \infty$

We now take the limit $D \gg 2b_{esc}$. From Eqs. (D.13) and (D.12), we have that in this limit $\alpha \to 0$ and $L \to D$. Eqs. (D.14) and (D.16) then imply that $b_n^k \to b_n^0 \equiv b_n$ and $\Delta b_n^k \to \Delta b_n^0 \equiv \Delta b_n$: the two intervals of surviving orbits of a given n come closer and closer as D increases, and their lengths become the same in this limit. Because of the approximate equality in the lengths, the magnification of each interval by $(\lambda_n)^{-1}$ gives approximately the same set of intervals. In other words, the fractal basin boundary is *self-similar* in this approximation.

The box-counting dimension of this self-similar set is given by the solution of the transcendental equation[7]:

$$2\sum_{n=0}^{\infty}(\lambda_n)^d = 1.$$

As we have seen in the previous Section, λ_1 is many orders of magnitude smaller than λ_0. Therefore, it is a good approximation to neglect terms with $n > 0$ in the above expression, and d can then be explicitly written as:

$$d = \frac{\ln 2}{\ln(\lambda_0)^{-1}}. \tag{D.19}$$

From Eq. (D.16), we have $(\lambda_0)^{-1} = D|\Delta'(b_{esc})|$, and we get:

$$d = \frac{\ln 2}{\ln D + \beta}, \tag{D.20}$$

with $\beta = \ln|\Delta'(b_{esc})|$. For large D, the box-counting dimension decays logarithmically with the distance, which is a very slow decay law. Even for the large distances found in astronomy, d is still non-negligible. Since the box-counting dimension is linked to the scattering cross-section [9], the slow decay of d with D shown in Eq. (D.20) could have observational consequences.

D.5 The case of different masses

Now we consider the case of two black holes with different masses M_a and M_b. We restrict ourselves to the limit $D \gg 2b^a_{esc}, 2b^b_{esc}$, where b^a_{esc} and b^b_{esc} are the impact parameters corresponding to deflections of π of the two black holes. Because the two masses are different, the ranges Δb_a and Δb_b of impact parameters for surviving orbits are different, and therefore the allowed range of scattering angles depends on which black hole the orbit is heading to. This means that the 'shrinking factors' λ^a_0 and λ^b_0 (given by Eq. (D.16)) depend on the black hole. This spoils the property of self-similarity, which is a feature of the equal-masses case in the limit $D \to \infty$. However, since the orbits are scattered alternately by the two black holes, the *square* of the scattering map defined by the system is self-similar, in the limit $D \to \infty$.

After two iterations, of each interval $[b_c, b_{esc}]$ there remains four subsets of surviving orbits, all with size of approximately $\lambda^a_0\lambda^b_0$ (we are not considering orbits with $n > 0$). Each of these subsets gives rise to four others after two further iterations, and so on. The box-counting dimension of the surviving set is given by[7] $4(\lambda^a_0\lambda^b_0)^d = 1$, that is:

$$d = -\frac{\ln 4}{\ln\left(\lambda^a_0\lambda^b_0\right)}.$$

Substituting Eqs. (D.16) and (D.17) with M replaced by M_a and M_b, we obtain λ^a_0 and λ^b_0, and we find:

$$d = \frac{\ln 2}{\ln D + \beta + \ln\sqrt{\eta}}, \tag{D.21}$$

where $\eta = M_a/M_b$, $\beta = \ln \Delta'(b^a_{esc})$. The difference between Eqs. (D.21) and (D.20) is the constant term $\ln\sqrt{\eta}$ in the denominator of d. If $M_a = M_b$, then $\eta = 1$ and Eq. (D.21) is equal to Eq. (D.20), as of course it should. In the limit $D \to \infty$, d also decays logarithmically with distance in this case, as in the case of equal masses.

D.6 Conclusions

In this article we have studied the chaotic behavior of light rays orbiting a system of two non-rotating fixed black holes. We have assumed that the black holes are sufficiently far away from each other, so that we could consider the motion of the light rays to be the result of the action of each black hole separately. Since the equations of motion of a light ray in the space-time of an isolated black hole can be solved analytically, using this approximation we reduce the motion of the massless test particle to a 2-dimensional map. Numerical integration of this map showed the existence of a fractal basin boundary, with an associated fractional box-counting dimension. In the limit of a large separation distance D between the two black holes, we have been able to obtain an analytical expression to the asymptotic value of the box-counting dimension d. We found that $d \sim (\ln D)^{-1}$ for large D; this result also holds for different black hole masses.

Bibliography

[1] D. Kramer, H. Stephani, M. MacCallum and E. Herlt, *Exact solutions of Einstein's field equations*, Cambridge University Press, Cambridge (1980).

[2] G. Contopoulos, Proc. R. Soc. Lond. A **431**, 183 (1990).

[3] C. P. Dettmann, N. E. Frankel and N. J. Cornish, Phys. Rev. D **50**, R619 (1994).

[4] S. Chandrasekhar, *The mathematical theory of black holes*, Oxford University Press, Oxford (1992)

[5] I. D. Novikov and V. P. Frolov, *Physics of black holes*, Kluwer Academic Publishers, Dordrecht (1988).

[6] *Numerical recipes in C*,

[7] E. Ott, *Chaos in dynamical systems*, Cambridge University Press, Cambridge (1993)

[8] E. T. Whittaker, *A treatise on the analytical dynamics of particles and rigid bodies*, Cambridge University Press, Cambridge (1970)

[9] J. Levin, PREPRINT CfPA-98-TH-19

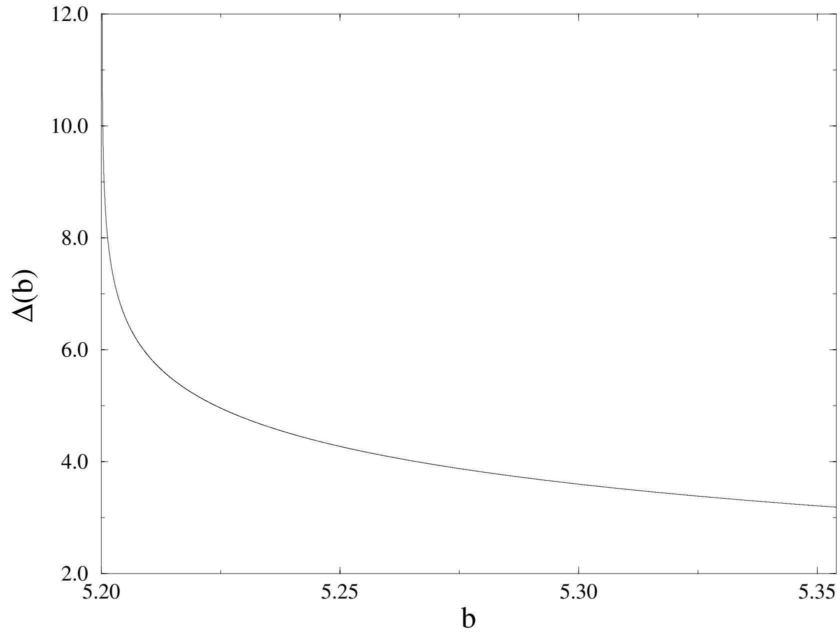

Figure D.1: The deflection function $\Delta(b)$ for an isolated Schwarzschild black hole.

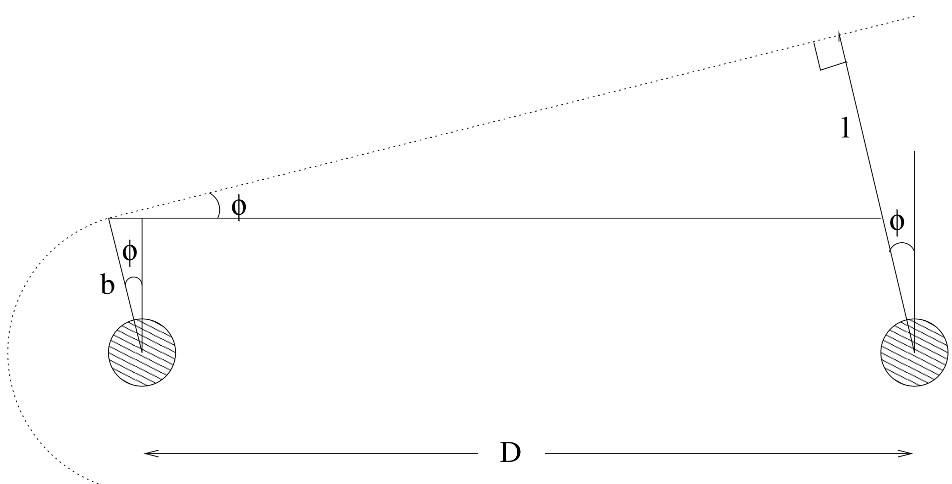

Figure D.2: Construction of the scattering map.

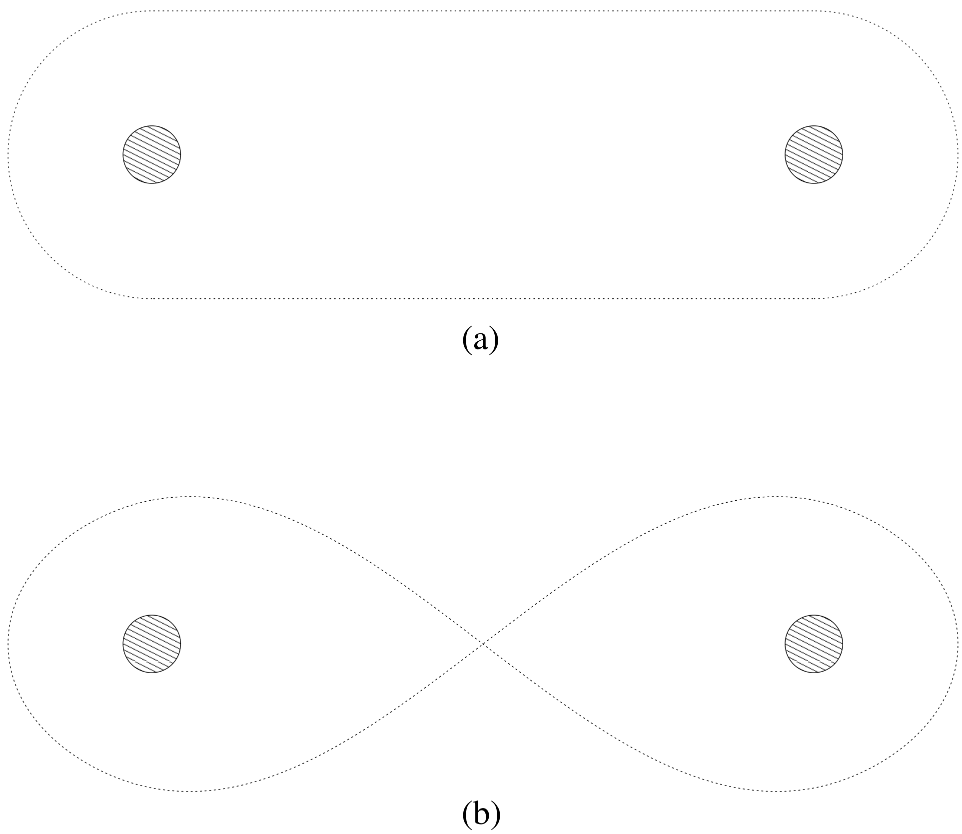

Figure D.3: Two examples of periodic orbits of the scattering map.

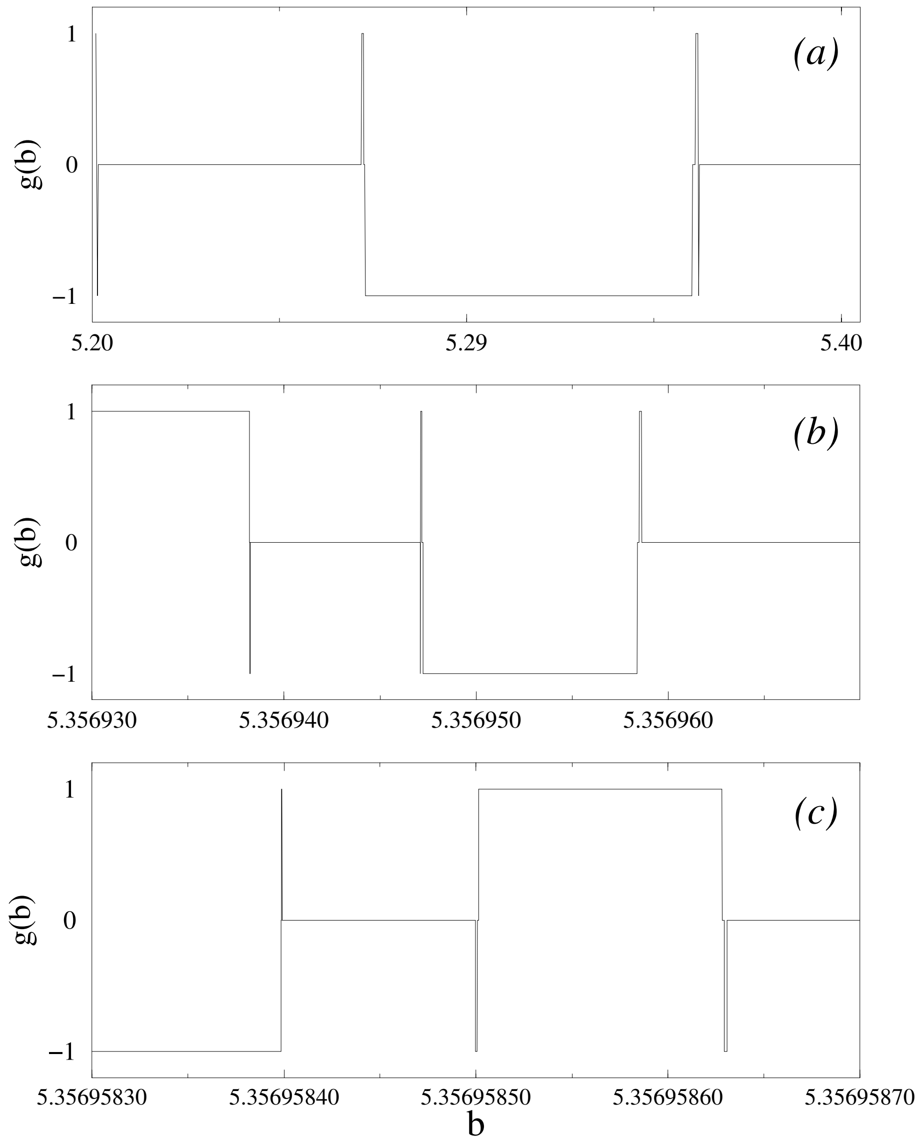

Figure D.4: Portrait of the basins as a function of the impact parameter b, for $\phi_0 = 0$. The 'basin function' $g(b)$ is defined to be 1 if the orbit with initial conditions $\phi_0 = 0$, $b_0 = b$ falls into one of the black holes, -1 if it falls into the other black hole, and 0 if it escapes to the asymptotically plane region. Two successive magnifications of a small region of the initial interval are pictured, showing the fractal dependency of g on b.

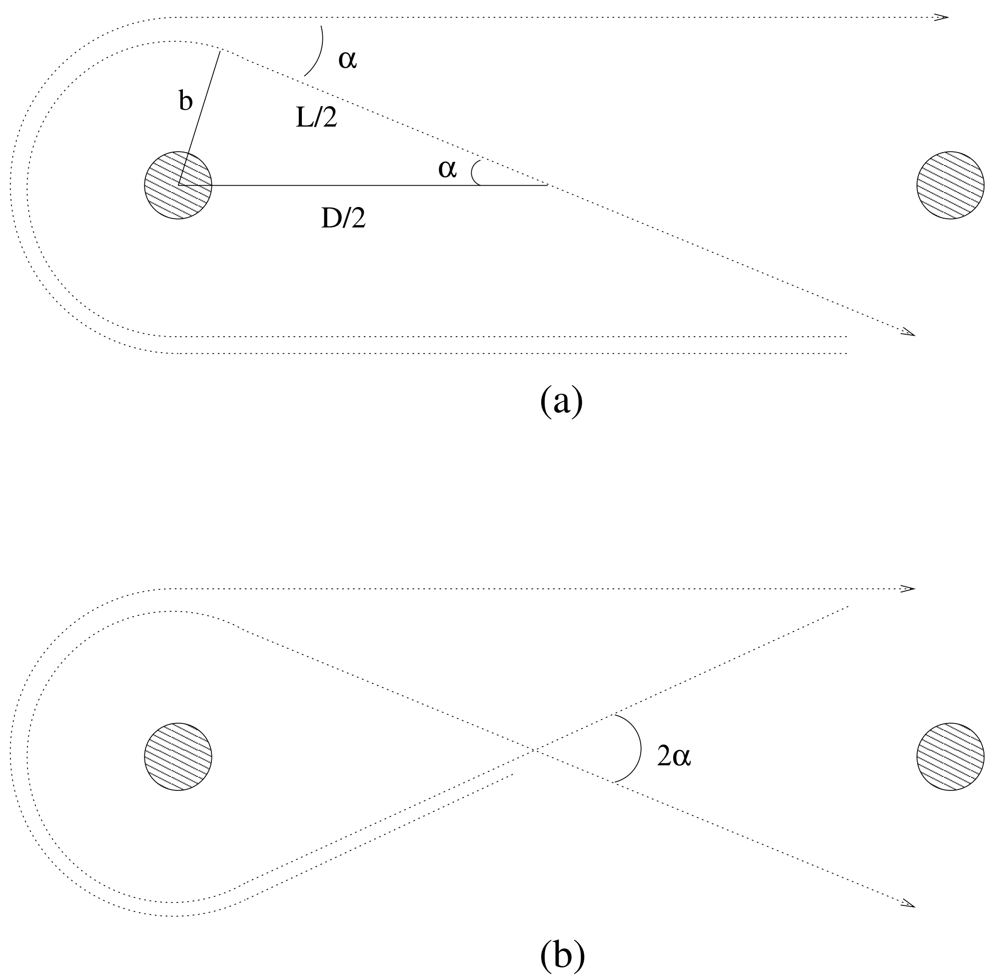

Figure D.5: (a) Two possible types of scatterings for an orbit which was previously scattered by $(2n+1)\pi$; (b) two scatterings for an orbit which was previously deflected by $(2n+1)\pi+\alpha$ or $(2n+1)\pi+2\alpha$.